



HAL
open science

Strongly driven quantum Josephson circuits

Lucas Verney

► **To cite this version:**

Lucas Verney. Strongly driven quantum Josephson circuits. Physics [physics]. Université Paris sciences et lettres, 2019. English. NNT : 2019PSLEE008 . tel-02307683

HAL Id: tel-02307683

<https://theses.hal.science/tel-02307683v1>

Submitted on 7 Oct 2019

HAL is a multi-disciplinary open access archive for the deposit and dissemination of scientific research documents, whether they are published or not. The documents may come from teaching and research institutions in France or abroad, or from public or private research centers.

L'archive ouverte pluridisciplinaire **HAL**, est destinée au dépôt et à la diffusion de documents scientifiques de niveau recherche, publiés ou non, émanant des établissements d'enseignement et de recherche français ou étrangers, des laboratoires publics ou privés.

THÈSE DE DOCTORAT
DE L'UNIVERSITÉ PSL
Préparée à l'École normale supérieure

Strongly driven quantum Josephson circuits

Soutenue par
Lucas Verney
Le 11 juillet 2019

École doctorale n°564
École Doctorale Physique
en Île-de-France

Spécialité
Physique

Composition du jury :

Serge Florens Directeur de recherche, CNRS	<i>Président et rapporteur</i>
Olivier Buisson Directeur de recherche, CNRS	<i>Rapporteur</i>
Mazyar Mirrahimi Directeur de recherche, INRIA Paris	<i>Directeur de thèse</i>
Zaki Leghtas Professeur associé, Mines ParisTech	<i>Co-directeur de thèse</i>

Résumé

Une machine quantique est un appareil dont les degrés de liberté et leur évolution sont gouvernés par les lois de la mécanique quantique. Il existe un certain nombre d'indices et de preuves que de telles machines pourraient offrir des possibilités radicalement différentes de celles offertes par les machines classiques. Elles pourraient résoudre des problèmes actuellement hors de portée des machines classiques, tel que fournir des moyens de faire des transferts sécurisés sur des réseaux [1], permettre de réaliser des mesures physiques avec une précision inégalée [2], générer de vrais nombres aléatoires certifiés [3] ou fournir une accélération importante pour résoudre des problèmes spécifiques [4].

Par le passé, les systèmes atomiques, optiques ou à base d'ions piégés ont été étudiés comme brique de base pour construire ces machines quantiques. Cependant, depuis la première démonstration il y a un peu plus de vingt ans [5, 6], les circuits quantiques à base de supraconducteurs sont de plus en plus prometteurs pour réaliser des bits quantiques. Ces circuits peuvent être utilisés pour créer des oscillateurs qui stockent des photons micro-ondes individuels et ainsi construire des bits quantiques. Tous les éléments de ces circuits sont intrinsèquement régis par les lois de la mécanique quantique : leurs niveaux d'énergie sont quantifiés et leur espacement est plus grand que l'énergie associée à la température (pour des températures cryogéniques accessibles en laboratoire). Afin de prédire leurs propriétés, le courant et la tension doivent tous deux être traités comme des opérateurs quantiques non commutatifs. Le temps de cohérence de ces circuits a progressé rapidement et continuellement, de plusieurs ordres de grandeur, et atteint désormais quelques millisecondes pour les meilleurs systèmes [7, 8, 9, 10, 11]. Contrairement aux systèmes utilisant la physique atomique, les circuits supraconducteurs fournissent une grande flexibilité dans les paramètres exploitables et dans la complexité des hamiltoniens les représentant. Cette flexibilité nous permet d'explorer des régimes d'opération entièrement nouveaux. De plus, les signaux micro-ondes, au contraire des signaux dans le domaine optique, sont très bien contrôlés et manipulés avec des équipements électroniques du commerce, développés pour l'ingénierie radio-fréquence. La nanofabrication nécessaire pour réaliser de tels circuits est de mieux en mieux contrôlée, de sorte qu'il devient désormais possible de fabriquer de multiples circuits complexes en parallèle. Ces récentes avancées laissent supposer qu'il sera bientôt possible de réaliser des processeurs quantiques contenant un nombre de qubits suffisant pour offrir des applications pratiques intéressantes, comme le montre également les récents investissements commerciaux dans ce domaine (de la part de Google, IBM, Intel ou Rigetti Computing).

Toutes ces propriétés ont fait des circuits supraconducteurs un cadre prometteur pour le traitement de l'information quantique. Des machines quantiques à petite échelle (seulement quelques degrés de liberté ou qubits) ont déjà été démontrées et ont récemment mené au développement de système à plusieurs qubits (entre cinquante et cent) et à leur comparaison avec les performances de matériel classique. En effet, de nombreuses

expériences précédemment réalisées en utilisant d'autres systèmes physiques (ions piégés, résonance magnétique nucléaire ou électrodynamique quantique avec des atomes de Rydberg) ont été reproduites avec succès avec des circuits supraconducteurs. Dans la plupart de ces expériences, les propriétés des circuits supraconducteurs, telles que leur facilité de contrôle et d'ajustement des forces des couplages ou des non-linéarités, ainsi que leur temps de cohérence raisonnable, leur a permis d'obtenir des performances comparables voire meilleures que leurs équivalents atomiques ou optiques.

Cependant, et malgré ces nombreux succès jusqu'à présent, le passage à l'échelle de ces systèmes à un nombre de degrés de liberté intéressant pour des applications pratiques, reste un problème ouvert. En effet, la prochaine étape critique pour le développement du traitement de l'information quantique est la correction active d'erreur, qui consiste à concevoir des encodages logiques de l'information, qui est alors protégée contre les principales sources de décohérence, à partir de multiples qubits physiques sous-jacents. De tels qubits logiques devraient atteindre un temps de cohérence bien meilleur que celui des qubits physiques sous-jacents. Cette approche est coûteuse en infrastructure physique, demandant jusqu'à plus de mille qubits physiques pour réaliser un seul qubit logique.

Dans cette thèse, je me concentre sur les circuits quantiques à base de supraconducteurs, non pas comme une source de qubits physiques, mais plutôt comme une façon d'émuler des hamiltoniens d'interactions particuliers (souvent non-linéaires) entre plusieurs sous-systèmes (par exemple entre deux cavités micro-ondes). Ceci est équivalent à considérer un atome (artificiel) couplé à des modes photoniques discrets dans une cavité à haut facteur de qualité, qui est le domaine de l'électrodynamique quantique en cavité (CQED) [12]. Dans la version optique, on utilise généralement des lasers et on surveille les changements dans la transmission à travers la cavité, résultant de la chute d'atomes à travers la cavité. Je considère ici une version à base de circuits, où le circuit supraconducteur joue le rôle d'atome artificiel. Cette implantation bénéficie de la grande flexibilité des circuits supraconducteurs, permettant ainsi de facilement modifier et ajuster l'interaction entre les sous-systèmes [13].

Le comportement de ces circuits supraconducteurs (Fig. 1.1) et leur quantification est assez bien comprise [14]. Cependant, le régime dans lequel les champs envoyés sur les circuits sont de forts champs micro-ondes n'est pas encore maîtrisé. En effet, ces systèmes sont des systèmes quantiques, ouverts par nature, avec des non-linéarités importantes et en présence de champs dépendant du temps. La combinaison de ces caractéristiques les rend uniques et difficiles à étudier avec les approches précédentes de la physique atomique ou de l'optique. Par exemple, de récentes expériences [15] montrent que quand un circuit supraconducteur est soumis à des champs micro-ondes forts, au-delà du régime de réponse linéaire, les taux de dissipation observés semblent substantiellement différents de ceux attendus en considérant uniquement l'environnement électromagnétique du qubit seul.

Cette thèse se concentre sur l'étude de la dynamique des circuits supraconducteurs en présence de dissipation et de champs micro-ondes forts, ainsi que ses conséquences sur l'utilisation de tels circuits comme brique de base pour émuler des interactions hamiltoniennes particulières, telles que celles requises pour réaliser l'encodage logique de l'information quantique sur des états de chats de Schrödinger [16]. En effet, par application de champs micro-ondes à des fréquences bien choisies sur un circuit supraconducteur, on peut obtenir de nouveaux termes d'interaction hamiltonienne, par interaction paramétrique. Contrairement à une situation d'une interaction directe entre deux cavités, une interaction paramétrique permet ainsi d'avoir une plus grande variété

dans la forme des termes d'interaction, tout en réduisant les contraintes d'ajustement de fréquences des oscillateurs du système physique utilisé. D'autre part, l'amplitude de l'interaction paramétrique résultante augmente avec l'amplitude des champs appliqués. Il semblerait donc à première vue qu'une telle approche devrait permettre d'obtenir des couplages aussi importants que nécessaires, relativement facilement. Il ne faut cependant pas oublier les effets observés lors de l'application de champs forts sur un circuit supraconducteur, qui limitent fortement la possibilité d'explorer ces régimes particuliers.

L'étude d'un circuit supraconducteur parmi les plus simples, le transmon, consistant en une jonction Josephson et un condensateur en parallèle, constitue la première partie de ce travail de thèse. Je montre ainsi, en développant une méthode numérique de simulations basée sur l'approche de Floquet-Markov et en comparant à des résultats expérimentaux, que le transmon est dynamiquement instable en présence de champs forts. Au-delà d'une certaine puissance incidente, son état ne repose plus dans le confinement fourni par le potentiel en cosinus de la jonction Josephson et il se comporte alors comme une sorte de particule libre, ne contribuant plus aucune non-linéarité au circuit et annulant dès lors son intérêt dans le cadre de pompage paramétrique. D'autre part, en sortant du confinement en cosinus, il devient rapidement très impur.

Dans une deuxième partie, je propose un circuit alternatif, comportant une inductance supplémentaire en parallèle du transmon. Cette inductance fournit un potentiel quadratique qui confine alors l'état du transmon pour toutes les puissances de pompe. J'étudie le comportement de ce système en utilisant la même approche numérique que précédemment et trouve alors qu'il a un comportement bien plus régulier. Son état reste pur sur une grande plage de puissances incidentes et son comportement général, bien plus régulier, est bien approché par des modèles analytiques simples obtenus par moyennisation. Dès lors, de tels systèmes avec des éléments inductifs semblent de très bons choix pour exploiter au mieux des pompes paramétriques.

Enfin, dans une dernière partie, j'étudie le comportement d'un tel système avec des éléments inductifs, afin de réaliser des termes hamiltoniens nécessaires pour un encodage de l'information quantique sur des états de chats de Schrödinger, par pompage paramétrique. Le circuit étudié, le modulateur en anneau de jonctions Josephson (*Josephson Ring Modulator*), est d'ores et déjà connu et utilisé pour réaliser de l'amplification ou de la conversion de fréquences. J'étudie ici une variante asymétrique de ce circuit, nommée modulateur asymétrique en anneau de jonctions Josephson (*Asymmetric Josephson Ring Modulator*), qui devrait permettre de réaliser les termes nécessaires à un encodage sur des états de chats de Schrödinger par pompage paramétrique tout en assurant l'absence d'une partie des termes néfastes par symétrie.

Abstract

In this thesis, we investigate the behavior of Josephson circuits under the action of strong microwave drives. Josephson circuits in the quantum regime are a building block to emulate a variety of Hamiltonians, useful to process quantum information. We are here considering a transmon device, made of a Josephson junction and a capacitor in parallel. Through numerical simulations and comparison with experimental results, we show that these drives lead to an instability which results in the escape of the circuit state into states which are no longer confined by the Josephson cosine potential. When the transmon occupies such states, the circuit behaves as if the junction had been removed and all non-linearities are lost, which translates into limitations on the emulated Hamiltonian strengths.

In a second part, we propose and study an alternative circuit consisting of a transmon device with an extra inductive shunt, providing a harmonic confinement. This circuit is found to be stable for all pump powers. The dynamics of this circuit is also well captured by a time-averaged model, providing a useful tool for analytical investigation and fast numerical simulations.

We developed a novel numerical approach that avoids the built-in limitations of perturbative analysis to investigate the dynamical behavior of both of these circuits. This approach, based on the Floquet-Markov theory, resulted in a modular simulation framework which can be used to study other Josephson-based circuits.

Last, we study the properties of an asymmetric version of the Josephson Ring Modulator, a circuit currently used for amplification and conversion, as a more robust source of non-linearity to engineer two-photon and four-photon interaction Hamiltonians required for the cat-state encoding of quantum information.

Remerciements

Je souhaite tout d'abord remercier mon directeur de thèse, Mazyar Mirrahimi, pour son encadrement et les échanges scientifiques enrichissant tout au long de ces trois années. Je souhaite également remercier mon co-directeur de thèse, Zaki Leghtas avec qui c'était un grand plaisir de travailler et qui m'a beaucoup appris.

Je tiens ensuite à remercier les membres du jury, Olivier Buisson et Serge Florens qui ont accepté d'être mes rapporteurs.

Je remercie l'ensemble des chercheurs permanents, post-doctorants et doctorants de l'équipe QUANTIC à l'INRIA ainsi que l'équipe des expérimentateurs du LPA à l'ENS. Ce travail a grandement bénéficié de cet environnement scientifique de qualité et de l'excellente ambiance au sein de cette équipe. Je remerciais tout particulièrement Gerardo Cardona et Jérémie Guillaud qui ont partagé mon bureau pendant ces années. Je voudrais également remercier Michel Devoret pour m'avoir accueilli dans son équipe à deux reprises pour trois mois. C'était une expérience très enrichissante que de travailler au sein de cette équipe et de pouvoir échanger avec eux sur leurs expériences en cours.

Enfin, je tiens à remercier mes parents et Morgan, pour m'avoir transmis le goût des sciences, et de la physique en particulier, et pour leur constant soutien durant ces trois années.

Contents

1	Introduction	1
1.1	Quantum information processing with superconducting circuits	2
1.2	Superconducting circuits quantization	3
1.2.1	Circuit elements and notations	3
1.2.2	Circuit quantization	6
1.2.3	Useful Hamiltonian transformations	8
1.3	Hamiltonian engineering with parametric pumping	8
1.3.1	Principles of parametric pumping	8
1.3.2	Example of the Josephson Parametric Amplifier	12
1.4	Dissipation engineering	13
1.5	Using a cavity as a logical qubit: cat qubits	15
1.5.1	Two-photon cat qubits encoding	15
1.5.2	Stabilization of the cat-states manifold with dissipation engineering	17
1.5.3	Four-photon pumping extension	18
1.6	Physical realization of cat-pumping interaction with a single Josephson junction	20
1.7	Plan of the manuscript	21
2	Structural instability of driven transmon circuit	25
2.1	Strongly driven transmon coupled to a cavity	26
2.2	Change of frame for numerical simulations	29
2.3	Simulations in the Floquet-Markov framework for weak dissipation . . .	31
2.3.1	Floquet-Markov framework for weak dissipation	31
2.3.2	Numerical simulations of the ac Stark shifts in absence of offset charge	34
2.3.3	Influence of the offset charge	37
2.4	Comparison with experimental data	38
3	Inductively shunted transmon: a solution to dynamical instability	41
3.1	Model of the driven shunted transmon circuit	42
3.2	Simulations in the Floquet-Markov framework for weak dissipation . . .	46
3.3	Rotating-wave approximation results and comparison with numerical sim- ulations	47
3.4	Choice of parameters for the shunted transmon circuit	49
4	Floquet-Markov simulations	53
4.1	Steady-state computation framework	54
4.1.1	Encoding the circuit Hamiltonian	55
4.1.2	Floquet code	60

4.1.3	Running simulations	63
4.2	Analysis code	65
4.2.1	Resonant frequencies of the system	65
4.2.2	Induced Kerr strength	66
5	Asymmetric Josephson Ring Modulator	69
5.1	Josephson Ring Modulator	70
5.1.1	Unshunted Josephson Ring Modulator	70
5.1.2	Josephson Ring Modulator with shunt inductances	72
5.2	Asymmetric Josephson Ring Modulator	75
5.2.1	Circuit Hamiltonian	75
5.2.2	Quantization of the AJRM circuit embedded in a microwave cavity	77
5.3	AJRM for the two-photon and four-photon pumping schemes	80
6	Conclusions and perspectives	85
	Bibliography	I

Chapter 1

Introduction

Contents

1.1 Quantum information processing with superconducting circuits	2
1.2 Superconducting circuits quantization	3
1.2.1 Circuit elements and notations	3
1.2.2 Circuit quantization	6
1.2.3 Useful Hamiltonian transformations	8
1.3 Hamiltonian engineering with parametric pumping	8
1.3.1 Principles of parametric pumping	8
1.3.2 Example of the Josephson Parametric Amplifier	12
1.4 Dissipation engineering	13
1.5 Using a cavity as a logical qubit: cat qubits	15
1.5.1 Two-photon cat qubits encoding	15
1.5.2 Stabilization of the cat-states manifold with dissipation engineering	17
1.5.3 Four-photon pumping extension	18
1.6 Physical realization of cat-pumping interaction with a single Josephson junction	20
1.7 Plan of the manuscript	21

1.1 Quantum information processing with superconducting circuits

A quantum machine is a device whose degrees of freedom and evolution are governed by quantum mechanics. There are insights and some proofs that these machines could exhibit novel capabilities, impossible to realize with classical hardware. They could solve problems which are currently far out of range for classical machines, providing more secure transfer of data over network [1], realize measurements with an unprecedented level of precision [2], generate true and certified random numbers [3] or provide a large advantage for some specific computation problems [4].

In the past, atomic systems, optical systems or trapped ions systems have been investigated as a basis to implement such quantum machines. However, since the first demonstration of a quantum superconducting bit, more than twenty years ago [5, 6], the domain of mesoscopic artificial atoms built out of superconducting quantum circuits became one of the most promising physical system to implement quantum machines. Such circuits can be used to create resonators which store individual microwave photons as well as superconducting quantum bits. All of these circuit elements are intrinsically quantum mechanical, with quantized energy levels with spacing much greater than the energy associated with the temperature (for cryogenic temperatures which are achievable in the laboratory) and in order to properly predict their properties, both the current and voltages should be represented by non-commuting operators. The coherence time of these circuits have improved rapidly and steadily over a few orders of magnitude, now reaching a few milliseconds for the best systems [7, 8, 9, 10, 11]. Contrary to the atomic physics based systems, such superconducting circuits provide greater flexibility in the range of exploitable parameters and in the complexity of the Hamiltonian they can implement. This flexibility let us explore a whole new realm of operating regimes. Moreover, the microwave signals, contrary to the optical ones, are very well controlled with commercial electronic equipment developed for radio-frequency engineering. The nanofabrication processes required to fabricate such quantum superconducting circuits are more and more controlled, so that it becomes possible to fabricate multiple complex systems in parallel, leading to the hope that it will soon be possible to scale such quantum processors with large numbers of qubits and leading to the recent development of many commercial interests (from Google, IBM, Intel or Rigetti Computing).

These properties have made the superconducting quantum circuits domain a very promising framework for quantum information processing. They have already led to multiple experimental proof of concept for quantum machines at small scales (only a handful of physical degrees of freedom or qubits) and recently led to a whole new range of multi-qubits systems exploring the performances of fifty to one hundred qubits and the advances such system could provide over classical hardware. Indeed, multiple previous experiments in the context of quantum information processing with trapped ions, nuclear magnetic resonance (NMR) or cavity quantum electrodynamic with Rydberg atoms have been successfully reproduced with superconducting qubits. In many of these experiments, the properties of the superconducting circuits, such as the controllability and tunability of the coupling strengths or non-linearities, together with the reasonable coherence time, allowed to achieve comparable or better performances than their atomic or optical counterparts. Additionally, the constant progresses on the coherence time of these systems paves the way for many new applications.

However, and despite these successful realizations so far, scaling these systems to a number of degrees of freedom of interest for practical applications, remains an open issue.

Indeed, the next critical step in the development of a quantum information processor is certainly the active error correction, which consists in conceiving a logical qubit, protected against the main information loss channels, relying on multiple physical qubits. Such a logical qubit should reach a regime of coherence time much larger than the underlying physical qubits. However, fault-tolerant quantum computation with protected logical qubits usually comes at the expense of a high cost in terms of hardware, requiring up to thousands of physical qubits for a single logical one. Each of the physical qubits should match with state of the art expectations of its properties (coupling strengths, tunability, coherence time), while avoiding as much as possible the noisy interactions between different subsystems on the same chip.

In this manuscript, I am focusing on using superconducting quantum circuits not as an implementation of a physical qubit, but rather as a way to engineer non-linear interaction Hamiltonians between multiple subsystems (typically two microwave cavities). This is an equivalent of having an (artificial) atom coupled to discrete photon modes in a high quality factor cavity, which is the area of Cavity Quantum ElectroDynamics (CQED) [12]. In the optical version of CQED, one usually drives the cavity with a laser and monitors changes in the cavity transmission resulting from coupling to atoms falling through the cavity. I am considering here a circuit version of this system, where the superconducting circuit plays the role of an artificial atom. As the superconducting circuits are widely tunable, one can finely engineer the interaction between the subsystems [13].

The behavior of such superconducting quantum circuits (Fig. 1.1) and their quantization is rather well understood [14]. However, this is not the case for the regime where one operates them under a strong microwave drive. Indeed, these systems are quantum systems, open systems by nature, possibly with large non-linearities and usually time-dependant. The combination of all these characteristics makes them quite unique and difficult to tackle with the previous approaches from optical or atomic physics. For instance, recent experiments [15] indicate that when a superconducting circuit is driven with a microwave signal beyond the linear response regime, the observed relaxation rates appear to be substantially different from expectations based on the electromagnetic environment of the qubit alone.

This manuscript will focus on investigating the dissipative dynamics of a quantum superconducting circuit under strong microwave drives and its consequences for using such a superconducting circuit as a resource for Hamiltonian engineering in the context of cat-states logical qubit encoding [16].

1.2 Superconducting circuits quantization

1.2.1 Circuit elements and notations

In this manuscript and following the approach from [17], Φ_k denotes the node flux at the node under consideration, defined as

$$\Phi_k = \int_{-\infty}^t V_k(\tau) d\tau \quad (1.1)$$

such that $V_k(t) = \dot{\Phi}_k$ is the voltage at the node. φ_k (small phi) denotes the reduced node flux defined as

$$\varphi_k = \frac{\Phi_k}{\varphi_0} \quad (1.2)$$

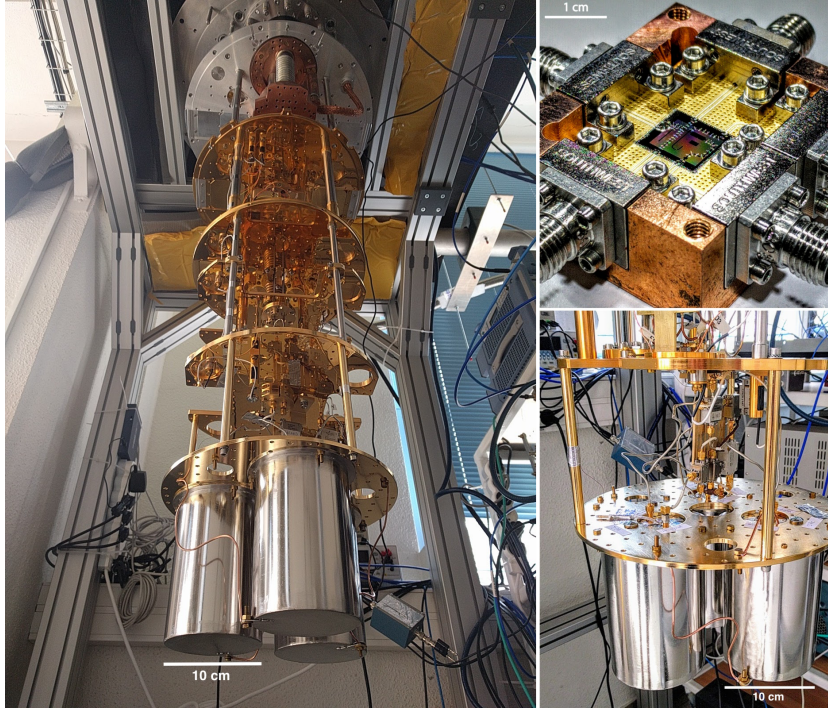


Figure 1.1: **Dilution refrigerator and sample for superconducting circuit experiments.** The left and bottom-right panels picture the dilution refrigerator which was used at ENS by the team of Z. Leghtas for the experiments discussed in this manuscript. Each plate in the dilution fridge is sitting at a different temperature, from 70 K for the upper one to 10 mK for the bottom one where the superconducting circuits under study are sitting. The top-right panel shows a superconducting circuit sample, together with scale.

with $\varphi_0 = \hbar/2e$ being the reduced flux quantum. Q_k denotes the (electric) charge, related to the intensity as $i_k = \dot{Q}_k$.

Throughout this manuscript, bold letters (e.g. Φ) will stand for quantum operators whereas standard letters (e.g. Φ) will represent the classical variable, their classical counterpart.

Here is a brief overview of the circuit elements used throughout this manuscript and their main properties.

Capacitor The associated energy for a capacitor reads

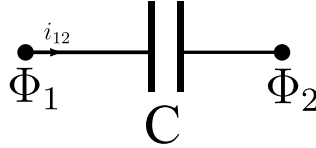
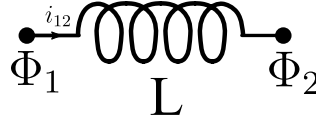
$$\mathcal{U}(\dot{\Phi}_1, \dot{\Phi}_2) = \frac{Q_{12}^2}{2C} = \frac{C}{2} (\dot{\Phi}_1 - \dot{\Phi}_2)^2 = 4E_C \mathbf{n}^2 \quad (1.3)$$

where $E_C = e^2/2C$ is the charging energy and \mathbf{n} is the operator corresponding to the number of Cooper pair tunneling through the capacitor.

Inductor The phase-intensity relation of an inductor is

$$\Phi_1 - \Phi_2 = Li_{12} \quad (1.4)$$

where L is the inductance of the element.

Figure 1.2: Electrical symbol of a capacitor of capacitance C .Figure 1.3: Electrical symbol of an inductor of inductance L .

The associated energy for an inductor reads

$$\mathcal{U}(\varphi_1, \varphi_2) = \frac{1}{2L} (\Phi_1 - \Phi_2)^2 = E_L \frac{(\varphi_1 - \varphi_2)^2}{2} \quad (1.5)$$

where $E_L = \varphi_0^2/L$ is the inductive energy.

Josephson junction Josephson junctions are the main source of non-linearity in quantum electrical circuits. Their phase-intensity relation is

$$i_{12} = I_0 \sin(\varphi_1 - \varphi_2) \quad (1.6)$$

where I_0 is the critical intensity. They behave as a sort of non-linear inductance.

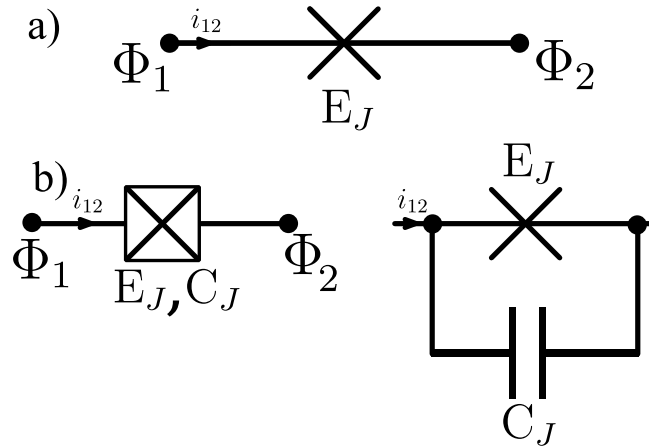


Figure 1.4: Electrical symbols for a Josephson junction. a) Electrical symbol of a pure Josephson junction. b) Due to the layered structure of a real Josephson junction, it always comes with an extra capacitance. Such a Josephson junction is pictured as a boxed Josephson junction, representing a junction with a capacitance in parallel.

Their associated energy reads

$$\mathcal{U}(\varphi_1, \varphi_2) = -E_J \cos(\varphi_1 - \varphi_2) \quad (1.7)$$

where $E_J = I_0 \varphi_0$.

1.2.2 Circuit quantization

I will now briefly recall the main principles and methods for circuit quantization, following the approach from [17, 14]. As an example, let us focus on the simple circuit pictured on Fig. 1.5, consisting of two LC oscillators capacitively coupled.

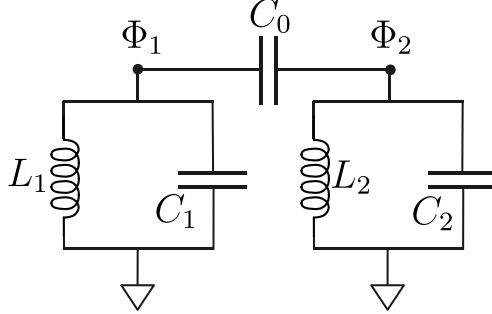


Figure 1.5: **Lumped element circuit of two microwave oscillators capacitively coupled.** This lumped element circuit consists of two microwave cavities (LC oscillators with parameters L_1 , C_1 and L_2 , C_2) capacitively coupled through a capacitor C_0 . The node fluxes $\Phi_{1,2}$ at each end of the coupling capacitor are shown as well.

First, let us write the Lagrangian of the whole system, written in terms of Φ_1 and Φ_2 variables, the node fluxes at each end of the coupling capacitance. The Lagrangian reads

$$\mathcal{L}(\Phi_1, \dot{\Phi}_1, \Phi_2, \dot{\Phi}_2) = \frac{C_1}{2} \dot{\Phi}_1^2 + \frac{C_2}{2} \dot{\Phi}_2^2 + \frac{C_0}{2} [\dot{\Phi}_1 - \dot{\Phi}_2]^2 - \frac{1}{2L_1} \Phi_1^2 - \frac{1}{2L_2} \Phi_2^2 \quad (1.8)$$

where we have used the fact that the node flux at the ground node is equal to zero.

From Eq. (1.8), one can compute the canonical momenta Q_1 , Q_2 associated with the Φ_1 and Φ_2 canonical variables and defined as

$$\begin{cases} Q_1 \triangleq \frac{\partial \mathcal{L}}{\partial \dot{\Phi}_1} = (C_0 + C_1) \dot{\Phi}_1 - C_0 \dot{\Phi}_2 \\ Q_2 \triangleq \frac{\partial \mathcal{L}}{\partial \dot{\Phi}_2} = (C_0 + C_2) \dot{\Phi}_2 - C_0 \dot{\Phi}_1 \end{cases} \quad (1.9)$$

or equivalently

$$\begin{cases} \dot{\Phi}_1 = \frac{1}{C_0 C_1 + C_0 C_2 + C_1 C_2} [(C_0 + C_2) Q_1 + C_0 Q_2] \\ \dot{\Phi}_2 = \frac{1}{C_0 C_1 + C_0 C_2 + C_1 C_2} [C_0 Q_1 + (C_0 + C_1) Q_2] \end{cases} \quad (1.10)$$

At this point, it is worth noting that the canonical momenta Q_1 and Q_2 mix the $\dot{\Phi}_1$ and $\dot{\Phi}_2$ variables.

The Hamiltonian of the system can then be computed as

$$H = Q_1 \dot{\Phi}_1 + Q_2 \dot{\Phi}_2 - \mathcal{L} \quad (1.11)$$

$$H = \frac{C_2 + C_0}{2(C_1C_2 + C_0C_1 + C_0C_2)}Q_1^2 + \frac{C_1 + C_0}{2(C_1C_2 + C_0C_1 + C_0C_2)}Q_2^2 + \frac{C_0}{C_1C_2 + C_0C_1 + C_0C_2}Q_1Q_2 + \frac{1}{2L_1}\Phi_1^2 + \frac{1}{2L_2}\Phi_2^2 \quad (1.12)$$

As the canonical variables \mathbf{Q}_1 , \mathbf{Q}_2 , Φ_1 and Φ_2 satisfy the commutation relations

$$\begin{aligned} [\mathbf{Q}_1, \Phi_1] &= [\mathbf{Q}_2, \Phi_2] = -i\hbar \\ [\mathbf{Q}_1, \Phi_2] &= [\mathbf{Q}_2, \Phi_1] = 0 \\ [\mathbf{Q}_1, \mathbf{Q}_2] &= [\Phi_1, \Phi_2] = 0 \end{aligned} \quad (1.13)$$

we can introduce annihilation and creation operators \mathbf{a} and \mathbf{a}^\dagger (respectively \mathbf{b} and \mathbf{b}^\dagger) to quantize them in the usual promotion to quantum operators, as harmonic oscillator modes (and satisfying $[\mathbf{a}, \mathbf{a}^\dagger] = [\mathbf{b}, \mathbf{b}^\dagger] = 1$ and the cross-commutator being zero). Therefore,

$$\begin{aligned} \mathbf{Q}_1 &= -iQ_{ZPF}^1 (\mathbf{a} - \mathbf{a}^\dagger) \\ \Phi_1 &= \Phi_{ZPF}^1 (\mathbf{a} + \mathbf{a}^\dagger) \\ \mathbf{Q}_2 &= -iQ_{ZPF}^2 (\mathbf{b} - \mathbf{b}^\dagger) \\ \Phi_2 &= \Phi_{ZPF}^2 (\mathbf{b} + \mathbf{b}^\dagger) \end{aligned} \quad (1.14)$$

where

$$\begin{aligned} Q_{ZPF}^1 &= \sqrt{\frac{\hbar}{2Z_1}} \\ \Phi_{ZPF}^1 &= \sqrt{\frac{\hbar Z_1}{2}} \\ Q_{ZPF}^2 &= \sqrt{\frac{\hbar}{2Z_2}} \\ \Phi_{ZPF}^2 &= \sqrt{\frac{\hbar Z_2}{2}} \end{aligned} \quad (1.15)$$

with

$$\begin{aligned} Z_1 &= \sqrt{L_1 (C_1C_2 + C_0C_1 + C_0C_2) / (C_0 + C_2)} \\ Z_2 &= \sqrt{L_2 (C_1C_2 + C_0C_1 + C_0C_2) / (C_0 + C_1)}. \end{aligned} \quad (1.16)$$

The full Hamiltonian of the system then reads

$$\mathbf{H} = \hbar\omega_1 \mathbf{a}^\dagger \mathbf{a} + \hbar\omega_2 \mathbf{b}^\dagger \mathbf{b} - \frac{C_0 Q_{ZPF}^1 Q_{ZPF}^2}{C_1C_2 + C_0C_1 + C_0C_2} (\mathbf{a} - \mathbf{a}^\dagger) (\mathbf{b} - \mathbf{b}^\dagger) \quad (1.17)$$

at the expense of introducing the frequencies of the modes, ω_1 and ω_2 , which can be expressed as function of the capacitances and inductances of the system. The full Hamiltonian \mathbf{H} can then be diagonalized using a Bogoliubov transformation. At this point,

let us note that in this section, we first wrote the Hamiltonian from the Lagrangian and then considered diagonalizing it through a Bogoliubov transformation. We could however have chosen the opposite, first diagonalizing the Lagrangian and then writing the associated Hamiltonian and quantify it.

1.2.3 Useful Hamiltonian transformations

In this section, I will briefly summarize two useful transformations on the Hamiltonian of a superconducting circuit with an additional electromagnetic drive, which will be extensively used in the rest of this manuscript. Let us focus on the following Hamiltonian

$$H = \hbar\omega_a \mathbf{a}^\dagger \mathbf{a} + \hbar\mathcal{A}_p(t) (\mathbf{a} + \mathbf{a}^\dagger) + H_1 (\mathbf{a}, \mathbf{a}^\dagger) \quad (1.18)$$

where ω_a is the frequency of the harmonic mode, $\mathcal{A}_p(t) = A_p \cos(\omega_p t)$ is the complex time-dependent amplitude of a pump applied onto this system and H_1 is an extra generic Hamiltonian term entering the description of the system.

First, let us introduce $\xi(t)$ such that

$$\frac{d\xi}{dt} = -i\omega_a \xi - i\mathcal{A}_p(t) \quad (1.19)$$

and define a displaced mode, $\tilde{\mathbf{a}}$ as

$$\tilde{\mathbf{a}} = \mathbf{a} - \xi(t), \quad (1.20)$$

which is obtained with a displacement $\mathbf{D}_{\xi(t)} = \exp(\xi(t)^* \mathbf{a} - \xi(t) \mathbf{a}^\dagger)$.

Then, the Hamiltonian \tilde{H} of the system, in this displaced frame, reads

$$\tilde{H} = \hbar\omega_a \tilde{\mathbf{a}}^\dagger \tilde{\mathbf{a}} + H_1 (\tilde{\mathbf{a}} + \xi(t), \tilde{\mathbf{a}}^\dagger + \xi^*(t)) \quad (1.21)$$

Finally, the Hamiltonian in the rotating frame of the harmonic oscillator (obtained by a unitary transform $\mathbf{U} = e^{i\omega_a \tilde{\mathbf{a}}^\dagger \tilde{\mathbf{a}} t}$) is given by

$$\tilde{H}_{\text{int}} = H_1 (\tilde{\mathbf{a}} e^{-i\omega_a t} + \xi(t), \tilde{\mathbf{a}}^\dagger e^{i\omega_a t} + \xi^*(t)). \quad (1.22)$$

1.3 Hamiltonian engineering with parametric pumping

In this manuscript, I investigate the behavior of circuits mediating parametric interactions between multiple modes in the large pumping regime. Indeed, by considering a non-linearity coupling multiple microwave modes and adding a periodic modulation on them (later called the ‘‘pump’’), one can engineer and tailor specific interactions between the considered modes [18]. Such parametric interactions can be used for amplification using single-mode or two-mode squeezing, for frequency conversion or for more elaborate multi-photon interactions between the considered modes, as I will briefly review in this section.

1.3.1 Principles of parametric pumping

Parametric interactions are a tool of paramount importance in order to design Hamiltonian interactions with a full control on the strength of the terms as well as being able to turn on and off the interaction easily. As pictured on Fig. 1.6, the core idea

is not to directly couple the two modes and physically engineer the parameters of the system to control the interaction term, but rather to use an auxiliary mode (the pump mode) which will mediate the interaction. Provided that the pump frequency verifies a specific frequency matching condition, the resulting interaction Hamiltonian can be obtained from rotating-wave approximation [19]. Moreover, provided that the pump is non-resonant and that its bandwidth is larger than the one from other modes, the pump can be considered in the “stiff pump regime”, which is equivalent to consider that the pump is not affected by the interaction process and can therefore be treated classically. Such framework has the major advantage compared to *in-situ* interactions engineering that the pump drive fully controls both the strength as well as the phase of the interaction terms, allowing for near real-time control.

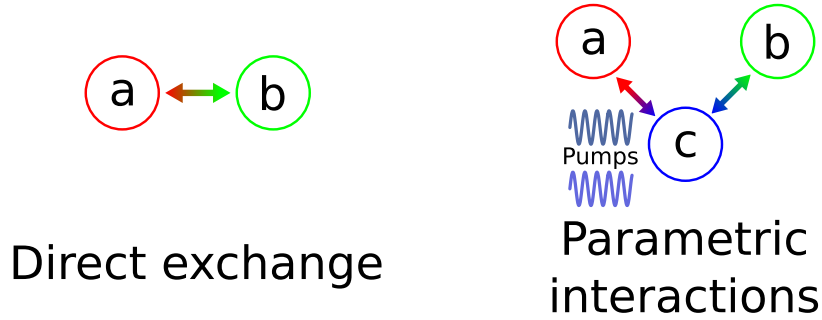


Figure 1.6: **Interaction engineering through parametric interactions.** Instead of considering a direct interaction between two modes a and b , we are using a third mode, c , to mediate interactions between a and b . This third mode is coupled to one or more AC drives (oscillating pumps) whose frequencies and amplitudes control the parametric interaction terms in the Hamiltonian.

Formally, let us consider the simplest Hamiltonian with two electromagnetic modes and a direct coupling between them,

$$H = \hbar\omega_a \mathbf{a}^\dagger \mathbf{a} + \hbar\omega_b \mathbf{b}^\dagger \mathbf{b} + g (\mathbf{a}\mathbf{b}^\dagger + \mathbf{a}^\dagger \mathbf{b}). \quad (1.23)$$

In an interaction picture with respect to the harmonic oscillator part of this Hamiltonian, it becomes

$$H = g \left(e^{i(\omega_b - \omega_a)t} \mathbf{a}\mathbf{b}^\dagger + e^{-i(\omega_b - \omega_a)t} \mathbf{a}^\dagger \mathbf{b} \right). \quad (1.24)$$

and the coupling term will remain in a rotating-wave approximation if and only if the two frequencies of the modes are detuned by a frequency mismatch much smaller than the coupling strength g . On the contrary, let us now consider a parametric interaction scheme with an extra mode \mathbf{c} . Assuming there exists a physical implementation of it, the Hamiltonian could then read

$$H = \hbar\omega_a \mathbf{a}^\dagger \mathbf{a} + \hbar\omega_b \mathbf{b}^\dagger \mathbf{b} + \hbar\omega_c \mathbf{c}^\dagger \mathbf{c} + g (\mathbf{a}\mathbf{b}^\dagger \mathbf{c} + \mathbf{a}^\dagger \mathbf{b}\mathbf{c}^\dagger) + \hbar\mathcal{A}_p(t) (\mathbf{c} + \mathbf{c}^\dagger) \quad (1.25)$$

where $\mathcal{A}_p(t) = A_p \cos(\omega_p t)$ is the amplitude of the parametric pump on the \mathbf{c} mode. Considering a coherent displacement of the \mathbf{c} mode to take into account the effect of the parametric pump (following section 1.2.3), the Hamiltonian reads

$$H = \hbar\omega_a \mathbf{a}^\dagger \mathbf{a} + \hbar\omega_b \mathbf{b}^\dagger \mathbf{b} + \hbar\omega_c \tilde{\mathbf{c}}^\dagger \tilde{\mathbf{c}} + g (\mathbf{a}\mathbf{b}^\dagger (\tilde{\mathbf{c}} + \xi(t)) + \mathbf{a}^\dagger \mathbf{b} (\tilde{\mathbf{c}}^\dagger + \xi(t)^*)). \quad (1.26)$$

In the interaction picture with respect to the harmonic part, the Hamiltonian reads

$$\tilde{H} = \frac{A_p g}{2(\omega_c - \omega_p)} \left(e^{i(\omega_b - \omega_a - \omega_p)t} \mathbf{a} \mathbf{b}^\dagger + e^{-i(\omega_b - \omega_a - \omega_p)t} \mathbf{a}^\dagger \mathbf{b} \right) \quad (1.27)$$

where a partial trace has been used on the mode $\tilde{\mathbf{c}}$ which is very close to the vacuum state. With such a parametric scheme, we recover an interaction term between \mathbf{a} and \mathbf{b} of the form of Eq. (1.24) where

- The resonance condition for this interaction to remain under rotating wave approximations is now

$$\omega_p = \omega_b - \omega_a. \quad (1.28)$$

It is important to note here that this frequency matching condition is a condition on the parametric pump frequency ω_p (which can be tuned easily) and no longer impose a frequency match for the two electromagnetic modes.

- The coupling amplitude is no longer g but is scaled by a factor $A_p/2(\omega_c - \omega_p)$. Therefore, increasing the pump strength increases the interaction strength.

In the previous calculation, I used an auxiliary \mathbf{c} mode for clarity. However, the same parametric scheme could be achieved by pumping one of the two initial electromagnetic modes (\mathbf{a} for example) and having an initial interaction with an extra power in this mode (an interaction of the form $\mathbf{a}^2 \mathbf{b}^\dagger + \text{h.c.}$ for instance).

Various superconducting circuits implementing parametric interactions have been proposed to achieve amplification and conversion [20]. Starting from the Josephson Parametric Amplifier (JPA) with a single Josephson junction or two Josephson junctions in a SQUID configuration [21, 22, 23] which achieve amplification through single-mode squeezing with an interaction Hamiltonian of the form

$$H_{\text{int}} = \hbar g \left[\mathbf{a}^2 + \left(\mathbf{a}^\dagger \right)^2 \right] \quad (1.29)$$

more refined circuits have been proposed. Among such circuits is the Josephson Ring Modulator (JRM) [24] (whose mode of operation is presented in details in Chapter 5) which consists in a loop of four Josephson junctions and offers an amplification through two-mode squeezing, using three-wave mixing terms of the form

$$H_{\text{int}} = \hbar g \left(\mathbf{a} \mathbf{b} + \mathbf{a}^\dagger \mathbf{b}^\dagger \right) \quad (1.30)$$

As demonstrated in [25, 26], the stability of the Josephson Ring Modulator circuit can be further improved using inductive shunts and the resulting circuit can be used to engineer squeezing interaction Hamiltonian as well as conversion processes along with the quantum limited amplification. Similar methods have been used in [27] to implement a Q-SWITCH with a conversion Hamiltonian of the form

$$H_{\text{int}} = \hbar g \left[\mathbf{a} \mathbf{b}^\dagger + \mathbf{a}^\dagger \mathbf{b} \right] \quad (1.31)$$

which can be used to transfer the state of an electromagnetic mode of a cavity to a propagating electromagnetic mode or another remote cavity.

Parametric methods are also ubiquitous to the cat states encoding proposal from [16] which requires a two-photon or four-photon exchange Hamiltonian of the form

$$H_{\text{int}} = \hbar g \left[\mathbf{a}^d \mathbf{b}^\dagger + \left(\mathbf{a}^\dagger \right)^d \mathbf{b} \right] \quad (1.32)$$

where $d = 2$ or $d = 4$. Superconducting circuits relying on parametric methods can engineer such Hamiltonians for the two-photon exchange process [28] or using higher order rotating-wave approximations to achieve four-photon exchange process [29].

Finally, these methods are not limited to standing electromagnetic modes but can also be used for amplification along a transmission line with travelling modes, such as in the Josephson Traveling-Wave Parametric Amplifier (JTWPA) [30].

At this point, it is worth noting that, usually, the strength of the engineered Hamiltonian scales with the amplitude of the pump drive mediating the parametric interaction. Therefore, one usually wishes to increase the pump power, in order to reach better operating regimes. This, however, does not in general experimentally yield improvements indefinitely. Indeed, the interaction terms in the Hamiltonian which are selected thanks to the parametric pumping are only a subset of all the possible terms. For instance, in the strong pump regime, such terms which were at first either negligible or discarded through rotating-wave approximations [19] might actually no longer be negligible and should be taken into account. Additionally, in the strong pump regime, the system can suffer from phase slips or symmetry breaking (the total flux can no longer be symmetrically divided across chains of Josephson junctions)[31], quasi-particle creation due to the strong electromagnetic fields breaking Cooper pairs[32, 33], or simply degrading the coherence times of the modes [34] (possibly through heating of the chip or by inducing other decay mechanisms which are not fully understood).

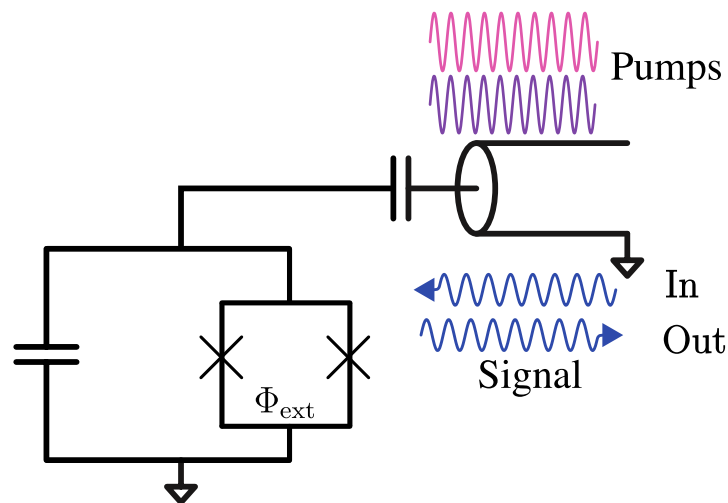


Figure 1.7: **Josephson Parametric Amplifier circuit.** The circuit consists of a RF Superconducting Quantum Interference Device (SQUID) with a parallel capacitor, capacitively coupled to a transmission line. The external flux threading the loop, Φ_{ext} can be used to adjust the frequency of the resonator, ω_a . Pumps (with time-dependent amplitude $\mathcal{A}_1(t)$ and $\mathcal{A}_2(t)$ and frequencies ω_1 and ω_2) are sent through the transmission line to achieve parametric pumping. A signal, at frequency ω_a (matched with the RF-SQUID mode frequency) is sent through the same transmission line. Such a device can be used to achieve amplification through single-mode squeezing with the reflected signal, coming out of the transmission line.

1.3.2 Example of the Josephson Parametric Amplifier

As a real world example, let us focus on the simple case of the Josephson Parametric Amplifier (JPA) whose circuit is pictured on Fig. 1.7. First, let us note that the Josephson junctions loop from the circuit is actually equivalent to a tunable Josephson junction. Assuming we operate at a fixed value of Φ_{ext} , the Hamiltonian of this system reads, considering only up to quartic term in the Josephson cosine potential expansion,

$$H = \hbar\omega_a \mathbf{a}^\dagger \mathbf{a} + K (\mathbf{a} + \mathbf{a}^\dagger)^4 + \hbar\mathcal{A}_1(t) (\mathbf{a} + \mathbf{a}^\dagger) + \hbar\mathcal{A}_2(t) (\mathbf{a} + \mathbf{a}^\dagger) \quad (1.33)$$

where K is a constant which can be expressed in terms of the capacitive and Josephson energy of the circuit elements, $\mathcal{A}_1(t) = A_1 \cos(\omega_1 t)$ and $\mathcal{A}_2(t) = A_2 \cos(\omega_2 t)$ are the time-dependent pump amplitudes.

Following the approach from equations (1.23)-(1.27), the Hamiltonian expressed in terms of displaced modes and in the interaction picture with the harmonic oscillator term reads

$$\tilde{H} = K' (\mathbf{a}e^{-i\omega_a t} + \xi_1 e^{-i\omega_1 t} + \xi_2 e^{-i\omega_2 t} + \text{h.c.})^4 \quad (1.34)$$

with K' a renormalized coupling strength, proportional to the pump amplitude, and $\xi_{1,2} = A_{1,2}/2(\omega_a - \omega_{1,2})$.

Assuming a frequency matching condition

$$\omega_1 + \omega_2 = 2\omega_a, \quad (1.35)$$

the remaining term of interest after a rotating-wave approximation is

$$12K' (\mathbf{a}^2 \xi_1^* \xi_2^* + \text{h.c.}) \quad (1.36)$$

which can be used to implement amplification through single-mode squeezing. At this point, let us note that if we had only considered a single pump, the frequency matching condition would have been $\omega_1 = \omega_a$ therefore requiring to have the pump in resonance with the oscillator mode and no longer being able to rely on the stiff pump approximation. On the contrary, using two pumps here allows us to choose two pumps far detuned from the oscillator frequency (one red-detuned and the other one blue-detuned) while satisfying the frequency matching condition.

However, the term from Eq. (1.36) is not the only one remaining under rotating-wave approximation. Indeed, this term is coming from a fourth-order term in the expansion of the cosine potential, along with terms of the form $\xi_{1,2}^* \xi_{1,2} (\mathbf{a}^\dagger)^2 \mathbf{a}^2$ (Kerr-type terms). They would be resonant under the frequency matching condition Eq. (1.35) and can be detrimental depending on the envisioned application for the circuit. Additionally, one should note that these terms, just as the main term of interest for amplification through single-mode squeezing, have their amplitude proportional to the pump amplitudes.

These limitations when pushing the pump power lead to the theoretical investigation of the behavior of such systems in the strong pump regime, with a particular focus on the loss of the non-linearity when the pump strength becomes too high [35, 36, 37, 38, 39] or the reduction of the coherence time of the non-linear resonator as a function of the mean photon occupancy (T_1 versus \bar{n}) [40]. These previous analysis were relying on simplified models of the superconducting circuit in use, relying on Jaynes-Cumming model (only considering the two lowest state of the non-linear resonator), generalized Jaynes-Cumming (considering a few states of the non-linear resonator) or

Duffing approximation (considering the non-linearity only to some order of its Taylor expansion).

Throughout this manuscript, I will investigate the steady state dynamics of such a non-linear resonator (transmon circuit) coupled to a linear resonator (microwave cavity) and a parametric pump in the strong pumping regime. I am proposing a Floquet-Markov framework to carry out numerical investigation of this system in the strong pumping regime. This scheme and the associated change of basis let me consider a large transmon Hilbert space truncature, able to capture highly excited transmon states, and avoid rotating-wave approximations, which are not valid in this setting. The results presented in this thesis, although presented in the context of cat-states encoding, can be generalized to a wide variety of the previously mentioned parametric systems with a pump mediating a non-linear interaction.

1.4 Dissipation engineering

The parametric methods presented in section 1.3 are of paramount interest to engineer specific dissipation terms, in particular non-linear dissipations or turning on and off dissipations on the fly in experiments. Indeed, parametric methods can be used to engineer a specific and controllable non-linear interaction between two electromagnetic modes. Then, in the limit where one of the two modes is strongly dissipative, adiabatic elimination procedures [41] can be used in order to get a simplified model without this extra dissipative mode. The engineered non-linear interaction between the two modes then turn into a non-linear dissipative terms for the remaining electromagnetic mode.

In the QUANTIC team at INRIA Paris, such methods are used and implemented in particular in the context of cat-states encoding, which I will more extensively describe in section 1.5 and which will be used as a recurring example for parametric methods and dissipation engineering considerations throughout this manuscript. I will now briefly describe the adiabatic elimination procedure for the specific case of the two-photon interaction

$$H_{\text{int}} = i\hbar g_{2\text{-ph}} \left[\left(\mathbf{a}^\dagger \right)^2 \mathbf{b} + \mathbf{a}^2 \mathbf{b}^\dagger \right] \quad (1.37)$$

which results in a non-linear dissipation of photons in pairs. Such an engineered dissipation is at the core of the two-photon cat-states encoding and the interest of such dissipation will be clear in section 1.5.

Starting from the two modes Lindblad master equation

$$\frac{d\rho}{dt} = u \left[\mathbf{b}^\dagger - \mathbf{b}, \rho \right] + \kappa_b D[\mathbf{b}](\rho) - ig_{2\text{-ph}} \left[\left(\mathbf{a}^\dagger \right)^2 \mathbf{b} + \mathbf{a}^2 \mathbf{b}^\dagger, \rho \right] + \mathcal{L}_a(\rho) \quad (1.38)$$

where $D[\mathbf{A}](\rho) = \mathbf{A}\rho\mathbf{A}^\dagger - (\mathbf{A}^\dagger\mathbf{A}\rho + \rho\mathbf{A}^\dagger\mathbf{A})/2$, u is the amplitude of the drive on the readout mode, κ_b is the (large) dissipation rate of the readout mode, $g_{2\text{-ph}}$ is the two-photon interaction rate and \mathbf{a} and \mathbf{b} are the storage (with a high quality factor) and readout (very dissipative) modes annihilation operators. Here, $\mathcal{L}_a(\rho)$ models parasitic Lindblad terms acting on the storage mode (for instance single photon dissipation, self-Kerr terms or dephasing noise). $\mathcal{L}_a(\rho)$ is supposed to be small compared to the other terms. Here, I assume that $g_{2\text{-ph}}/\kappa_b$ is small enough to be in the regime where the results from [41] are valid.

Eq. (1.38) can be recasted into

$$\frac{d\rho}{dt} = \underbrace{-ig_{2\text{-ph}} \left[\left(\mathbf{a}^2 - \alpha_{2\text{-ph}}^2 \right)^\dagger \mathbf{b} - \left(\mathbf{a}^2 - \alpha_{2\text{-ph}}^2 \right) \mathbf{b}^\dagger, \rho \right]}_{\varepsilon \mathcal{L}_{\text{int}}(\rho)} + \underbrace{\kappa_b D[\mathbf{b}](\rho)}_{\mathcal{L}_b(\rho)} + \varepsilon \mathcal{L}_a(\rho) \quad (1.39)$$

at the expense of introducing $\alpha_{2\text{-ph}} = \sqrt{u/ig_{2\text{-ph}}}$.

The adiabatic elimination theorem from [41] can be applied on Eq. (1.39), as the dynamics can be split into two time scales:

- A rapid convergence of the fastest subsystem towards a given subspace (given by the dynamics in absence of coupling, with the time scale κ_b),
- A slow evolution of the other subsystem while maintaining the fastest subsystem in the vicinity of its steady state in absence of coupling.

Indeed, with $\varepsilon = g_{2\text{-ph}}/\kappa_b$,

- $\mathcal{L}_b(\rho) = \kappa_b D[\mathbf{b}](\rho)$ is the fast dynamics
- $\varepsilon \mathcal{L}_a$ is the slow dynamics (which is supposed to be at most of order ε)
- $\varepsilon \mathcal{L}_{\text{int}} = -ig_{2\text{-ph}} \left[\left(\mathbf{a}^2 - \alpha_{2\text{-ph}}^2 \right)^\dagger \mathbf{b} - \left(\mathbf{a}^2 - \alpha_{2\text{-ph}}^2 \right) \mathbf{b}^\dagger, \rho \right]$ is an interaction Lindbladian

which verify the previous condition for the validity of the results from [41]. Let us note that in absence of coupling between the two modes ($g_{2\text{-ph}} = 0$), the fast dynamics (of the mode \mathbf{b}) rapidly converges to a coherent state $|\beta\rangle$ given by $\beta = 2u/\kappa_b$. In presence of the coupling, however, the steady state lies in $\text{Span}\{|\pm\alpha_{2\text{-ph}}\rangle\} \otimes |0\rangle$.

Following the analysis from [41] and [42] and their notations, the steady state of the fast dynamics $\bar{\rho}_b$ is given by $\bar{\rho}_b = |0\rangle\langle 0|$. Then, the master equation at second order is given by¹

$$\frac{d\rho_s}{dt} = \frac{4g_{2\text{-ph}}^2}{\kappa_b} D\left[\mathbf{a}^2 - \alpha_{2\text{-ph}}^2\right](\rho_s) + \mathcal{L}_a(\rho_s) + O(\varepsilon^3) \quad (1.40)$$

where ρ_s is a reduced density matrix. In absence of parasitic \mathcal{L}_a Lindbladian, the reduced density matrix ρ_s obeys a master equation of the form

$$\frac{d\rho}{dt} = \kappa_{2\text{-ph}} D\left[\mathbf{a}^2 - \alpha_{2\text{-ph}}^2\right](\rho) \quad (1.41)$$

with $\kappa_{2\text{-ph}} = 4g_{2\text{-ph}}^2/\kappa_b$. This master equation and its implication for cat states pumping will be detailed in section 1.5.2.

As shown by Eq. (1.41), after an adiabatic elimination of the most dissipative mode, the non-linear parametric interaction from Eq. (1.38) translates in a non-linear two-photon dissipation on the remaining storage mode.

Moreover, in absence of \mathcal{L}_a term, the full state of the system can be recovered from the fast dynamics steady state $\bar{\rho}_b$ and the reduced density matrix ρ_s using the following Kraus map

$$K(\rho_s) = \rho_s \otimes \bar{\rho}_b + 2ig_{2\text{-ph}} \left[\left(\rho_s \left(\mathbf{a}^{\dagger 2} - \alpha_{2\text{-ph}}^{*2} \right) \right) \otimes |0\rangle\langle 1| - \left(\left(\mathbf{a}^2 - \alpha_{2\text{-ph}}^2 \right) \rho_s \otimes |1\rangle\langle 0| \right) \right]. \quad (1.42)$$

¹In general, the reduced system Hilbert space (in which ρ_s lies) is not the same as the slow dynamics Hilbert space (denoted by the index a). One should apply a Kraus map whose expression is given in Eq. 1.42 and then a partial trace to pass from the reduced system to the slow dynamics space.

At this point, it is worth noting that this Kraus map reduces to $\rho_s \otimes \bar{\rho}_b$ in the steady state of the system. Therefore, the Kraus map should be taken into account during the transient evolution but not in the steady state, where the ρ_s reduced density matrix coincides with the density matrix of the storage mode.

1.5 Using a cavity as a logical qubit: cat qubits

In [11], M. H. Devoret and R. J. Schoelkopf distinguish seven steps towards quantum information processing, from the realization of simple operations on individual physical qubits to the realization of a full fault-tolerant quantum computation on a large-scale qubits system. Systems based on superconducting qubits have successfully reached the third step, that is to be able to perform quantum nondemolition measurements (called QND measurements) for control and error correction purposes, and they are on the edge of reaching the fourth step, that is to be able to control logical qubits with lifetimes larger than individual physical qubits.

Classical information processing relies on storing the information on bits (two-states systems) and error correction is based on redundantly encoding the information and performing majority votes. In quantum information processing, information is stored on a qubit, a two-level system, quantum analogous of the classical information bit. The qubit being a physical system coupled to a noisy environment, it also experiences errors which should be corrected. These errors can be modelled as *bit-flip* errors (analogous to the classical bit inversion error, swapping the $|0\rangle$ and $|1\rangle$ states) and *phase-flips* errors (turning the $|0\rangle + |1\rangle$ state into $|0\rangle - |1\rangle$). In the quantum world, the no-cloning theorem and measurement back action prevents any scheme based on copying the information and exploiting redundancy (through majority votes) as simply as in the classical world. Therefore, more sophisticated error-correction schemes have to be implemented.

In order to implement quantum error correction, one can encode the (logical) qubit state on multiple (physical) qubits, which is the approach used by the Steane code[43] for instance. On the contrary, in this manuscript, I will focus on another approach relying on storing the information in a single high dimensional Hilbert space, such as an harmonic oscillator Hilbert space. The cat-code encoding presented in the next subsection uses this approach and relies on encoding the state of the qubit on superposition of coherent states. I will present the principle of the cat-state encoding and a cat-pumping scheme to further confine the state of the logical qubit to a manifold spanned by the useful coherent states, therefore extending the upper bound on the lifetime of the qubit. Then, I will present the current state of the art experiment for an experimental realization of this encoding scheme and an extension to a larger manifold allowing for better error tracking through carefully chosen projective measurements.

1.5.1 Two-photon cat qubits encoding

Cat qubits encoding encodes quantum information redundantly in the Hilbert space of a quantum harmonic oscillator. Indeed, given a complex number α , let us consider the coherent state $|\alpha\rangle$ defined as

$$|\alpha\rangle = e^{-|\alpha|^2} \sum_{n \geq 0} \frac{\alpha^n}{n!} |n\rangle, \quad (1.43)$$

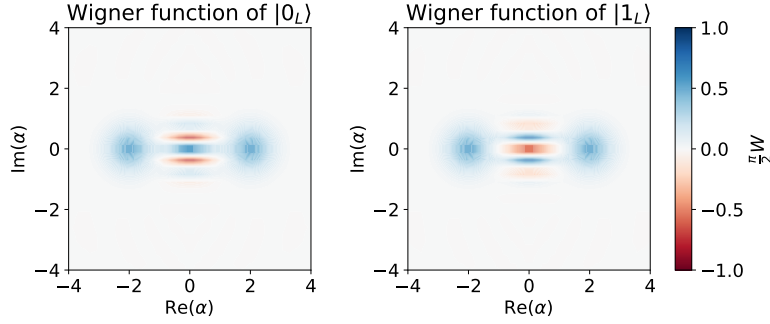


Figure 1.8: **Wigner representation of the two cat states used as a basis for defining a logical qubit**, $|0_L\rangle = |\mathcal{C}_\alpha^+\rangle = \mathcal{N}^+ (|\alpha\rangle + |-\alpha\rangle)$ and $|1_L\rangle = |\mathcal{C}_\alpha^-\rangle = \mathcal{N}^- (|\alpha\rangle - |-\alpha\rangle)$. The fringes in the center of the figure are a confirmation that these are coherent superpositions of two states (called *cat* states). The sign of the center fringe indicates the parity of the cat state.

where $|n\rangle$ is the n -th Fock state of the harmonic oscillator. One can consider the superposition of such coherent states, called *cat* states,

$$|\mathcal{C}_\alpha^\pm\rangle = \mathcal{N}^\pm (|\alpha\rangle \pm |-\alpha\rangle), \quad \mathcal{N}^\pm = \frac{1}{\sqrt{2(1 \pm e^{-2|\alpha|^2})}}. \quad (1.44)$$

At this point, one might note that the state $|\mathcal{C}_\alpha^+\rangle$ (respectively $|\mathcal{C}_\alpha^-\rangle$) is a superposition of Fock states with even (odd) photon numbers. Therefore, these two states are orthogonal and can be used as a basis for encoding quantum information. Moreover, since $|\langle -\alpha | \alpha \rangle|^2 = e^{-2|\alpha|^2}$, when α is large enough (in practice, for $\alpha \geq 2$), these states can be considered orthogonal and the difference between \mathcal{N}^+ and \mathcal{N}^- can be neglected, effectively taking a normalization factor $\mathcal{N} = 1/\sqrt{2}$. Following [44], let us define a logical qubit as

$$\begin{aligned} |0_L\rangle &= |\mathcal{C}_\alpha^+\rangle = \mathcal{N}^+ (|\alpha\rangle + |-\alpha\rangle) \\ |1_L\rangle &= |\mathcal{C}_\alpha^-\rangle = \mathcal{N}^- (|\alpha\rangle - |-\alpha\rangle) \end{aligned} \quad (1.45)$$

The Wigner function of these two logical qubit states is shown in Fig. 1.8.

Under the action of an annihilation operator \mathbf{a} , these states evolve as

$$\begin{aligned} \mathbf{a} |0_L\rangle &= \alpha \frac{\mathcal{N}^+}{\mathcal{N}^-} |1_L\rangle \approx \alpha |1_L\rangle \\ \mathbf{a} |1_L\rangle &= \alpha \frac{\mathcal{N}^-}{\mathcal{N}^+} |0_L\rangle \approx \alpha |0_L\rangle \end{aligned} \quad (1.46)$$

which is the action of a *bit-flip* error. On the contrary, in a heuristic way, a *phase-flip* error would involve an operator coupling $|0_L\rangle + |1_L\rangle \propto |\alpha\rangle$ and $|0_L\rangle - |1_L\rangle \propto |-\alpha\rangle$. As $|\langle -\alpha | \alpha \rangle|^2 = e^{-2|\alpha|^2}$, one might expect (as detailed in the next subsection) that these errors could be greatly reduced. This would leave the system with a single main channel of errors: bit-flip type errors.

1.5.2 Stabilization of the cat-states manifold with dissipation engineering

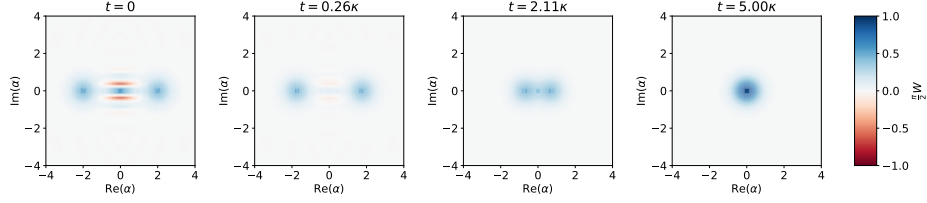


Figure 1.9: **Wigner representation of the $|0_L\rangle$ cat states at different time steps when evolving under the collapse operator $\sqrt{\kappa}\mathbf{a}$ with a the annihilation operator for this photon mode.** As a result of the action of this collapse operator, the coherent superposition first decays to a statistical mixture of the underlying coherent states $|\pm\alpha\rangle$. Then, as the coherent states $|\pm\alpha\rangle$ deterministically decay to the vacuum state $|0\rangle$ as $|\alpha(t) = \alpha e^{-\kappa t/2}\rangle$ with κ the dissipation rate, the whole mixture collapses to the vacuum state, therefore losing the encoded information.

The basis defined in section 1.5.1 can be used to store quantum information. However, this encoding on coherent states is still sensitive to the deterministic relaxation of energy, as shown on Fig. 1.9. Indeed, in presence of dissipation modelled by a collapse operator $\sqrt{\kappa}\mathbf{a}$ with κ the dissipation rate and \mathbf{a} the annihilation operator of the harmonic oscillator, any coherent state $|\alpha\rangle$ would decay towards the vacuum state as $|\alpha(t) = \alpha e^{-\kappa t/2}\rangle$. This deterministic energy relaxation could be overcome if one had a scheme to stabilize the manifold $\text{Span}\{|\alpha\rangle, |-\alpha\rangle\}$. Such a method was proposed in [16, 28] using a reservoir engineering technique. In this method, an auxiliary (harmonic oscillator) mode is taken into account and a non-linear interaction between this auxiliary mode and the storage mode is tailored in order to pump back energy into the storage mode of the cat qubits.

Let us consider the following master equation modelling a d -photon drive with an amplitude $\varepsilon_{d\text{-ph}}$ and a d -photon dissipation with a rate $\kappa_{d\text{-ph}}$,

$$\frac{d\rho}{dt} = \left[\varepsilon_{d\text{-ph}} (\mathbf{a}^\dagger)^d - \varepsilon_{d\text{-ph}} \mathbf{a}^d, \rho \right] + \kappa_{d\text{-ph}} D[\mathbf{a}^d](\rho) \quad (1.47)$$

where ρ is the density matrix of the system and $D[\mathbf{X}](\rho) = \mathbf{X}\rho\mathbf{X}^\dagger - (\mathbf{X}^\dagger\mathbf{X}\rho + \rho\mathbf{X}^\dagger\mathbf{X})/2$.

When $d = 1$, Eq. (1.47) represents the action of a simple coherent drive with dissipation and it is a known result that the system converges towards $|\alpha_{1\text{-ph}} = 2\varepsilon_{1\text{-ph}}/\kappa_{1\text{-ph}}\rangle$.

Let us now focus on the $d = 2$ case, modelling the coupling of a quantum harmonic oscillator mode to a reservoir while restricting the exchanges of photons to be only in pairs. In this case, Eq. (1.47) can be written in an equivalent form

$$\frac{d\rho}{dt} = \kappa_{2\text{-ph}} D[\mathbf{a}^2 - \alpha_{2\text{-ph}}^2](\rho) \quad (1.48)$$

where $\alpha_{2\text{-ph}} = \sqrt{2\varepsilon_{2\text{-ph}}/\kappa_{2\text{-ph}}}$. From the form of Eq. (1.48), it is clear that, whatever the initial state of the system, it converges towards a manifold spanned by two different coherent states, $\rho_\infty \in \text{Span}\{|\alpha_{2\text{-ph}}\rangle, |-\alpha_{2\text{-ph}}\rangle\}$. This is illustrated by the (classical) trajectories of the system shown on Fig. 1.10. As proven in [45], starting from an initial coherent state $\rho(0) = |\alpha(0)\rangle\langle\alpha(0)|$, the system converges to $|\alpha_{2\text{-ph}}\rangle$ (resp. $|-\alpha_{2\text{-ph}}\rangle$) if

$\text{Re}(\alpha(0)) > 0$ (resp. $\text{Re}(\alpha(0)) < 0$). Additionally, although the action of \mathbf{a} operator induces bit-flip errors, phase-flip errors are heavily suppressed in presence of this pumping scheme. Indeed, as proven in [45], the phase-flip rate is exponentially suppressed with the size of the cat states $|\alpha_{2\text{-ph}}|^2$.

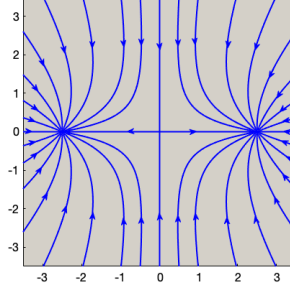


Figure 1.10: **Vector field associated to the semi-classical dynamics of Eq. (1.48) represented in the phase space of the harmonic oscillator.** The dynamics admit three equilibrium points: the two equilibrium points $\pm\alpha$ are stable and the equilibrium 0 is a saddle point.

An evolution under a master equation such as Eq. (1.48) can be achieved by considering both the harmonic oscillator mode \mathbf{a} (now called *storage* mode), with a very good quality factor and which will be the mode effectively storing information using cat states, and an extra very dissipative mode \mathbf{b} (called *readout* mode). The latter mode can be viewed as a way to evacuate entropy out of the system. Assuming an interaction Hamiltonian between these two modes of the form

$$H_{\text{int}} = \hbar g_{2\text{-ph}} \left[(\mathbf{a}^\dagger)^2 \mathbf{b} + \mathbf{a}^2 \mathbf{b}^\dagger \right] \quad (1.49)$$

while driving the \mathbf{b} mode, resulting in a Hamiltonian $H_{\text{drive}} = i\hbar u (\mathbf{b}^\dagger - \mathbf{b})$ with u the amplitude of the drive, this results in a master equation for the whole system reading

$$\frac{d\rho}{dt} = u [\mathbf{b}^\dagger - \mathbf{b}, \rho] + \kappa_b D[\mathbf{b}](\rho) - ig_{2\text{-ph}} \left[(\mathbf{a}^\dagger)^2 \mathbf{b} + \mathbf{a}^2 \mathbf{b}^\dagger \right] \quad (1.50)$$

where κ_b is the (large) dissipation rate of the readout mode. Then, using an adiabatic elimination method [41] to eliminate the strongly dissipative readout mode (with fast dynamics), one recovers a (reduced) master equation of the form of Eq. (1.48). More details about this adiabatic elimination procedure are given in section 1.4.

1.5.3 Four-photon pumping extension

The cat encoding and two-photon pumping schemes presented in sections 1.5.1 and 1.5.2 can be extended to a four-photon pumping scheme with greater protection against errors. Indeed, similarly to the cat states defined in section 1.5.1, one can define the cat states

$$\begin{aligned} |\mathcal{C}_\alpha^\pm\rangle &= \frac{1}{\sqrt{2}} (|\alpha\rangle \pm |-\alpha\rangle) \\ |\mathcal{C}_{i\alpha}^\pm\rangle &= \frac{1}{\sqrt{2}} (|i\alpha\rangle \pm |-i\alpha\rangle) \end{aligned} \quad (1.51)$$

where we assumed that α is large enough so that $|\pm\alpha\rangle$ and $|\pm i\alpha\rangle$ can all be considered orthogonal. It is important to note at this point that $\text{Span}(|\alpha\rangle, |-\alpha\rangle, |i\alpha\rangle, |-i\alpha\rangle)$ is stable under the application of the annihilation operator, which is the main source of errors in superconducting circuits.

Then, let us introduce two different qubit basis

$$\begin{aligned} |0_L^+\rangle &= |\mathcal{C}_\alpha^+\rangle & \text{and} & & |0_L^-\rangle &= |\mathcal{C}_\alpha^-\rangle \\ |1_L^+\rangle &= |\mathcal{C}_{i\alpha}^+\rangle & & & |1_L^-\rangle &= |\mathcal{C}_{i\alpha}^-\rangle \end{aligned} \quad (1.52)$$

which can be used to encode a qubit value. From the fact that $\mathbf{a}|\mathcal{C}_\alpha^\pm\rangle \approx \alpha|\mathcal{C}_\alpha^\mp\rangle$ and that $\mathbf{a}|\mathcal{C}_{i\alpha}^\pm\rangle \approx i\alpha|\mathcal{C}_{i\alpha}^\mp\rangle$, it immediately comes that the \mathbf{a} annihilation operator induces jumps between these two basis. By tracking the jumps between these sets of encoding bases, one can therefore correct the induced errors such that no information is lost. This evolution of the encoding basis under the action of the annihilation operator \mathbf{a} is illustrated in Fig. 1.11.

These change of basis can be tracked by continuously monitoring the parity operator $\mathbf{\Pi} = \exp(i\mathbf{a}^\dagger\mathbf{a})$ (with eigenvalues $+1$ for even Fock states and -1 for odd Fock states). Indeed, $|0_L^+\rangle$ and $|1_L^+\rangle$ are eigenstates of the parity operator $\mathbf{\Pi}$ associated to the eigenvalue 1 , while $|0_L^-\rangle$ and $|1_L^-\rangle$ are eigenstates of the parity operator associated to the eigenvalue -1 . The action of the annihilation operator \mathbf{a} translates into a jump of the mean value of the parity observable.

In order to overcome the deterministic energy relaxation of the underlying coherent states, a pumping scheme should be devised. [16] makes a proposal to use an interaction Hamiltonian between a storage mode \mathbf{a} and a dissipative readout mode \mathbf{b} , similar to the two-photon pumping scheme from section 1.5.2, which reads

$$H_{\text{int}} = \hbar g_{4\text{-ph}} \left[(\mathbf{a}^\dagger)^4 \mathbf{b} + \mathbf{a}^4 \mathbf{b}^\dagger \right] \quad (1.53)$$

where $g_{4\text{-ph}}$ is the four-photons interaction strength and should be as large as possible (typically of the order of a few MHz). An Hamiltonian such as Eq. (1.53) can be achieved, for instance, using a circuit analogous to the one used in section 1.5.2, based on a Josephson junction coupling two microwave cavities. Indeed, when taking into account higher order terms in the expansion of the cosine and under the frequency matching condition $\omega_p = 4\omega_a - \omega_b$, an interaction term of the form of Eq. (1.53) would emerge. This, however, comes at the expense of having many parasitic non-rotating terms and this circuit is not much of practical use.

The \mathbf{b} mode being very dissipative, it can be adiabatically eliminated (following the approach of section 1.4), and the evolution of the storage mode \mathbf{a} only is given by

$$\frac{d\rho}{dt} = \kappa_{4\text{-ph}} D \left[\mathbf{a}^4 - \alpha_{4\text{-ph}}^4 \right] (\rho) \quad (1.54)$$

where $\kappa_{4\text{ph}} = \frac{4g_{4\text{-ph}}^2}{\kappa_b}$ with κ_b the single photon dissipation rate of the readout mode \mathbf{b} and $\alpha_{4\text{-ph}} = \sqrt[4]{2\varepsilon_{4\text{-ph}}/\kappa_{4\text{-ph}}}$ with $\varepsilon_{4\text{-ph}} = 2A_p g_{4\text{-ph}}/\kappa_b$.

For practical use, one wishes that $\kappa_{4\text{-ph}} \gg \kappa_{1\text{-ph}}$ where $\kappa_{1\text{-ph}}$ denotes the rate at which single photon loss happens on the storage mode. In current experiments, $\kappa_{1\text{-ph}}$ is typically of the order of 10kHz. Noting that $\kappa_{4\text{-ph}} < g_{4\text{-ph}}$, this means that ideally $g_{4\text{-ph}}$ should be of the order of 1MHz.

1.6 Physical realization of cat-pumping interaction with a single Josephson junction

As discussed in previous section, by engineering an interaction Hamiltonian between the storage mode and an extra readout mode, one can force exchanges of photons between the two modes to be made only in pairs. Such an engineered dissipation stabilize the cat states manifold, enabling us to store the quantum information on time scales longer than the initial quantum harmonic oscillator (for instance a microwave cavity mode) lifetime. I will now focus on the simplest circuit to achieve an interaction Hamiltonian of the form of Eq. (1.49) and used in [28]. The circuit, shown in Fig. 1.12(a), consists in a microwave cavity with a high quality factor for the storage mode coupled to a very dissipative microwave cavity for the readout mode through a Josephson junction providing a non-linearity. In a first time, let us ignore the drive close to resonance on the cavity. The Hamiltonian of this system reads

$$H(t) = \hbar\omega_a \mathbf{a}^\dagger \mathbf{a} + \hbar\omega_b \mathbf{b}^\dagger \mathbf{b} - E_J \left[\cos(\varphi) + \frac{\varphi^2}{2} \right] + \hbar\mathcal{A}_p(t) (\mathbf{b}^\dagger - \mathbf{b}) \quad (1.55)$$

where $\varphi = \varphi_a^0 (\mathbf{a} + \mathbf{a}^\dagger) + \varphi_b^0 (\mathbf{b} + \mathbf{b}^\dagger)$ is the flux across the junction, ω_a is the frequency of the storage mode, ω_b is the frequency of the readout mode, $\mathcal{A}_p(t) = 2A_p \cos \omega_p t$ is the time-dependent amplitude of the strong far-detuned pump at frequency ω_p and E_J is the Josephson energy.

When $E_J = 0$, the corresponding quantum Langevin equations read

$$\begin{cases} \frac{d\mathbf{a}}{dt} = -i\omega_a \mathbf{a} \\ \frac{d\mathbf{b}}{dt} = -i\omega_b \mathbf{b} - i\mathcal{A}_p(t) \end{cases} \quad (1.56)$$

And, as $\mathcal{A}_p(t) = 2A_p \cos \omega_p t$, a solution for the \mathbf{b} mode is a coherent state of amplitude $\bar{\beta}(t)$ such that

$$\bar{\beta}(t) = A_p \left[\frac{e^{i\omega_p t}}{\omega_b + \omega_p} + \frac{e^{-i\omega_p t}}{\omega_b - \omega_p} \right] \quad (1.57)$$

Then, introducing $\tilde{\mathbf{b}} = \mathbf{b} - \bar{\beta}(t)$, the Hamiltonian of the system reads

$$H = \hbar\omega_a \mathbf{a}^\dagger \mathbf{a} + \hbar\omega_b \tilde{\mathbf{b}}^\dagger \tilde{\mathbf{b}} - E_J \left[\cos \tilde{\varphi} + \frac{\tilde{\varphi}^2}{2} \right] \quad (1.58)$$

where $\tilde{\varphi} = \varphi_a^0 (\mathbf{a} + \mathbf{a}^\dagger) + \varphi_b^0 (\tilde{\mathbf{b}} + \tilde{\mathbf{b}}^\dagger) + 2\varphi_b^0 \text{Re} \bar{\beta}(t)$.

Assuming φ is small, let us expand the cosine term and write the Hamiltonian in interaction picture with respect to the numbers operators part ($\hbar\omega_a \mathbf{a}^\dagger \mathbf{a} + \hbar\omega_b \mathbf{b}^\dagger \mathbf{b}$)

$$H(t) = -E_J \sum_{k \geq 2} \frac{(-1)^k}{k!} \left[\varphi_a^0 (\mathbf{a} e^{-i\omega_a t} + \mathbf{a}^\dagger e^{i\omega_a t}) + \varphi_b^0 (\tilde{\mathbf{b}} e^{-i\omega_b t} + \tilde{\mathbf{b}}^\dagger e^{i\omega_b t}) + 2\varphi_b^0 \text{Re} \bar{\beta}(t) \right]^{2k} \quad (1.59)$$

Using the time-averaging methods from [19] and only considering the cosine expansion up to quartic terms, the Hamiltonian reduces to

$$\bar{H}_{2\text{-ph}} = \hbar g_{2\text{-ph}} \left[\mathbf{a}^\dagger \mathbf{b}^\dagger + (\mathbf{a}^\dagger)^2 \mathbf{b} \right] + \frac{\hbar \chi_{aa}}{2} (\mathbf{a}^\dagger \mathbf{a})^2 + \frac{\hbar \chi_{aa}}{2} (\tilde{\mathbf{b}}^\dagger \tilde{\mathbf{b}})^2 + \hbar \chi_{ab} (\mathbf{a}^\dagger \mathbf{a}) (\tilde{\mathbf{b}}^\dagger \tilde{\mathbf{b}}) \quad (1.60)$$

where we introduced $\chi_{aa} = E_J |\varphi_a^0|^4 / 2\hbar$ (respectively $\chi_{bb} = E_J |\varphi_b^0|^4 / 2\hbar$) the self Kerr strengths, $\chi_{ab} = E_J |\varphi_a^0|^2 |\varphi_b^0|^2 / \hbar$ the cross Kerr strength and $g_{2\text{-ph}}$ the two-photon interaction strength, expressed in terms of the physical parameters of the system and the pump strength.

Finally, when taking into account the extra drive which is close to resonance with the readout mode, the full Hamiltonian of the system reads

$$\bar{H}_{2\text{-ph}} = \hbar g_{2\text{-ph}} \left[\mathbf{a}^2 \tilde{\mathbf{b}}^\dagger + (\mathbf{a}^\dagger)^2 \tilde{\mathbf{b}} \right] + \frac{\hbar \chi_{aa}}{2} (\mathbf{a}^\dagger \mathbf{a})^2 + \frac{\hbar \chi_{bb}}{2} (\tilde{\mathbf{b}}^\dagger \tilde{\mathbf{b}})^2 + \hbar \mathcal{A}_d(t) (\tilde{\mathbf{b}}^\dagger - \tilde{\mathbf{b}}) \quad (1.61)$$

where \mathcal{A}_d is the complex amplitude of the drive close to resonance with the readout mode.

Using this physical implementation with a single photon and using the results derived in section 1.4, the effective two-photon dissipation rate is given by $\kappa_{2\text{-ph}} = 4g_{2\text{-ph}}^2 / \kappa_b$. In the cat-states encoding scheme, the protection rate is given by $\kappa_{2\text{-ph}}$ and is increasing with $g_{2\text{-ph}}$ and therefore with the pump amplitude: one usually wishes to increase the pump power to obtain a significant protection rate.

However, as discussed in section 1.3, such an increase of the pump power is strongly limited [34]: other detrimental terms in the expansion of the cosine potential of the Josephson junction will no longer be negligible in presence of a strong pump, the system can undergo phase slips or heating.

1.7 Plan of the manuscript

In Chapter 2, I study the dynamics of a transmon circuit under strong external microwave drives. First, I will present the dynamics of a transmon circuit coupled to a harmonic oscillator and I perform some change of variables to make the simulation tractable. Then, I present the Floquet-Markov approach and its application to the case of a transmon coupled to a microwave cavity. Indeed, simulating the dynamics of such a system under strong drives is challenging, due to the sizes of the Hilbert spaces as well as due to the many time scales in the system. The Floquet-Markov approach let us consider the non-linear Hamiltonian while avoiding many approximations. In the last section of Chapter 2, using the Floquet-Markov approach, I will present the results for the ac-Stark shift, that is the renormalization of the microwave cavity frequency as a function of drive power.

In Chapter 3, I study an alternative circuit consisting of a transmon with an additional inductive shunt, coupled to a microwave cavity. Indeed, the results from Chapter 2 emphasize a decoupling behavior where the transmon non longer contribute any non-linearity to the microwave cavity mode above a given threshold pump power. As I show in Chapter 3, the additional inductive shunt makes the whole system more stable and the non-linearity can then be exploited on a larger span of pump powers. In this Chapter, I present the model as well as the results from simulations in the Floquet-Markov theory. In the last section, I compare results from the Floquet-Markov theory with results obtained from a first-order time-averaging on this system. Here, and contrary to the unshunted case, the time-averaged model can be used, giving good qualitative predictions.

In Chapter 4, I detail the way I realized the Floquet-Markov simulations and the numerical methods.

Finally, building on previous results, I investigate in Chapter 5 the properties of a circuit based on the Josephson Ring Modulator, a circuit currently used for amplification

and conversion. This slightly modified version, with some asymmetry in the Josephson ring, is considered as a more robust source of non-linearity to engineer two-photon and four-photon pumping Hamiltonian for the cat encoding scheme.

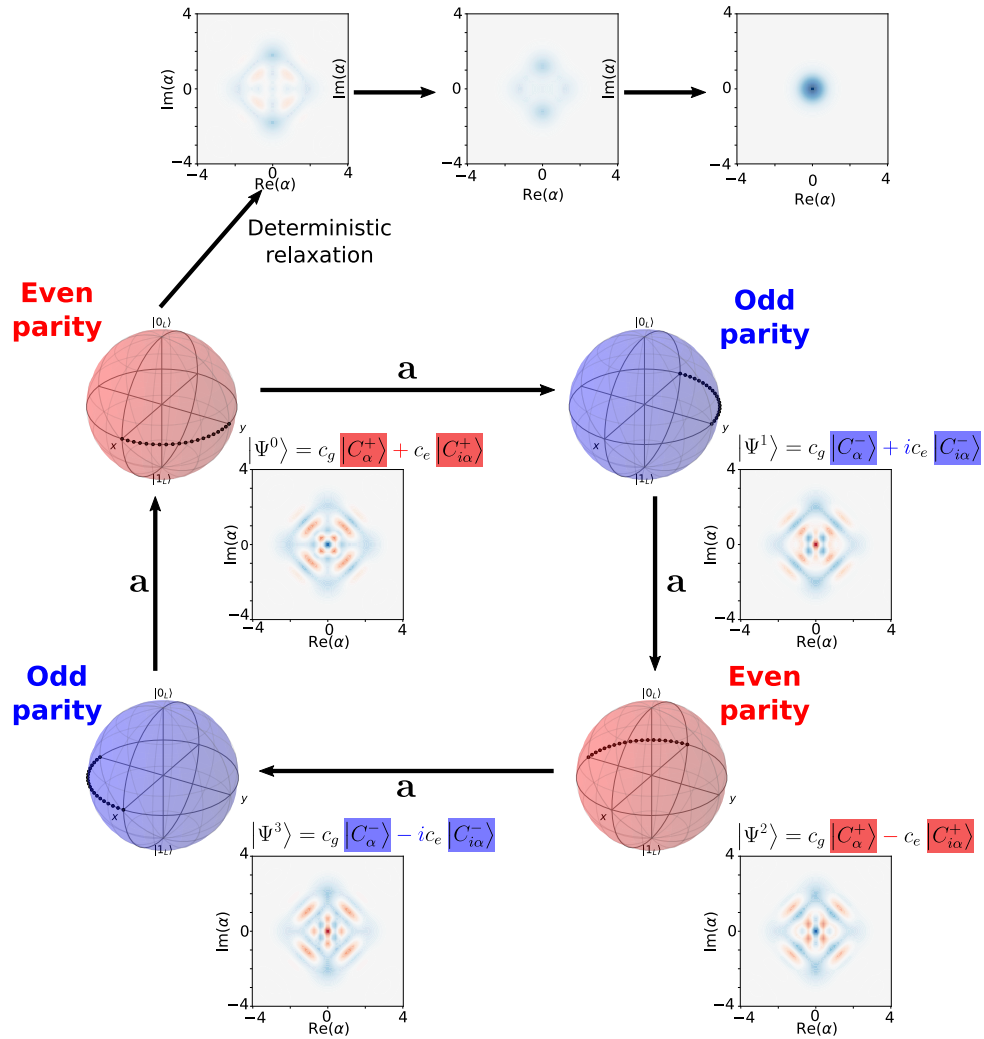


Figure 1.11: **Life and death of information encoded in the four-photon cat states encoding in a microwave cavity.** Starting from an initial qubit state $|\Psi\rangle$ encoded in the even parity subspace $\{|0_L^+\rangle, |1_L^+\rangle\}$ (top-left Bloch sphere representation), the action of the storage mode annihilation operator \mathbf{a} switches back and forth the encoding basis between even parity and odd parity states (lower ring). Bloch sphere representation in each of the encoding basis are shown as well as Wigner representation of the $|0_L^\pm\rangle$ states. The fringes in the Wigner representation indicate a coherent superposition while the parity of the states can be distinguished by looking at the sign of the center fringe. In absence of pumping, the underlying coherent states decay towards the vacuum state according to the microwave cavity lifetime, therefore losing quantum information (top line).

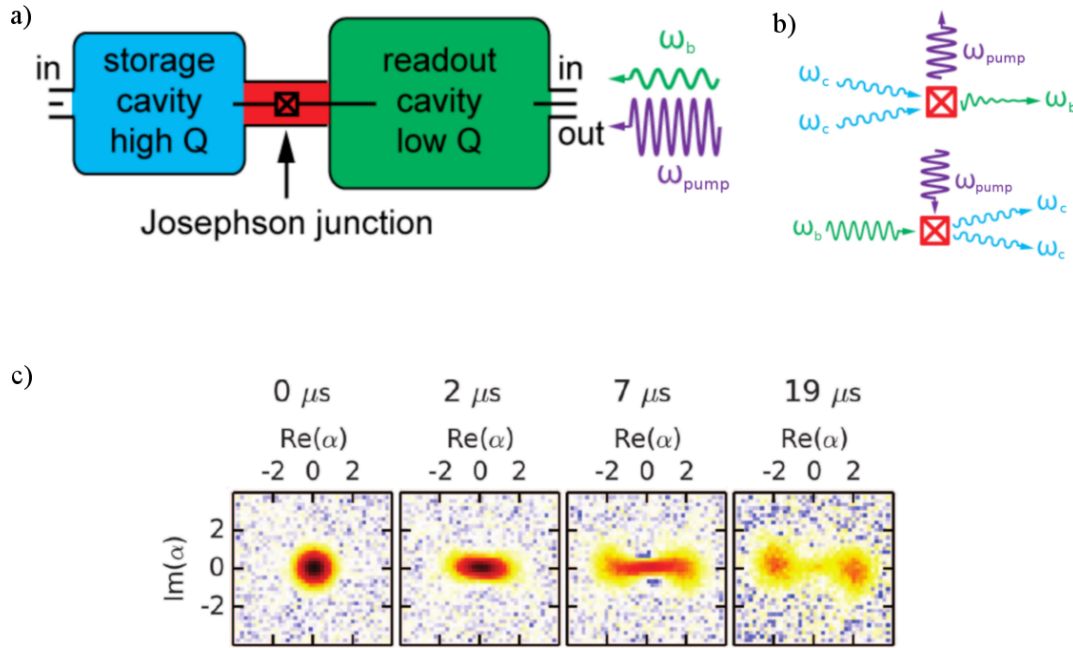


Figure 1.12: **Implementation of the two-photon pumping scheme with a Josephson junction.** a) A storage mode, used to store the quantum information with a cat-state encoding, is coupled to a fast dissipative readout mode through a non-linear element (Josephson junction). A pump, detuned from the resonant frequencies of the system, is driving the readout cavity to mediate the two-photon exchange Hamiltonian. An additional drive, in resonance with the readout cavity, is applied. b) Under the frequency matching condition, two processes are dominant: the conversion of one photon at the readout frequency and a photon from the pump into two photons at the storage frequency and the reverse process. c) Wigner tomography results from [28]. Starting from the vacuum of the storage mode and turning on the pumping, the system evolves to a cat state at $t = 7\mu\text{s}$ as evidenced by the negativity in the center. For longer time scales, it decays to a statistical mixture of two coherent states. (Figure courtesy of Z. Leghtas[28])

Chapter 2

Structural instability of driven transmon circuit

Contents

2.1	Strongly driven transmon coupled to a cavity	26
2.2	Change of frame for numerical simulations	29
2.3	Simulations in the Floquet-Markov framework for weak dissipation	31
2.3.1	Floquet-Markov framework for weak dissipation	31
2.3.2	Numerical simulations of the ac Stark shifts in absence of offset charge	34
2.3.3	Influence of the offset charge	37
2.4	Comparison with experimental data	38

Josephson junctions are ideal non-dissipative elements that realize non-linear Hamiltonians for superconducting quantum circuits. Compared to nonlinear crystals in the optical regime, Josephson circuits have a much larger ratio between multi-wave mixing and decoherence rates [46, 47, 48]. By applying off-resonant drives (pumps) verifying frequency matching conditions, one can engineer various Hamiltonians that are not obtainable statically. This so-called parametric method has been used, for instance, to achieve frequency conversion [49], quantum-limited amplification [50], two-mode squeezing [51], transverse readout of a qubit [52], and multi-photon exchanges between two modes [28]. In all these applications, the rates of the engineered parametric couplings scale with the pump power. However, as observed in [28, 34, 32], this scaling can be strongly limited by effects such as the induced deterioration of the coherence properties.

In this Chapter, I will study such limitations, focusing in particular on the ac-Stark shift effect [53, 54, 55] as an indicator of systems behavior. Indeed, when driving a non-linear oscillator, there is a shift of its resonant frequency as a function of the drive power. This is the ac-Stark shift effect which is the dominant observable effect in such quantum circuits. For small enough pump strengths, the frequency shift is expected to be linear in the pump power [53]. At higher pump strengths, higher order terms in the ac-Stark shift should be taken into account, giving a small curvature of this dependence. I am here interested in the high pumping regime, beyond these spans of pump strengths.

I explain these limitations by analyzing the structural stability of the underlying dynamical system. I call a dynamical system structurally stable if small modifications of the parameters, such as the strength of the pumping drives, lead to small changes in its qualitative behavior, such as the asymptotic steady states of the driven-dissipative system. I show that the ubiquitous system consisting of a transmon [56, 7] coupled to a cavity mode displays strong instabilities in this sense. I predict that above a critical pump power the transmon state escapes the Josephson potential confinement and is sent to free-particle-like states. The circuit behaves then as if we had removed the junction, and this explains the jump of the cavity frequency towards its bare (undressed) value. Previously, such a jump in the resonance frequency has been observed in a setup with a single strong probe drive, and used to perform single shot measurements of the transmon qubit [36]. This work however differs from previous theoretical works which have investigated this phenomenon assuming two-level [37], multi-level [57, 35, 39] and Duffing approximations [38] of the transmon mode in that the full model is taken into consideration for numerical simulations. Additionally and contrary to the approach of looking at the transmission response of the strong pump, the pump drive is only used as a pump here, while a separate small power probe drive is considered for performing spectroscopy of the system.

2.1 Strongly driven transmon coupled to a cavity

In this chapter, I am investigating the dynamics of a transmon coupled to a harmonic oscillator (later simply referred to as “oscillator”), under strong drives. The lumped elements circuit depicted in Fig. 2.1 can be quantized by following closely the methods described in [17, 14]. First, let us write its Lagrangian,

$$L = \frac{C_J}{2} \dot{\Phi}_b^2 + \frac{C_g}{2} (\dot{\Phi}_a - \dot{\Phi}_b)^2 + \frac{C_B}{2} \dot{\Phi}_a^2 - \frac{\Phi_a^2}{2L_B} + E_J \cos \left[2\pi \frac{\Phi_b}{\Phi_0} \right] \quad (2.1)$$

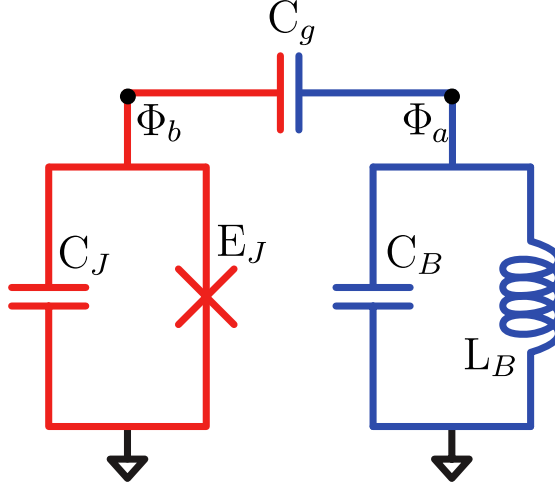


Figure 2.1: **Lumped element circuit of a transmon coupled to a harmonic oscillator (microwave cavity)**. This lumped element circuit depicts a transmon (here in red) with a capacitance C_J and a Josephson energy E_J for the junction, capacitively coupled (through a capacitance C_g) to a microwave cavity (harmonic oscillator, here in blue) with a capacitance C_B and an inductance L_B .

where $\Phi_{a,b}$ are the node flux as indicated on Fig. 2.1, $\Phi_0 = h/2e$ is the magnetic quantum flux, C_J is the capacitance associated to the junction, E_J is the Josephson junction energy, C_B and L_B are the capacitance and inductance of the microwave cavity and C_g is the coupling capacitance.

Let us introduce the conjugate variables $Q_{a,b}$ (node charge), defined as

$$\begin{cases} Q_a = \frac{\partial L}{\partial \Phi_a} = C_B \dot{\Phi}_a + C_g (\dot{\Phi}_a - \dot{\Phi}_b) \\ Q_b = \frac{\partial L}{\partial \Phi_b} = C_J \dot{\Phi}_b + C_g (\dot{\Phi}_b - \dot{\Phi}_a) \end{cases} \quad (2.2)$$

The Hamiltonian of this circuit is then given by

$$H = Q_a \dot{\Phi}_a + Q_b \dot{\Phi}_b - L \quad (2.3)$$

which can be written as

$$H = \frac{Q_a^2}{2\tilde{C}_a} + \frac{Q_b^2}{2\tilde{C}_b} + E_g Q_a Q_b + \frac{\Phi_a^2}{2\tilde{L}_a} - E_J \cos \theta \quad (2.4)$$

at the expense of introducing $\theta = 2\pi\Phi_b/\Phi_0$, renormalized capacitances \tilde{C}_a and \tilde{C}_b and a coupling energy E_g which are expressed in terms of C_B , C_J and C_g .

Quantization of the Hamiltonian Eq. (2.4) can now be done using the usual promotion of variables to operators. I will use the charge states description for the transmon operators $\cos(\theta)$ and \mathbf{Q}_b . Then,

$$\begin{cases} \mathbf{Q}_b = -2e (\mathbf{N} - N_g) \\ \cos(\theta) = \frac{1}{2} \sum_{N=-\infty}^{+\infty} |N\rangle \langle N+1| + \text{h.c.} \end{cases} \quad (2.5)$$

where e is the elementary charge, $\mathbf{N} = \sum_{N=-\infty}^{+\infty} |N\rangle \langle N|$ is the Cooper pair number operator, N_g is a continuous-valued offset charge (or “gate charge”) and $\{|N\rangle\}_{N \in \mathbb{Z}}$ is the charge states basis. The $\cos(\theta)$ operator accounts for the transfer of Cooper pairs across the junction. Let us note that here, the number of Cooper pairs \mathbf{N} takes its value in \mathbb{Z} and that the phase θ takes its values in the interval $[0, 2\pi]$ [14, 17]. Therefore, θ can only appear in operators defined by a periodic function. \mathbf{N} and θ operators satisfy the commutation relation $[\theta, \mathbf{N}] = i$.

I can quantize the cavity variables Φ_a and Q_a as a harmonic oscillator, introducing photon annihilation and creation operators of the oscillator mode, \mathbf{a} and \mathbf{a}^\dagger . Then,

$$\begin{cases} \mathbf{Q}_a = -iQ_a^{\text{ZPF}} (\mathbf{a}^\dagger - \mathbf{a}) \\ \Phi_a = \Phi_a^{\text{ZPF}} (\mathbf{a} + \mathbf{a}^\dagger) \end{cases} \quad (2.6)$$

where $Q_a^{\text{ZPF}} = \sqrt{\hbar/2Z_a}$ and $\Phi_a^{\text{ZPF}} = \sqrt{\hbar Z_a/2}$ with $Z_a = \sqrt{\tilde{L}_a/\tilde{C}_a}$ the characteristic impedance of the oscillator. Then,

$$\frac{\mathbf{Q}_a^2}{2\tilde{C}_a} + \frac{\Phi_a^2}{2\tilde{L}_a} = \hbar\omega_a \mathbf{a}^\dagger \mathbf{a} \quad (2.7)$$

where $2\pi\omega_a = 2\pi/\sqrt{\tilde{L}_a\tilde{C}_a}$ is the bare frequency of the oscillator, in absence of coupling to the transmon. Note that I discarded the vacuum energy here.

The quantized Hamiltonian of the circuit from Fig. 2.1 is then given by

$$\mathbf{H}(t) = 4E_C (\mathbf{N} - N_g)^2 - E_J \cos(\theta) + \hbar\omega_a \mathbf{a}^\dagger \mathbf{a} + i\hbar g (\mathbf{N} - N_g) (\mathbf{a}^\dagger - \mathbf{a}). \quad (2.8)$$

where $E_C = e^2/2\tilde{C}_b$ is the charging energy, ω_a is the bare frequency of the oscillator (in absence of coupling to the transmon) and E_J is the Josephson coupling energy. $g = 2eE_g Q_a^{\text{ZPF}}/\hbar$ is the coupling rate between the two modes.

Let us now focus on the circuit depicted in Fig. 2.2 where I also considered the coupling of the cavity to a transmission line. A (strong) off-resonant microwave drive at frequency ω_p is sent to the system through this transmission line. This pump can be described by its time-dependent amplitude $\mathcal{A}_p(t) = A_p \cos(\omega_p t)$, with an amplitude A_p and a frequency ω_p far detuned from the resonance frequencies of the system. Using the previous results, the Hamiltonian of the whole circuit from Fig. 2.2 can be written as

$$\mathbf{H}(t) = 4E_C (\mathbf{N} - N_g)^2 - E_J \cos(\theta) + \hbar\omega_a \mathbf{a}^\dagger \mathbf{a} + i\hbar g (\mathbf{N} - N_g) (\mathbf{a}^\dagger - \mathbf{a}) + i\hbar \mathcal{A}_p(t) (\mathbf{a}^\dagger - \mathbf{a}). \quad (2.9)$$

The dissipation is modelled as a capacitive coupling of the oscillator to a transmission line [58], the Hamiltonian of this coupling between the system and the bath being

$$\mathbf{H}_{SB} = \sum_k \left[\hbar\omega_k \mathbf{c}^\dagger[\omega_k] \mathbf{c}[\omega_k] - \hbar\Omega[\omega_k] (\mathbf{a}^\dagger - \mathbf{a}) (\mathbf{c}^\dagger[\omega_k] - \mathbf{c}[\omega_k]) \right]. \quad (2.10)$$

Here, $\mathbf{c}[\omega_k]$ and $\mathbf{c}^\dagger[\omega_k]$ are the photon annihilation and creation operators of the bath modes at frequency ω_k and $\Omega[\omega_k]$ represents their coupling strengths to the circuit oscillator mode \mathbf{a} .

From now on, I will focus on the Hamiltonian Eq. (2.9) modelling the circuit Fig. 2.2 and consider the new parameters E_C , E_J , ω_a , g and $\mathcal{A}_p(t)$ as the base parameters

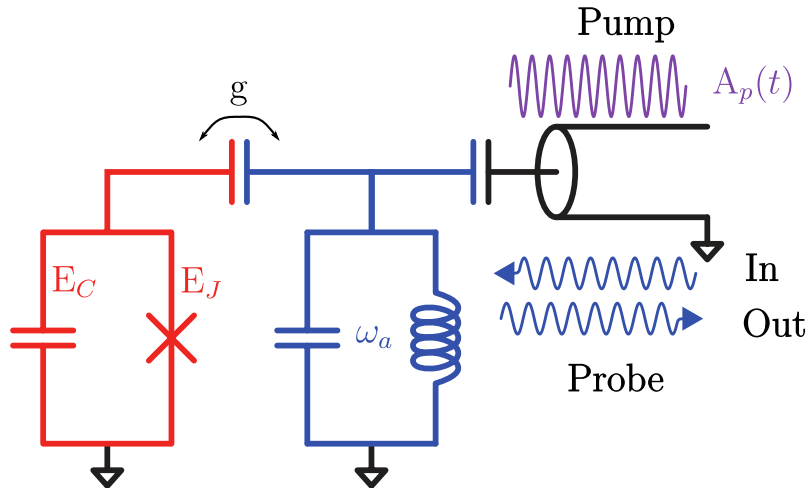


Figure 2.2: **Circuit of a regular transmon, coupled to a harmonic oscillator (microwave cavity) and capacitively coupled to a transmission line.** A (strong) off-resonant microwave drive at frequency ω_p , called a *pump*, is sent to the system through the transmission line. Experimentally, an additional weak drive, called a *probe*, is used to probe the resonant frequencies of the system. This probe drive is not considered in the model I use as a basis for the numerical simulation. Instead, its effect is simulated through the study of the structure of the steady-state dynamics, as detailed in section 2.3.1.

describing the circuit. In this chapter, I am investigating the dynamics of this system for large pump amplitudes, where the number of circulating photons, given by $\bar{n} = |A_p|^2/4|\Delta_p|^2$ (with Δ_p the detuning between the pump frequency and the dressed oscillator frequency) can reach a few hundreds.

2.2 Change of frame for numerical simulations

Non-perturbative numerical simulations of such a strongly driven nonlinear system are particularly challenging. They require the simulation of a master equation over a Hilbert space of large dimension and with times scales separated by many orders of magnitude [59]. The dimensionality issue can be overcome by changing the frame of reference, displacing the high excitation manifold into a tractable one.

First, let us write quantum Langevin equations for the time evolution under Hamiltonian Eq. (2.9). To start and in order to simplify notations, I will ignore the influence of the charge offset N_g , setting $N_g = 0$.

For the annihilation operator \mathbf{a} , this gives

$$\frac{d\mathbf{a}}{dt} = -i\omega_a \mathbf{a} + g\mathbf{N} + \mathcal{A}_p(t) \quad (2.11)$$

and for the transmon operators, this gives

$$\begin{cases} \frac{d\theta}{dt} = 8\frac{E_C}{\hbar} \mathbf{N} + ig(\mathbf{a}^\dagger - \mathbf{a}) \\ \frac{d\mathbf{N}}{dt} = -\frac{E_J}{\hbar} \sin(\theta). \end{cases} \quad (2.12)$$

Let us introduce the displaced modes $\tilde{\mathbf{a}} = \mathbf{a} - \bar{a}\mathbf{1}$, $\tilde{\mathbf{N}} = \mathbf{N} - \bar{N}\mathbf{1}$ and $\tilde{\boldsymbol{\theta}} = \boldsymbol{\theta} - \bar{\theta}\mathbf{1}$ where \bar{a} , \bar{N} and $\bar{\theta}$ are solutions of Eq. (2.11) and Eq. (2.12) with E_J set to zero¹,

$$\begin{cases} \frac{d\bar{a}}{dt} = -i\omega_a\bar{a} + g\bar{N} + \mathcal{A}_p(t) \\ \frac{d\bar{\theta}}{dt} = 8\frac{E_C}{\hbar}\bar{N} + ig(\bar{a}^* - \bar{a}) \\ \frac{d\bar{N}}{dt} = 0 \end{cases} \quad (2.13)$$

A solution of this system is

$$\begin{cases} \bar{a} = \frac{A_p}{2i} \left[\frac{e^{i\omega_p t}}{\omega_a + \omega_p} + \frac{e^{-i\omega_p t}}{\omega_a - \omega_p} \right] \\ \bar{\theta} = -\frac{2A_p g \omega_a}{\omega_p(\omega_a^2 - \omega_p^2)} \sin(\omega_p t) \quad \text{mod } 2\pi \\ \bar{N} = 0 \end{cases} \quad (2.14)$$

Then, $\tilde{\mathbf{a}}$, $\tilde{\mathbf{N}}$ and $\tilde{\boldsymbol{\theta}}$ are solutions of

$$\begin{cases} \frac{d\tilde{\mathbf{a}}}{dt} = -i\omega_a\tilde{\mathbf{a}} + g\tilde{\mathbf{N}} \\ \frac{d\tilde{\boldsymbol{\theta}}}{dt} = 8\frac{E_C}{\hbar}\tilde{\mathbf{N}} + g(\tilde{\mathbf{a}}^\dagger - \tilde{\mathbf{a}}) \\ \frac{d\tilde{\mathbf{N}}}{dt} = -\frac{E_J}{\hbar} \sin(\tilde{\boldsymbol{\theta}} + \bar{\theta}\mathbf{1}) \end{cases} \quad (2.15)$$

From this set of equations, a Hamiltonian formulation can be recovered as

$$\tilde{\mathbf{H}}(t) = \hbar\omega_a \tilde{\mathbf{a}}^\dagger \tilde{\mathbf{a}} + 4E_C \tilde{\mathbf{N}}^2 - E_J \cos[\tilde{\boldsymbol{\theta}} - \xi \sin(\omega_p t \mathbf{1})] + i\hbar g \tilde{\mathbf{N}} (\tilde{\mathbf{a}}^\dagger - \tilde{\mathbf{a}}) \quad (2.16)$$

where $\xi = \frac{2A_p g \omega_a}{\omega_p(\omega_a^2 - \omega_p^2)}$. This Hamiltonian is written in a displaced frame taking into account a coherent displacement of the cavity. In this displaced frame, the mean value of the cavity photon number is expected to be close to zero. Additionally, it takes the pump drive into account as a drive on the superconducting phase of the transmon. Therefore, the size of the cavity Hilbert space truncature to consider for high values of the number of circulating photons ($\bar{n} \simeq 1000$) should remain numerically tractable.

At this point, it is probably worth emphasizing that, although the pump term now appears inside the cosine term in Eq. (2.16), there is still a kinetic energy term $4E_C \tilde{\mathbf{N}}^2$ outside of the cosine. Then, this differs from the usual approach where one would use black box quantization techniques [61] and end up with hybridized modes $Q_k, \Phi_k = f(k, k^\dagger)$ and a single cosine term in the Hamiltonian, of the form

$$H = -E_J \cos(\varphi_a^0 (ae^{-i\omega_a t} + \text{h.c.}) + \varphi_b^0 (be^{-i\omega_b t} + \text{h.c.}) + \varepsilon_p \cos \omega_p t).$$

Additionally, in the system studied in this chapter, under a strong pump drive, the counter-rotating terms play a major role and cannot be neglected through rotating wave approximations.

¹Note that this choice of frame ($E_J = 0$) is different from the choice of [60] ($g = 0$). By choosing a frame where $E_J = 0$, we are anticipating that in the large pump limit, the system behaves as though E_J is close to 0, and therefore it is in this frame that the cavity will remain close to its ground state. This is a key point that enabled us to simulate the system at large pump powers.

2.3 Simulations in the Floquet-Markov framework for weak dissipation

Non-perturbative numerical simulations of such a strongly driven nonlinear system are particularly challenging. They require the simulation of a master equation over a Hilbert space of large dimension and with times scales separated by many orders of magnitude [59]. The change of frame described in the previous section solves the dimension problem by displacing the high excitation manifold into a tractable one correctly. However, the full numerical simulation of the dynamics of this system, in absence of any rotating-wave approximation, remains difficult.

Indeed, usually, to simplify the dynamics, one starts by removing the fastest times scales through rotating-wave approximations. However, reliable simulations in the presence of strong drives require taking into account the counter-rotating terms in the Hamiltonian, as it had previously been noted in [40, 57]. In the study I conducted, I purposely avoided any time-averaging of the driven Hamiltonian. The Floquet-Markov framework [62] provides a useful and efficient framework to conduct these simulations for a system evolving under a periodic Hamiltonian and with weak dissipation.

2.3.1 Floquet-Markov framework for weak dissipation

Hamiltonian formulation of Floquet theory

Let us consider here a system evolving under a time-periodic Hamiltonian of period $T = 2\pi/\omega_p$. Such a system can be efficiently simulated using the tools from the Floquet theory [62, Section 2]. In this subsection, I recall some of the basic elements of the Floquet theory that are required to understand the numerical simulations method.

The Schrödinger equation for such a quantum system is

$$i\hbar \frac{\partial |\Psi\rangle}{\partial t} = H(t) |\Psi(t)\rangle \quad (2.17)$$

where $|\Psi(t)\rangle$ denotes the state of the system at time t .

The Floquet theorem states that there exists solutions to Eq. (2.17), called *Floquet states*, of the form

$$|\Psi_{\tilde{\alpha}}(t)\rangle = e^{-i\varepsilon_{\tilde{\alpha}}t/\hbar} |\Phi_{\tilde{\alpha}}(t)\rangle \quad (2.18)$$

where $|\Phi_{\tilde{\alpha}}\rangle$ is called a *Floquet mode* and is T -periodic in time and $\varepsilon_{\tilde{\alpha}}$ is a real-valued energy, called a *quasi-energy*. For any Floquet mode $|\Phi_{\tilde{\alpha}}(t)\rangle$, the periodic wave function $e^{i n \omega_p t} |\Phi_{\tilde{\alpha}}(t)\rangle$ is also a Floquet mode. Therefore, the set of quasi-energies is invariant under a translation by multiples of $\hbar\omega_p$ and the index $\tilde{\alpha}$ corresponds to two indices $(\alpha, n) \in [-\hbar\omega_p/2, \hbar\omega_p/2[\times \mathbb{Z}$, with $\varepsilon_{\tilde{\alpha}} = \varepsilon_{\alpha, n} = \varepsilon_{\alpha} + n\omega_p$. Each value of n here corresponds to a Brillouin zone. From now on, I will focus on the first Brillouin zone, $(\alpha, 0)$, which I will denote by α only to simplify the notation.

A general approach for solving the Schrödinger equation Eq. (2.17) is to first identify the Floquet modes and the associated quasi-energies. These are eigenvectors of the $H(t) - i\hbar\partial/\partial t$ operator, with corresponding eigenvalues $\{\varepsilon_{\alpha}\}_{\alpha}$. Then, as the Floquet states at a given time t from a given Brillouin zone form a basis, the initial state $|\Psi(0)\rangle$ can be written as a superposition of the Floquet states of the first Brillouin zone at time $t = 0$,

$$|\Psi(0)\rangle = \sum_{\alpha} c_{\alpha} |\Psi_{\alpha}(0)\rangle = \sum_{\alpha} c_{\alpha} |\Phi_{\alpha}(0)\rangle. \quad (2.19)$$

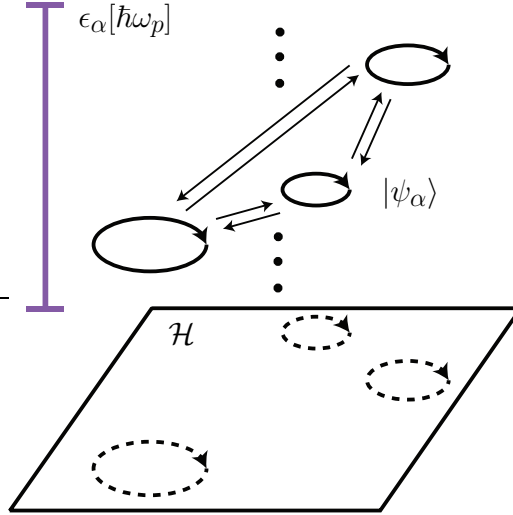


Figure 2.3: **Floquet-Markov theory.** The Floquet states $\{|\Psi_\alpha(t)\rangle\}_\alpha$ are periodic orbits of the driven system in its Hilbert space \mathcal{H} . A quasi-energy ε_α is associated with each Floquet state $|\Psi_\alpha(t)\rangle$. The set of quasi-energies is invariant under translation by multiples of $\hbar\omega_p$ (different Brillouin zones). Here, I plot the Floquet states of the first Brillouin zone (with quasi-energies defined modulo $\hbar\omega_p$ and denoted by $\varepsilon_\alpha[\hbar\omega_p]$) and their transitions due to the coupling to the bath, represented by arrow connections between them. The steady state of the driven dissipative system is given by a statistical mixture of these Floquet states, with populations inferred from an extension of the Fermi golden rule. Each Floquet state has a different projection onto the Hilbert space under consideration, \mathcal{H} , represented in dotted lines here.

The solution of Eq. (2.17) at any time $t > 0$ is then given by

$$|\Psi(t)\rangle = \sum_\alpha c_\alpha |\Psi_\alpha(t)\rangle = \sum_\alpha c_\alpha e^{-i\varepsilon_\alpha t/\hbar} |\Phi_\alpha(t)\rangle \quad (2.20)$$

In order to identify the Floquet modes and the quasi-energies, let us note that by applying the propagator $\tilde{\mathbf{U}}(t+T, t)$ of Eq. (2.17) to a Floquet solution gives

$$\tilde{\mathbf{U}}(t+T, t) |\Phi_\alpha(t)\rangle = e^{-i\varepsilon_\alpha T/\hbar} |\Phi_\alpha(T+t)\rangle \quad (2.21)$$

and in particular, at $t = 0$,

$$\tilde{\mathbf{U}}(T, 0) |\Phi_\alpha(0)\rangle = e^{-i\varepsilon_\alpha T/\hbar} |\Phi_\alpha(T)\rangle = e^{-i\varepsilon_\alpha T/\hbar} |\Phi_\alpha(0)\rangle. \quad (2.22)$$

Equation Eq. (2.22) can be used to efficiently compute numerically the Floquet modes at $t = 0$ and their quasi-energies through the eigenstates and eigenvalues of $\tilde{\mathbf{U}}(T, 0)$. Then, the value of the Floquet modes at any later time can be obtained using

$$|\Phi_\alpha(t)\rangle = e^{i\varepsilon_\alpha t/\hbar} \tilde{\mathbf{U}}(t, 0) |\Phi_\alpha(0)\rangle. \quad (2.23)$$

Floquet-Markov approach for weak dissipation

The Floquet theory can be extended to take into account weak dissipations. Under the Floquet-Markov-Born approximation [62, Section 9], one can write a master equation

in the basis of the Floquet modes of the first Brillouin zone:

$$\begin{aligned}\dot{\rho}_{\alpha\alpha}(t) &= \sum_{\nu} [L_{\alpha\nu}\rho_{\nu\nu}(t) - L_{\nu\alpha}\rho_{\alpha\alpha}(t)] \\ \dot{\rho}_{\alpha\beta}(t) &= -\frac{1}{2}\sum_{\nu} (L_{\nu\alpha} + L_{\nu\beta})\rho_{\alpha\beta}(t), \quad \alpha \neq \beta\end{aligned}\tag{2.24}$$

where $(\rho_{\alpha\beta}) = \langle \Phi_{\alpha}(t) | \rho | \Phi_{\beta}(t) \rangle$ are the components of the density matrix ρ and $L_{\alpha,\beta}$ is defined by

$$L_{\alpha\beta} = \sum_{k=-\infty}^{+\infty} (\gamma_{\alpha,\beta,k} + n_{\text{th}}(|\Delta_{\alpha,\beta,k}|) (\gamma_{\alpha,\beta,k} + \gamma_{\beta,\alpha,-k})).\tag{2.25}$$

where

$$\gamma_{\alpha,\beta,k} = 2\pi\Theta(\Delta_{\alpha\beta k}) J(\Delta_{\alpha,\beta,k}) |P_{\alpha\beta k}|^2,\tag{2.26}$$

Θ is the Heaviside distribution, $\hbar\Delta_{\alpha,\beta,k} = \epsilon_{\beta} - \epsilon_{\alpha} + k\hbar\omega_p$ is a quasi-energy difference and $J(\omega)$ is the noise spectral function of the environmental coupling. The matrix elements, $P_{\alpha\beta k}$ are given by

$$P_{\alpha\beta k} = \frac{i}{T} \int_0^T e^{-ik\omega_p t} \langle \Phi_{\alpha}(t) | (\tilde{\mathbf{a}} - \tilde{\mathbf{a}}^{\dagger}) | \Phi_{\beta}(t) \rangle dt.\tag{2.27}$$

Finally, $n_{\text{th}}(\omega) = 1/[\exp(\hbar\omega/k_B T) - 1]$ is the thermal occupation of the bath at frequency ω . In my simulations, I assume a zero temperature and therefore $n_{\text{th}} \equiv 0$.

Under some non-degeneracy assumptions (absence of resonance), the steady state of Eq. (2.24) is diagonal in the Floquet modes basis. Moreover, the diagonal of this steady state density matrix can be computed numerically in a very efficient way, by solving the linear system

$$Rp = 0,\tag{2.28}$$

where $(p_{\alpha})_{\alpha} = (\rho_{\alpha\alpha})_{\alpha}$ is the diagonal of the steady state density matrix and

$$(R_{\alpha\beta})_{\alpha\beta} = \left(L_{\alpha\beta} - \delta_{\alpha\beta} \sum_{\nu} L_{\alpha\nu} \right)_{\alpha\beta}\tag{2.29}$$

with $\delta_{\alpha\beta}$ the Kronecker delta.

Computation of the ac Stark shifts in the Floquet-Markov approach

In this subsection, I will focus on the resonance frequency of the driven system with Hamiltonian $\tilde{H}(t)$, close to the oscillator's bare frequency. Experimentally, such a resonance frequency can be found by sweeping the frequency of a very weak probe drive around the oscillator's frequency [32]. Let us model this weak probe as a small perturbative Hamiltonian $i\hbar\varepsilon(t) (\tilde{\mathbf{a}}^{\dagger} - \tilde{\mathbf{a}})$.

As shown in previous subsections, the system converges asymptotically to a limit cycle given by a statistical mixture of Floquet states:

$$\rho_{ss}(t) = \sum_{\alpha} p_{\alpha} |\Phi_{\alpha}(t)\rangle \langle \Phi_{\alpha}(t)|.$$

Initializing the system at one of the Floquet modes $|\Phi_{\alpha}\rangle$ populated in the steady state, let us focus on the solution of the Schrödinger equation in the presence of the weak

probe. Let us consider this solution at the lowest order in the amplitude of the probe field. The Schrödinger equation in this case is

$$\frac{\partial}{\partial t} |\Psi(t)\rangle = -\frac{i}{\hbar} \mathbf{H}_\varepsilon(t) |\Psi(t)\rangle, |\Psi(0)\rangle = |\Phi_\alpha(0)\rangle \quad (2.30)$$

where $\mathbf{H}_\varepsilon(t) = \tilde{\mathbf{H}}(t) + i\hbar\varepsilon(t) (\tilde{\mathbf{a}}^\dagger - \tilde{\mathbf{a}})$.

First, let us introduce the propagation operator $\tilde{\mathbf{U}}(t, 0)$ associated with the $\tilde{\mathbf{H}}(t)$ Hamiltonian,

$$\frac{\partial \tilde{\mathbf{U}}(t, 0)}{\partial t} = -\frac{i}{\hbar} \tilde{\mathbf{H}}(t) \tilde{\mathbf{U}}(t, 0), \quad \tilde{\mathbf{U}}(0, 0) = \mathbf{I}.$$

The solution of Eq. (2.30) is given by

$$\begin{aligned} |\Psi(t)\rangle &= \tilde{\mathbf{U}}(t, 0) |\Phi_\alpha(0)\rangle \\ &+ \frac{1}{\hbar} \tilde{\mathbf{U}}(t, 0) \int_0^t \varepsilon(s) \tilde{\mathbf{U}}(s, 0)^\dagger (\tilde{\mathbf{a}}^\dagger - \tilde{\mathbf{a}}) \tilde{\mathbf{U}}(s, 0) |\Phi_\alpha(0)\rangle ds \\ &= e^{-i\varepsilon_\alpha t/\hbar} |\Phi_\alpha(t)\rangle \\ &+ \frac{1}{\hbar} \tilde{\mathbf{U}}(t, 0) \int_0^t \varepsilon(s) e^{-i\varepsilon_\alpha s/\hbar} \tilde{\mathbf{U}}(s, 0)^\dagger (\tilde{\mathbf{a}}^\dagger - \tilde{\mathbf{a}}) |\Phi_\alpha(s)\rangle ds. \end{aligned}$$

Let us now focus on the overlap of $|\Psi(t)\rangle$ with other Floquet modes $|\Phi_\beta(t)\rangle$. Eq. (2.31) gives,

$$\begin{aligned} \langle \Phi_\beta(t) | \Psi(t) \rangle &= e^{-i\varepsilon_\alpha t/\hbar} \langle \Phi_\beta(t) | \Phi_\alpha(t) \rangle \\ &+ \frac{1}{\hbar} \langle \Phi_\beta(t) | \tilde{\mathbf{U}}(t, 0) \int_0^t \varepsilon(s) e^{-i\varepsilon_\alpha s/\hbar} \tilde{\mathbf{U}}(s, 0)^\dagger (\tilde{\mathbf{a}}^\dagger - \tilde{\mathbf{a}}) |\Phi_\alpha(s)\rangle ds \end{aligned} \quad (2.31)$$

that is

$$\begin{aligned} \langle \Phi_\beta(t) | \Psi(t) \rangle &= e^{-i\varepsilon_\alpha t/\hbar} \langle \Phi_\beta(t) | \Phi_\alpha(t) \rangle \\ &+ \frac{1}{\hbar} e^{-i\varepsilon_\beta t/\hbar} \int_0^t \varepsilon(s) e^{i(\varepsilon_\beta - \varepsilon_\alpha)s/\hbar} \langle \Phi_\beta(s) | (\tilde{\mathbf{a}}^\dagger - \tilde{\mathbf{a}}) |\Phi_\alpha(s)\rangle ds \\ &= e^{-i\varepsilon_\alpha t/\hbar} \langle \Phi_\beta(t) | \Phi_\alpha(t) \rangle \\ &- \frac{i}{\hbar} e^{-i\varepsilon_\beta t/\hbar} \sum_k \int_0^t \varepsilon(s) e^{i\Delta_{\alpha,\beta,k}s} P_{\beta,\alpha,k} ds \end{aligned} \quad (2.32)$$

To induce a transition in the system between the Floquet modes $|\Phi_\alpha\rangle$ and $|\Phi_\beta\rangle$, one needs the frequency of the probe drive $\varepsilon(t)$ to match one of the frequencies $\Delta_{\alpha,\beta,k}$, and furthermore that the associated matrix element $P_{\beta,\alpha,k}$ is non-zero. Moreover, the transition rate is proportional to both the population of the initial Floquet mode $|\Phi_\alpha\rangle$ in the steady state ρ_{ss} given by p_α , and the matrix element $P_{\beta,\alpha,k}$.

2.3.2 Numerical simulations of the ac Stark shifts in absence of offset charge

In order to investigate the dynamics of the system Eqs. (2.16)-(2.10) for large pump amplitude, when the circulating photons number can reach a few hundreds, I performed Floquet-Markov simulations, assuming a white-noise spectrum for the bath (therefore taking $J(\omega) = 1$ in Eq. (2.26)). In Fig. 2.4, I plot the populations of the true transmon

eigenstates $\{|\eta_k\rangle\}_{k=0}^\infty$, in $\rho_{ss}(0)$ and as a function of the pump power. The transmon eigenstates are those of the transmon Hamiltonian $4E_C\mathbf{N}^2 - E_J \cos(\theta)$.

First, the populations of the mode $\tilde{\mathbf{a}}$ remain close to the ground state over the whole range of pump values. This confirms that the actual state is well approximated by a coherent state and therefore, that the change of frame performed in section 2.2 is a correct approximation.

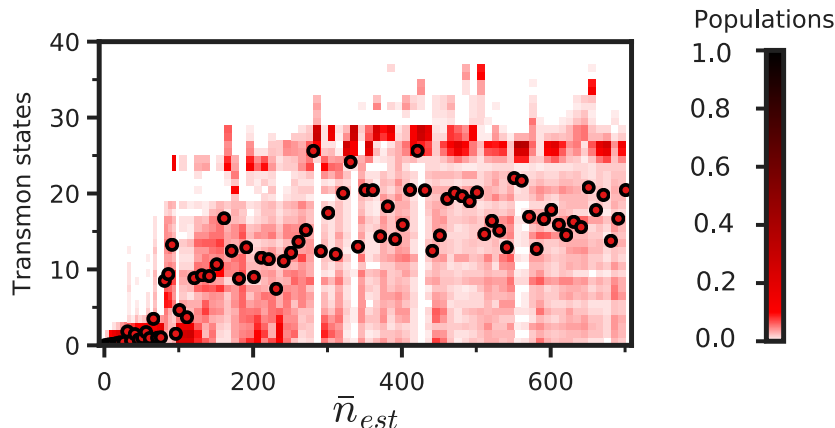


Figure 2.4: **Populations of the transmon eigenstates $\{|\eta_k\rangle\}_k$ in the steady state $\rho_{ss}(0)$ of Eqs. (2.16)-(2.10) as a function of the pump power, as computed with a Floquet-Markov approach.** The parameters are taken to be $E_C/\hbar = 150$ MHz, $E_J/\hbar = 20$ GHz, $g/2\pi = 140$ MHz, $\omega_a/2\pi = 5.5$ GHz and $\omega_p/2\pi = 6$ GHz. Here, $\bar{n}_{\text{est}} = |A_p|^2 / 4 |\omega_p - \omega_a|^2$ is an estimation of the number of circulating photons \bar{n} , where I use the bare oscillator frequency instead of the dressed one. The red dots indicate the average number of excitations in the transmon mode.

With this given set of parameters, the dynamics of the displaced transmon mode exhibit two regimes, as shown on Fig. 2.4. For $\bar{n} \lesssim 100$, the state remains well confined on the lowest transmon eigenstates, lying inside the cosine potential confinement, except for a few pump values. For $\bar{n} \gtrsim 100$, the transmon mode gets highly populated, beyond the cosine confinement. Indeed, the number of confined states in a transmon is roughly given by the ratio between the depth of the cosine potential ($2E_J$) and the level spacings (approximately $\sqrt{8E_J E_C}$) [56]. With the parameters used in Fig.2.4, there are about eight such confined levels.

Additionally, the whole tensor state remains pure for $\bar{n} \lesssim 100$, except for a few pump values, whereas for $\bar{n} \gtrsim 100$, it rapidly turns into a mixed state of a high number of excitations, as shown on Fig. 2.5 (impurity is plotted as black crosses, right axis).

Then, inspired by the experiments on the ac Stark shifts [53, 54], I simulated an excitation spectroscopy of such a driven system near the oscillator bare frequency. Each Floquet state $|\Psi_\alpha(t)\rangle$ with a nonzero population in the steady state $\rho_{ss}(t)$ can be excited to other Floquet states $|\Psi_\beta(t)\rangle$ by a weak probe drive at the frequency given by the difference of their quasi-energies $(\varepsilon_\beta - \varepsilon_\alpha)/\hbar$ [57, 63, 60]. In Fig. 2.5, I plot all these resonance frequencies as a function of the pump power.

For each pump power, a few resonance frequencies may appear, corresponding to various transitions and various Floquet states populated in the limit cycle. For weak drives, that is for $\bar{n} \ll 100$, the shift is linear in the number of photons, which is in agreement with the usual ac Stark shifts experiments [53, 54] and the associated theoretical work [55]. The behavior remains smooth up to $\bar{n} \simeq 100$, with a slight curvature

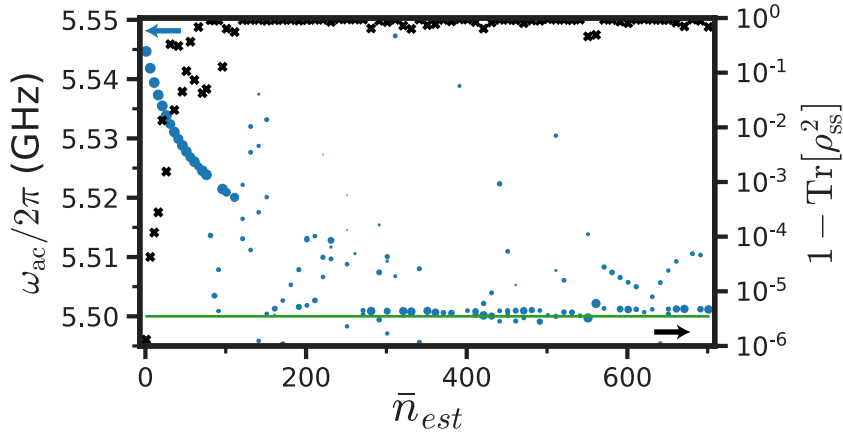


Figure 2.5: **Impurity of the steady state $\rho_{ss}(0)$ and ac Stark shifted frequencies of the oscillator as a function of the pump power.** The black crosses (right-hand axis) correspond to the impurity of the whole (tensor) steady state. The steady state quickly becomes very mixed, even for small pump strengths. The blue dots (left-hand axis) correspond to the ac Stark shifted frequencies of the oscillator as a function of the pump power. The areas of the points are proportional to the associated transition probabilities (see section 2.3.1). The green horizontal line corresponds to the oscillator bare frequency ω_a . At many pump powers, multiple resonance frequencies appear, corresponding to different transitions from the limit cycle to Floquet states. The abscissa is the same as in Fig. 2.4, using an estimation of the number of circulating photons, \bar{n}_{est} . Parameters are the same as in Fig. 2.4.

representing the effect of higher-order nonlinearities [64]. For $\bar{n} \gtrsim 300$, the dominant resonance frequency shifts close to the oscillator bare frequency. This can be physically understood by the fact that high-energy transmon states (with an energy above $2E_J$) are not affected by the cosine potential. Therefore, they are well approximated by charge states. Upon reaching these levels, the transmon mode acts as a free particle (similar to the ionization of an atom) and its dynamic follows that of the oscillator. The oscillator no longer inherits a nonlinearity from the transmon mode, as evidenced by the jump of its resonance frequency towards the bare frequency ω_a .

These two regimes slightly overlap in the middle region ($100 \lesssim \bar{n} \lesssim 300$), which presents many transition frequencies.

Previously, such a jump in the resonance frequency has been observed in a setup with a single strong probe drive and used to perform single-shot measurements of the transmon qubit [36]. Various theoretical works have investigated this phenomenon, assuming two-level [37], multilevel [57, 35, 39] and Duffing approximations [38] of the transmon mode. In contrast to these approaches, the above numerical simulations of the full model given in Eq. (2.16) and Eq. (2.10) and the experimental observations detailed in section 2.4 illustrate that such a jump in the resonance frequency coincides with the excitation of the transmon mode to high energy levels, well beyond the confinement potential.

More details about the numerical methods, the code used and the physical infrastructure used to conduct these simulations are provided in chapter 4.

2.3.3 Influence of the offset charge

In this section, I will focus on the study of the effect of charge offset N_g on the dynamics of the system. In all the simulations discussed so far in this chapter, N_g was set to zero.

Taking into account the charge offset N_g , the full Hamiltonian Eq. (2.9) of the system is

$$\mathbf{H}(t) = 4E_C (\mathbf{N} - N_g)^2 - E_J \cos(\boldsymbol{\theta}) + \hbar\omega_a \mathbf{a}^\dagger \mathbf{a} + i\hbar g (\mathbf{N} - N_g) (\mathbf{a}^\dagger - \mathbf{a}) + i\hbar \mathcal{A}_p(t) (\mathbf{a}^\dagger - \mathbf{a}). \quad (2.33)$$

where N_g is real valued. The same analysis as performed in section 2.2 can then be done, taking into account N_g and leading to the Hamiltonian Eq. (2.34) in the displaced frame

$$\widetilde{\mathbf{H}}(t) = \hbar\omega_a \widetilde{\mathbf{a}}^\dagger \widetilde{\mathbf{a}} + 4E_C (\widetilde{\mathbf{N}} - N_g)^2 - E_J \cos[\widetilde{\boldsymbol{\theta}} - \xi \sin(\omega_p t \mathbb{1})] + i\hbar g (\widetilde{\mathbf{N}} - N_g) (\widetilde{\mathbf{a}}^\dagger - \widetilde{\mathbf{a}}) \quad (2.34)$$

where $\xi = \frac{2A_p g \omega_a}{\omega_p (\omega_a^2 - \omega_p^2)}$.

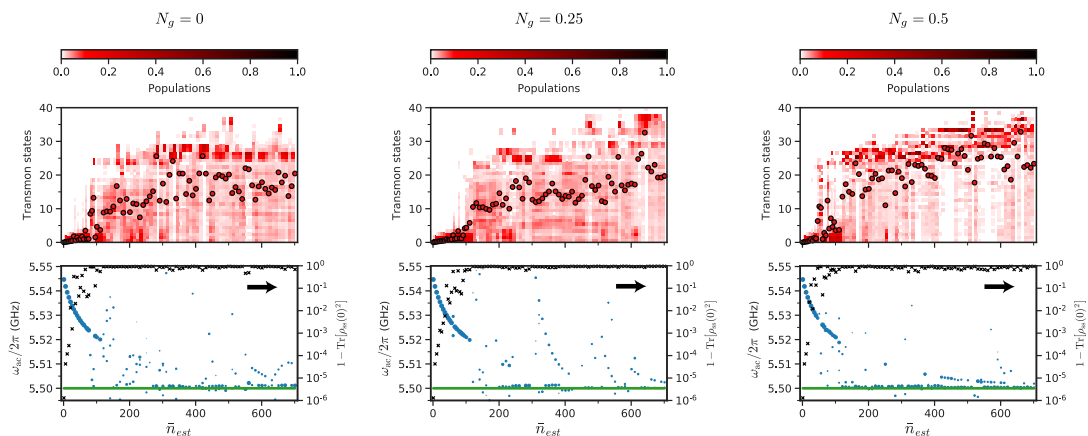


Figure 2.6: **Floquet-Markov simulations (in the asymptotic regime) of Eqs. (2.34)-(2.10), using the same parameters as in Fig. 2.4 and three different values of N_g .** In the upper figures, I plot the populations of the transmon eigenstates in the steady state $\rho_{ss}(0)$ as a function of the pump power. The red dots indicate the average number of excitations in the transmon mode. In the lower figures, I plot the ac Stark shifted frequencies of the oscillator (blue dots, left-hand axis) and the impurity of the whole steady state (black crosses, right-hand axis) as a function of the pump power. The abscissa is the same as in Fig. 2.4, using an estimation of the number of circulating photons, \bar{n}_{est} . No significant qualitative difference can be observed between the three cases. In all three cases, the steady state rapidly becomes very mixed and highly excited in the transmon eigenstates basis. Although the frequency is well defined and smooth up to $\bar{n}_{est} \simeq 100$, it is no longer well defined for larger values of \bar{n}_{est} .

As can be seen in Fig. 2.6, the value of the charge offset N_g does not yield any significant effect on the qualitative behavior of the system in the steady state.

2.4 Comparison with experimental data

In parallel to the theoretical work described in previous section, an experimental investigation of the behavior of a single transmon embedded in a 3D copper cavity was conducted at Laboratoire Pierre Aigrain [32]. Such a circuit is well modeled by the Hamiltonian depicted in Eq. (2.4). The operating regime has comparable parameters of the system, that is $E_C/\hbar = 2\pi \times 166$ MHz (versus 150 MHz in simulations), $E_J/\hbar = 2\pi \times 23.3$ GHz (versus 20 GHz in simulations), $g/2\pi = 179$ MHz (versus 140 MHz in simulations). The main difference lies in the cavity frequency under consideration, $\omega_a/2\pi = 7.739$ GHz (versus 5.5 GHz in simulations).

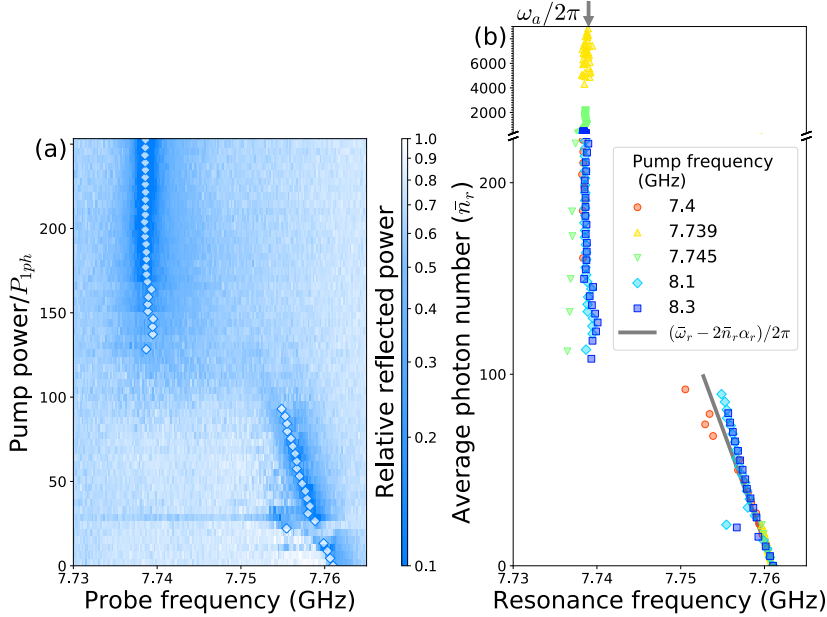


Figure 2.7: **Effect of the pump on the cavity resonance frequency.** (a) Relative reflected power of a weak probe as a function of probe frequency (x-axis), and pump power (y-axis) in units of P_{1ph} , the power needed to populate the cavity with one photon in average. The pump frequency is fixed at 8.1 GHz, about 300 MHz above the cavity frequency. The reduced reflected power is due to internal losses when the probe is resonant with the cavity. We indicate the fitted cavity resonance $\omega_r/2\pi$ with white diamonds. As the pump power increases, two regimes are distinguishable. For small powers, ω_r shifts linearly with the pump power. Above a critical power, the cavity resonance jumps to a new frequency $\omega_a/2\pi = 7.739$ GHz which is independent of pump power. (b) Fitted cavity resonance as a function of pump power for various pump frequencies. Pump powers are converted into a mean number of photons \bar{n}_r . The y-axis of (a) and (b) slightly differ because \bar{n}_r takes into account the resonator frequency shift. The general behavior is the same for all pump frequencies. The low power linear dependence is well reproduced by the AC Stark shift for an independently measured Kerr α_r (solid gray line). These two panels should be compared with theoretical results from Fig. 2.5.

They perform a spectroscopy measurement of the resonator while the pump is applied, shown on Fig. 2.7. In the regime of small pump power, they see a linear shift of the resonator frequency, while for a critical value of about a hundred photons for the most detuned frequencies, the resonator frequency abruptly jumps towards a new frequency

very close to $\omega_a/2\pi$ and independent of the pump frequency and power. This behavior is very similar to the one noticed in numerical simulations and in good qualitative agreement with the results shown on Fig. 2.5.

Additionally, in the experimental study, we measured the transmon coherence time T_1 after a time delay large enough to ensure all modes have decayed back to their ground state. Such a measure let us discriminate the possible generation of quasiparticles by the pump pulse. We find that the T_1 value is unaffected, therefore confirming that no measurable amount of quasiparticles have been generated. This is a confirmation that the model used in previous sections, which does not include quasiparticles generation, is relevant.

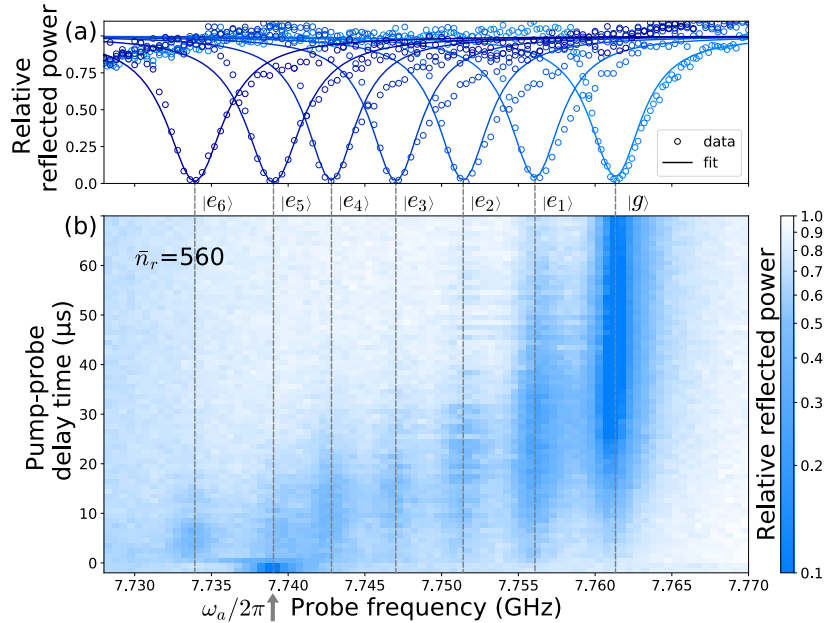


Figure 2.8: **Probing the transmon decay out of highly excited states populated by a strong off-resonant pump.** (a) Cavity spectroscopy after the transmon is prepared in various eigenstates. Each transmon state $|e_k\rangle$ ($k = 1$ to 6) is prepared using a k -photon π -pulse and higher states could not be prepared due to charge noise. (b) Time resolved measurement: first, a pump is applied for $50 \mu\text{s}$ at 8.1 GHz populating the cavity with a sufficiently large photon number to induce a jump in ω_r , here $\bar{n}_r = 560$. After a time-delay t , a weak probe is applied for $2 \mu\text{s}$. We plot the relative reflected power of the probe as a function of probe frequency (x-axis), and time-delay t (y-axis). For $t < 0$, as in Fig. 2.7, the cavity is probed while the pump is on, and the resonance frequency is $\omega_a/2\pi$, confirming that the system has jumped. At $t > 0$, the photons in the cavity rapidly decay at a rate $\kappa_r = 1/(55 \text{ ns})$, and the cavity can now be used, as in panel (a), to read the transmon state. The transmon is found in a highly excited state, and after $t = 60 \mu\text{s}$, it has fully decayed into its ground state which is compatible with $T_1 = 14 \mu\text{s}$.

Finally, the spectroscopy setup let us discriminate the seven first excitation levels of the transmon (with the parameters in use, we have about eight confined levels) in the Josephson cosine potential (results are shown in Fig. 2.8). Measuring the transmon state immediately after turning off a large pump drive (whose power corresponds to about 550 photons at the most detuned frequencies), they find the transmon to be in a highly excited state, rapidly climbing down the ladder and decaying back to the ground

state. This tends to confirm our explanation for the decoupling between the transmon and the oscillator mode after a critical pump power by the fact that the transmon state escapes out of the cosine potential. This escape of the transmon state strongly limits the exploitable range of pump powers and therefore the achievable interaction strengths with a parametric pumping scheme built around a transmon device. This escape might however be prevented by further confining the state of the circuit, imposing a broader confining potential (such as a harmonic confinement) on top of the non-linear cosine potential provided by the Josephson junction.

Chapter 3

Inductively shunted transmon: a solution to dynamical instability

Contents

3.1	Model of the driven shunted transmon circuit	42
3.2	Simulations in the Floquet-Markov framework for weak dissipation	46
3.3	Rotating-wave approximation results and comparison with numerical simulations	47
3.4	Choice of parameters for the shunted transmon circuit	49

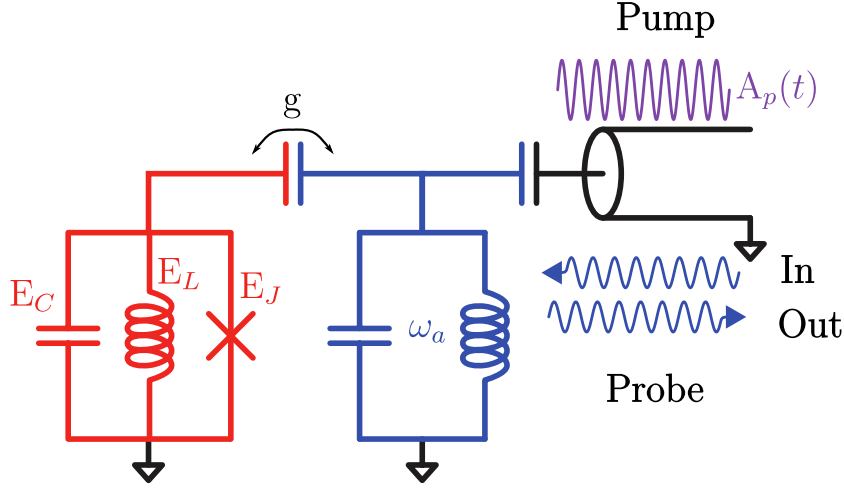


Figure 3.1: **Circuit of a transmon, shunted with an inductance and coupled to a harmonic oscillator (microwave cavity) and capacitively coupled to a transmission line.** A (strong) *pump* at frequency ω_p is sent to the system through the transmission line, similarly to the setup presented in Fig. 2.2. The extra inductance in the transmon mode should provide an extra harmonic confinement and therefore allow for a larger span of exploitable pump strengths.

The previous analysis from Chapter 2 illustrates that in the parametric construction of a non-linear Hamiltonian (such as the two-photon exchange between two modes which is used for the cat pumping scheme), the span of exploitable pump strengths is very limited. Indeed, above a critical threshold, the transmon ionizes. States of the transmon mode become excited well above the confinement provided by the cosine potential of the Josephson junction. The transmon therefore no longer contributes any non-linearity to the oscillator mode. Such a limitation has been observed through the heating of the transmon mode in [34] for instance. Further confinement of the non-linear mode should enhance the span of exploitable pump strengths. In this Chapter, I propose to shunt the transmon circuit with an inductance, providing an extra harmonic confinement of the phase across the junction [65, 66, 67], which should prevent the escape of the transmon state from its cosine confinement potential. I will first describe the model of this shunted circuit and then perform Floquet-Markov simulations to compute the ac-Stark shift effect as a function of pump strength, in comparison with the unshunted case. Finally, a first order time-averaged Hamiltonian can be derived from this system, showing a qualitative agreement with the full dynamics.

3.1 Model of the driven shunted transmon circuit

Following the approach developed in section 2.1, the Hamiltonian of the shunted transmon system, as presented in Fig. 3.1, reads

$$\mathbf{H}_{\text{shunt}}(t) = \hbar\omega_a \mathbf{a}^\dagger \mathbf{a} + 4E_C \mathbf{N}^2 + \frac{E_L}{2} \varphi^2 - E_J \cos(\varphi) + i\hbar g \mathbf{N} (\mathbf{a}^\dagger - \mathbf{a}) + i\hbar \mathcal{A}_p(t) (\mathbf{a}^\dagger - \mathbf{a}), \quad (3.1)$$

where \mathbf{a} and \mathbf{a}^\dagger are photon annihilation and creation operators of the cavity mode, ω_a is the bare cavity frequency (in absence of coupling to the transmon mode). E_C is the transmon charging energy and E_J is the Josephson energy of the junction. g is the

coupling rate between the two modes. Similarly to the case depicted in chapter 2, the pump is described by $\mathcal{A}_p(t) = A_p \cos(\omega_p t)$, with an amplitude A_p and a frequency ω_p far detuned from the resonance frequencies of the system. However, contrary to the pure transmon case depicted in chapter 2 and due to the presence of the extra inductance which removes the superconducting island, the φ operator is no longer defined on a compact interval. Both the charge operator \mathbf{N} and the phase operator φ now take real values in \mathbb{R} .

The dissipation is still modelled as a capacitive coupling of the oscillator to a transmission line [58], the Hamiltonian of this coupling between the system and the bath being

$$\mathbf{H}_{SB} = \sum_k \left[\hbar\omega_k \mathbf{c}^\dagger[\omega_k] \mathbf{c}[\omega_k] - \hbar\Omega[\omega_k] (\mathbf{a}^\dagger - \mathbf{a}) (\mathbf{c}^\dagger[\omega_k] - \mathbf{c}[\omega_k]) \right] \quad (3.2)$$

where, $\mathbf{c}[\omega_k]$ and $\mathbf{c}^\dagger[\omega_k]$ are the photon annihilation and creation operators of the bath modes at frequency ω_k and $\Omega[\omega_k]$ represents their coupling strengths to the circuit oscillator mode \mathbf{a} .

At large numbers of excitations, the harmonic potential of the Hamiltonian Eq. (3.1) $E_L/2\varphi^2$ is expected to dominate the nonlinear part $E_J \cos \varphi$, still resulting in a loss of nonlinearity in the high pumping regime. However, this passage is expected to be smoother in the shunted transmon case.

Inductively shunted Josephson junctions have previously been considered as superconducting qubit designs [68, 69]. Here, I am considering parameters comparable to a flux qubit, $E_C \ll E_J \lesssim E_L$. However, I am only considering such a circuit for using it as a nonlinear device in the strong pumping regime, in order to realize nonlinear Hamiltonians in a parametric way. Therefore, I will focus on its dynamic behavior and not on its coherence properties.

Similarly to the regular transmon case presented in chapter 2, we can apply a unitary transformation on Hamiltonian Eq. (3.1) to account for the main displacement of the modes under a strong pump.

Let us introduce $\mathbf{X}_\mathbf{a}^{(0)}$ and $\mathbf{P}_\mathbf{a}^{(0)}$ defined as

$$\begin{aligned} \mathbf{X}_\mathbf{a}^{(0)} &= i \frac{\mathbf{a}^\dagger - \mathbf{a}}{\sqrt{2}} \\ \mathbf{P}_\mathbf{a}^{(0)} &= \frac{\mathbf{a} + \mathbf{a}^\dagger}{\sqrt{2}} \\ \mathbf{N}^{(0)} &= \sqrt{\hbar\omega_a/E_L} \mathbf{N} \\ \varphi^{(0)} &= \varphi / \sqrt{\hbar\omega_a/E_L} \end{aligned} \quad (3.3)$$

Then, the Hamiltonian from Eq. (3.1) reads

$$\begin{aligned} \mathbf{H}_{\text{shunt}}(t) &= \frac{\hbar\omega_a}{2} (\mathbf{X}_\mathbf{a}^{(0)2} + \mathbf{P}_\mathbf{a}^{(0)2}) + 4 \frac{E_C E_L}{\hbar\omega_a} \mathbf{N}^{(0)2} + \frac{\hbar\omega_a}{2} \varphi^{(0)2} \\ &\quad - E_J \cos \left(\sqrt{\frac{\hbar\omega_a}{E_L}} \varphi^{(0)} \right) + \hbar\sqrt{2}g \sqrt{\frac{E_L}{\hbar\omega_a}} \mathbf{N}^{(0)} \mathbf{X}_\mathbf{a}^{(0)} + \hbar\mathcal{A}_p(t) \sqrt{2} \mathbf{X}_\mathbf{a}^{(0)}. \end{aligned} \quad (3.4)$$

Let us define $\mathbf{X}_a^{(1)}$, $\mathbf{P}_a^{(1)}$, $\mathbf{N}^{(1)}$, $\varphi^{(1)}$ as

$$\begin{cases} \mathbf{X}_a^{(0)} = \cos \theta \mathbf{X}_a^{(1)} + \sin \theta \mathbf{N}^{(1)} \\ \mathbf{N}^{(0)} = \cos \theta \mathbf{N}^{(1)} - \sin \theta \mathbf{X}_a^{(1)} \\ \mathbf{P}_a^{(0)} = \cos \theta \mathbf{P}_a^{(1)} + \sin \theta \varphi^{(1)} \\ \varphi^{(0)} = \cos \theta \varphi^{(1)} - \sin \theta \mathbf{P}_a^{(1)} \end{cases} \quad (3.5)$$

then, under the condition

$$\frac{\hbar\omega_a}{2} \sin 2\theta - \frac{4E_C E_L}{\hbar\omega_a} \sin 2\theta + \hbar g \sqrt{\frac{2E_L}{\hbar\omega_a}} \cos 2\theta = 0 \Leftrightarrow \theta = -\frac{1}{2} \tan^{-1} \left(\frac{2\hbar g \sqrt{2E_L \hbar\omega_a}}{(\hbar\omega_a)^2 - 8E_C E_L} \right), \quad (3.6)$$

the Hamiltonian Eq. (3.4) becomes

$$\begin{aligned} \mathbf{H}_{\text{shunt}}(t) &= \frac{\hbar\omega_1}{2} \mathbf{X}_a^{(1)2} + \frac{\hbar\omega_2}{2} \mathbf{N}^{(1)2} \\ &+ \frac{\hbar\omega_a}{2} \mathbf{P}_a^{(1)2} + \frac{\hbar\omega_a}{2} \varphi^{(1)2} - E_J \cos \left(\sqrt{\frac{\hbar\omega_a}{E_L}} \cos \theta \varphi^{(1)} - \sqrt{\frac{\hbar\omega_a}{E_L}} \sin \theta \mathbf{P}_a^{(1)} \right) \\ &+ \hbar \mathcal{A}_p(t) \sqrt{2} \left(\cos \theta \mathbf{X}_a^{(1)} + \sin \theta \mathbf{N}^{(1)} \right) \end{aligned} \quad (3.7)$$

where we have defined

$$\begin{aligned} \omega_1 &= \omega_a \cos^2 \theta + 8 \frac{E_C E_L}{\hbar^2 \omega_a} \sin^2 \theta - g \sqrt{\frac{2E_L}{\hbar\omega_a}} \sin 2\theta \\ \omega_2 &= \omega_a \cos^2 \theta + 8 \frac{E_C E_L}{\hbar^2 \omega_a} \sin^2 \theta + g \sqrt{\frac{2E_L}{\hbar\omega_a}} \sin 2\theta \end{aligned} \quad (3.8)$$

We can diagonalize the quadratic part of Hamiltonian Eq. (3.7), introducing operators $\mathbf{X}_a^{(2)}$, $\mathbf{P}_a^{(2)}$, $\mathbf{N}^{(2)}$, $\varphi^{(2)}$ and ending up with

$$\begin{aligned} \mathbf{H}_{\text{shunt}}(t) &= \frac{\hbar\tilde{\omega}_a}{2} \left[\mathbf{X}_a^{(2)2} + \mathbf{P}_a^{(2)2} \right] + \frac{\hbar\tilde{\omega}_b}{2} \left[\mathbf{N}^{(2)2} + \varphi^{(2)2} \right] \\ &- E_J \cos \left(r_a \sqrt{\frac{\hbar\omega_a}{E_L}} \cos \theta \varphi^{(2)} - r_b \sqrt{\frac{\hbar\omega_a}{E_L}} \sin \theta \mathbf{P}_a^{(2)} \right) \\ &+ \hbar \mathcal{A}_p(t) \sqrt{2} \left(r_a \cos \theta \mathbf{X}_a^{(2)} + r_b \sin \theta \mathbf{N}^{(2)} \right) \end{aligned} \quad (3.9)$$

where $\tilde{\omega}_a = \sqrt{\omega_a \omega_1}$, $\tilde{\omega}_b = \sqrt{\omega_a \omega_2}$, $r_a = \sqrt[4]{\omega_1 / \omega_a}$ and $r_b = \sqrt[4]{\omega_2 / \omega_a}$.

The pump drive initially applied on the cavity mode only is now being applied on both modes, $(\mathbf{X}_a^{(2)}, \mathbf{P}_a^{(2)})$ and $(\mathbf{N}^{(2)}, \varphi^{(2)})$. We can now account for the coherent displacement of these modes, due to the pump, by displacing $(\mathbf{X}_a^{(2)}, \mathbf{P}_a^{(2)})$ by a coherent state $\alpha(t)$ and $(\mathbf{N}^{(2)}, \varphi^{(2)})$ by a coherent state $\beta(t)$. As φ and \mathbf{N} take values in \mathbb{R} and verify the commutation relation $[\varphi, \mathbf{N}] = i$ and the initial $\mathbf{X}_a^{(0)}$ and $\mathbf{P}_a^{(0)}$ are a quantum harmonic oscillator mode, we can define new photon annihilation and creation

operators $(\tilde{\mathbf{a}}, \tilde{\mathbf{a}}^\dagger)$ and $(\tilde{\mathbf{b}}, \tilde{\mathbf{b}}^\dagger)$ for the displaced modes $(\mathbf{X}_a^{(2)}, \mathbf{P}_a^{(2)})$ and $(\mathbf{N}^{(2)}, \boldsymbol{\varphi}^{(2)})$. Then, let us write quantum Langevin equations for these operators

$$\begin{aligned} \frac{d\tilde{\mathbf{a}}}{dt} &= -i\tilde{\omega}_a\tilde{\mathbf{a}} - \frac{E_J}{\hbar}r_b\sqrt{\frac{\hbar\omega_a}{E_L}}\sin\theta\sin\left(r_a\sqrt{\frac{\hbar\omega_a}{E_L}}\cos\theta\boldsymbol{\varphi}^{(2)} - r_b\sqrt{\frac{\hbar\omega_a}{E_L}}\sin\theta\mathbf{P}_a^{(2)}\right) \\ &\quad + iA_p\sqrt{2}r_a\cos\theta\cos(\omega_pt) \\ \frac{d\tilde{\mathbf{b}}}{dt} &= -i\tilde{\omega}_b\tilde{\mathbf{b}} - i\frac{E_J}{\hbar}r_a\sqrt{\frac{\hbar\omega_a}{E_L}}\cos\theta\sin\left(r_a\sqrt{\frac{\hbar\omega_a}{E_L}}\cos\theta\boldsymbol{\varphi}^{(2)} - r_b\sqrt{\frac{\hbar\omega_a}{E_L}}\sin\theta\mathbf{P}_a^{(2)}\right) \\ &\quad + A_p\sqrt{2}r_b\sin\theta\cos(\omega_pt) \end{aligned} \quad (3.10)$$

We can now look for $\alpha(t)$ and $\beta(t)$ in the form

$$\alpha(t) = R_\alpha \cos(\omega_pt) + S_\alpha \sin(\omega_pt) \quad (3.11)$$

$$\beta(t) = R_\beta \cos(\omega_pt) + S_\beta \sin(\omega_pt)$$

Cancelling out the terms oscillating at frequency ω_p , we finally get

$$\begin{aligned} \alpha(t) &= \frac{A_p \cos\theta\sqrt{2}r_a}{\omega_p^2 - \tilde{\omega}_a^2} (-i\omega_p \sin(\omega_pt) + \tilde{\omega}_a \cos(\omega_pt)) \\ \beta(t) &= \frac{A_p \sin\theta\sqrt{2}r_b}{\omega_p^2 - \tilde{\omega}_b^2} (\omega_p \sin(\omega_pt) + i\tilde{\omega}_b \cos(\omega_pt)). \end{aligned} \quad (3.12)$$

Finally, under these unitary transformations, the Hamiltonian becomes

$$\begin{aligned} \tilde{\mathbf{H}}_{\text{shunt}}(t) &= \hbar\tilde{\omega}_a\tilde{\mathbf{a}}^\dagger\tilde{\mathbf{a}} + \hbar\tilde{\omega}_b\tilde{\mathbf{b}}^\dagger\tilde{\mathbf{b}} \\ &\quad - E_J \cos\left[\phi_a(\tilde{\mathbf{a}} + \tilde{\mathbf{a}}^\dagger) + \phi_b(\tilde{\mathbf{b}} + \tilde{\mathbf{b}}^\dagger) + \xi \sin(\omega_pt)\right] \end{aligned} \quad (3.13)$$

where $\tilde{\omega}_a$ and $\tilde{\omega}_b$ are renormalized frequencies (see Eq. (3.9)),

$$\begin{aligned} \phi_a &= -\sin\theta\sqrt{\frac{\hbar\omega_a}{2E_L}}\sqrt[4]{\frac{\omega_1}{\omega_a}} \\ \phi_b &= \cos\theta\sqrt{\frac{\hbar\omega_a}{2E_L}}\sqrt[4]{\frac{\omega_2}{\omega_a}} \end{aligned} \quad (3.14)$$

are zero-point fluctuations of the two modes as seen by the Josephson junction and

$$\xi = 2\phi_a\text{Re}\alpha + 2\phi_b\text{Re}\beta \quad (3.15)$$

is a renormalized pump amplitude. Here the mode $\tilde{\mathbf{a}}$ is closer to the initial oscillator mode \mathbf{a} and the mode $\tilde{\mathbf{b}}$ is closer to the junction mode ($\phi_a \ll \phi_b$). In contrast to the unshunted case, this change of variables ensures that both modes remain close to their ground state. This is a direct consequence of the harmonic confinement and will be confirmed through numerical simulations.

Under this change of variables, the operator $i(\mathbf{a}^\dagger - \mathbf{a})$ appearing in the coupling to the bath Eq. (3.2) is replaced by

$$i\cos\theta\sqrt[4]{\frac{\omega_1}{\omega_a}}(\tilde{\mathbf{a}}^\dagger - \tilde{\mathbf{a}}) + i\sin\theta\sqrt[4]{\frac{\omega_2}{\omega_a}}(\tilde{\mathbf{b}}^\dagger - \tilde{\mathbf{b}}). \quad (3.16)$$

The new system-bath coupling is given by

$$\begin{aligned} \tilde{\mathbf{H}}_{\text{SB}} = & \sum_k \hbar\omega_k \mathbf{c}^\dagger[\omega_k] \mathbf{c}[\omega_k] \\ & - \sum_k \hbar\Omega[\omega_k] \cos\theta \sqrt{\frac{\omega_1}{\omega_a}} \left(\tilde{\mathbf{a}}^\dagger - \tilde{\mathbf{a}} \right) \left(\mathbf{c}^\dagger[\omega_k] - \mathbf{c}[\omega_k] \right) \\ & - \sum_k \hbar\Omega[\omega_k] \sin\theta \sqrt{\frac{\omega_2}{\omega_a}} \left(\tilde{\mathbf{b}}^\dagger - \tilde{\mathbf{b}} \right) \left(\mathbf{c}^\dagger[\omega_k] - \mathbf{c}[\omega_k] \right) \end{aligned} \quad (3.17)$$

The transformations applied on Eqs. (3.1)-(3.2) and leading to Eqs. (3.13)-(3.17) can be summarized as, in order, a Bogoliubov transformation \mathbf{U}_{s1} , a beam-splitter type unitary \mathbf{U}_θ , a displacement of the frame \mathbf{D} and another Bogoliubov transformation \mathbf{U}_{s2} given by

$$\begin{aligned} \mathbf{U}_{s1} &= \exp\left(\frac{\zeta}{2}(\mathbf{b}^{\dagger 2} - \mathbf{b}^2)\right) \\ \mathbf{U}_\theta &= \exp(\theta(\mathbf{a}\mathbf{b}^\dagger - \mathbf{a}^\dagger\mathbf{b})) \\ \mathbf{D} &= \exp(\alpha^*(t)\mathbf{a} - \alpha(t)\mathbf{a}^\dagger) \exp(\beta^*(t)\mathbf{b} - \beta(t)\mathbf{b}^\dagger) \\ \mathbf{U}_{s2} &= \exp\left(\frac{\zeta_a}{2}(\mathbf{a}^{\dagger 2} - \mathbf{a}^2)\right) \exp\left(\frac{\zeta_b}{2}(\mathbf{b}^{\dagger 2} - \mathbf{b}^2)\right). \end{aligned} \quad (3.18)$$

where $\mathbf{b} = (\varphi + i\mathbf{N})/\sqrt{2}$ and

$$\begin{aligned} \theta &= -\frac{1}{2} \arctan\left[\frac{2\hbar g\sqrt{2E_L\hbar\omega_a}}{(\hbar\omega_a)^2 - 8E_C E_L}\right], \\ \alpha(t) &= \frac{A_p \cos\theta}{\omega_p^2 - \omega_a\omega_1} (\omega_p \sin(\omega_p t) + i\omega_a \cos(\omega_p t)), \\ \beta(t) &= \frac{A_p \sin\theta}{\omega_p^2 - \omega_a\omega_2} (\omega_p \sin(\omega_p t) + i\omega_a \cos(\omega_p t)), \\ \zeta &= \log\left(\sqrt{\frac{E_L}{\hbar\omega_a}}\right), \\ \zeta_a &= \log\left(\sqrt[4]{\frac{\omega_a}{\omega_1}}\right), \quad \zeta_b = \log\left(\sqrt[4]{\frac{\omega_a}{\omega_2}}\right), \end{aligned} \quad (3.19)$$

with

$$\begin{aligned} \omega_1 &= \omega_a \cos^2\theta + \frac{8E_C E_L}{\hbar^2\omega_a} \sin^2\theta - g\sqrt{\frac{2E_L}{\hbar\omega_a}} \sin(2\theta), \\ \omega_2 &= \omega_a \sin^2\theta + \frac{8E_C E_L}{\hbar^2\omega_a} \cos^2\theta + g\sqrt{\frac{2E_L}{\hbar\omega_a}} \sin(2\theta). \end{aligned} \quad (3.20)$$

3.2 Simulations in the Floquet-Markov framework for weak dissipation

I carried out numerical simulations of the driven dissipative system Eqs. (3.13)-(3.17) in the Floquet-Markov framework, similarly to the analysis done on the (unshunted) transmon circuit in section 2.3. Although the simulations are run here in the Fock states basis of the two modes $\tilde{\mathbf{a}}$ and $\tilde{\mathbf{b}}$, I show and plot the results in the shunted transmon

basis $\{|\nu_k\rangle\}_k$ (eigenstates of the Hamiltonian $4E_C\mathbf{N}^2 + E_L\varphi^2/2 - E_J\cos\varphi$) to ease the comparison with results from the previous chapter. Here, the parameters are chosen such that the bare frequencies, impedances and coupling of the harmonic oscillator and the transmon mode coincide with those of chapter 2. The important change concerns the dilution of the nonlinearity by the addition of the harmonic shunt with an energy E_L , about a factor 2 larger than E_J .

The populations of the $\tilde{\mathbf{a}}$ mode remain very close to its ground state over the whole range of pump values, even more than in the regular transmon case. In a similar way, the populations of the $\tilde{\mathbf{b}}$ mode, as shown on Fig. 3.2, remain very close to the ground state, with a slight increase with the pump power. Both modes remain much closer to their ground state than their counterpart in chapter 2. The state $\rho_{ss}(0)$ follows a very smooth behavior and, as shown on Fig. 3.3, the impurity of ρ_{ss} (black crosses, right axis) remains close to zero (below 3% for the whole pump range).

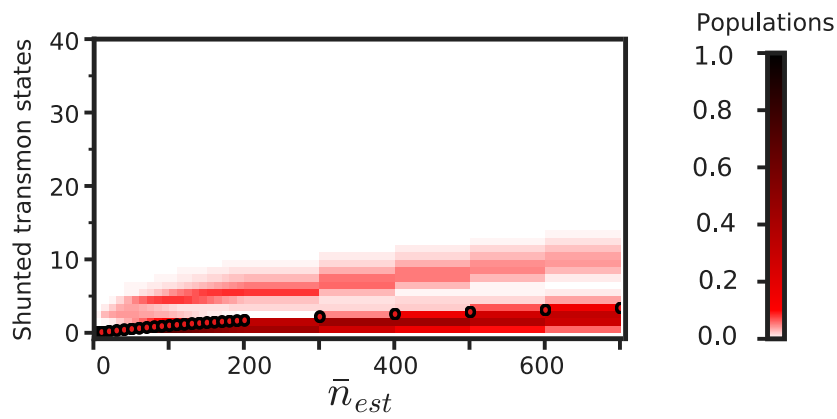


Figure 3.2: **Populations of the shunted transmon eigenstates $\{|\eta_k\rangle\}_k$ in the steady state $\rho_{ss}(0)$ of Eqs. (3.13)-(3.17) as a function of the pump power, as computed with a Floquet-Markov approach.** The parameters are taken to be $E_c/\hbar = 150$ MHz, $E_J/\hbar = 6$ GHz, $E_L/\hbar = 14$ GHz, $g/2\pi = 140$ MHz, $\omega_a/2\pi = 5.5$ GHz and $\omega_p/2\pi = 6$ GHz. Here, \bar{n}_{est} is an estimation of the number of circulating photons \bar{n} , where I use the bare oscillator frequency instead of the dressed one. The red dots indicate the average number of excitations in the transmon mode. The parameters are chosen to be comparable with the results from chapter 2.

Fig. 3.3 also illustrates the ac Stark shifted frequency of the resonator mode. In contrast to the (unshunted) transmon case, this frequency is now well-defined for all values of the pump power. As a result, I could extend the study to much higher pump powers. As illustrated in Fig. 3.4, the ac Stark shifted frequency is well-defined over a wide range of pump powers and exhibit a smooth oscillating behavior decaying to $\tilde{\omega}_a$.

3.3 Rotating wave approximations results and comparison with numerical simulations

The Hamiltonian Eq. (3.13) can easily be time averaged following methods from [19]. This section focuses on comparing the numerical results from the Floquet-Markov method with those from time-averaging methods for a shunted transmon circuit coupled to an

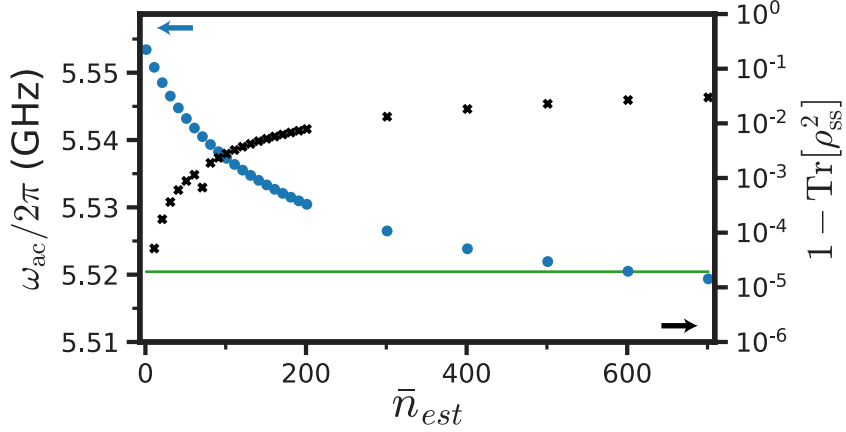


Figure 3.3: **Impurity of the steady state $\rho_{ss}(0)$ and ac Stark shifted frequencies of the oscillator as a function of the pump power.** The black crosses (right-hand axis) correspond to the impurity of the whole (tensor) steady state. The steady state quickly becomes very mixed, even for small pump strengths. The blue dots (left-hand axis) correspond to the ac Stark shifted frequencies of the oscillator as a function of the pump power. The green horizontal line corresponds to the renormalized oscillator frequency $\tilde{\omega}_a$. The frequency is unique and well-defined for all pump powers. This is also reflected by the impurity of the steady state which remains smaller than 3%. The abscissa is the same as in Fig. 3.2, using an estimation of the number of circulating photons, \bar{n}_{est} . Parameters are the same as in Fig. 3.2.

oscillator. Starting from the Hamiltonian from Eq. (3.13)

$$\begin{aligned} \tilde{\mathbf{H}}_{\text{shunt}}(t) = & \hbar\tilde{\omega}_a \tilde{\mathbf{a}}^\dagger \tilde{\mathbf{a}} + \hbar\tilde{\omega}_b \tilde{\mathbf{b}}^\dagger \tilde{\mathbf{b}} \\ & - E_J \cos \left[\phi_a (\tilde{\mathbf{a}} + \tilde{\mathbf{a}}^\dagger) + \phi_b (\tilde{\mathbf{b}} + \tilde{\mathbf{b}}^\dagger) \right] \cos [\xi \sin (\omega_p t)] \\ & + E_J \sin \left[\phi_a (\tilde{\mathbf{a}} + \tilde{\mathbf{a}}^\dagger) + \phi_b (\tilde{\mathbf{b}} + \tilde{\mathbf{b}}^\dagger) \right] \sin [\xi \sin (\omega_p t)] \end{aligned} \quad (3.21)$$

one can perform a first-order time-averaging following the methods from [19]. The first order time-averaged Hamiltonian is defined as

$$\begin{aligned} \tilde{\mathbf{H}}_{\text{shunt}}^{\text{RWA}} = & \frac{1}{T} \int_0^T \tilde{\mathbf{H}}_{\text{shunt}}(t) dt \\ = & \hbar\tilde{\omega}_a \tilde{\mathbf{a}}^\dagger \tilde{\mathbf{a}} + \hbar\tilde{\omega}_b \tilde{\mathbf{b}}^\dagger \tilde{\mathbf{b}} - E_J J_0(\xi) \cos \left[\phi_a (\tilde{\mathbf{a}} + \tilde{\mathbf{a}}^\dagger) + \phi_b (\tilde{\mathbf{b}} + \tilde{\mathbf{b}}^\dagger) \right] \end{aligned} \quad (3.22)$$

where $T = 2\pi/\omega_p$ and $J_0(\cdot)$ represents the Bessel function of the first kind and zero order.

As shown on Fig. 3.4, the ac Stark shifted frequency curve from Fig. 3.4 is in good agreement with the first-order predictions by a model resulting from time-averaging the Hamiltonian Eq. (3.13) to lowest order. Additionally, the observed jump in the ac Stark shift of the (unshunted) transmon from chapter 2 appears at pump strengths much lower than the first oscillation of this Bessel function. Therefore, an experimental observation of such an oscillating behavior would prove a striking difference between the (unshunted) case and the circuit with an inductance shunt discussed in this chapter.

Moreover, the previous analysis tend to indicate that the strengths of various types of nonlinear Hamiltonians could be tuned. As an example, I will focus on the strength

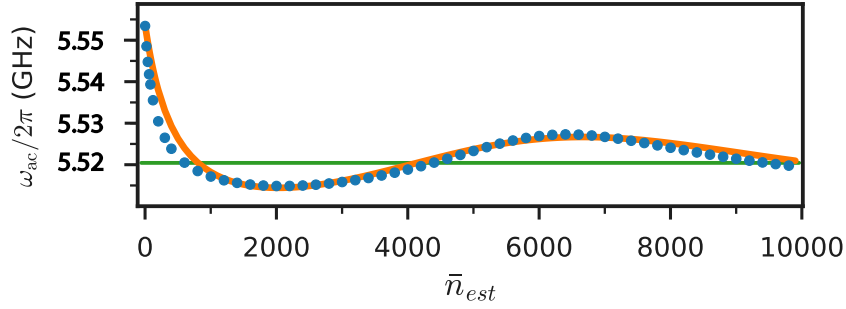


Figure 3.4: **ac Stark shifted frequencies of the oscillator with rotating wave approximations as a function of the pump power.** The orange curve represents the oscillator frequency found by numerically diagonalizing the time-averaged Hamiltonian Eq. (3.22) of the system. The blue dots correspond to the ac Stark shifted frequencies of the oscillator, found from the numerical Floquet-Markov approach, as a function of the pump power. The green horizontal line corresponds to the renormalized oscillator frequency $\tilde{\omega}_a$. The abscissa is the same as in Fig. 3.2, using an estimation of the number of circulating photons, \bar{n}_{est} . Parameters are the same as in Fig. 3.2.

of the induced Kerr of the mode $\tilde{\mathbf{a}}$, which is the leading order nonlinear effect in circuit QED experiments.

The induced Kerr strength of the mode $\tilde{\mathbf{a}}$ can be computed from the Floquet-Markov numerical simulations in a similar fashion as the ac Stark shifted frequency, in a cascading scheme. Indeed, starting from the steady state $\rho_{ss}(0)$, I list the possible transitions between Floquet states in the steady state and any other Floquet state. Their transition frequencies correspond to the ac Stark shifted frequencies as detailed in section 2.3.1. Then, starting from this set of Floquet states coupled to those of the steady state, the same procedure can be repeated to find a second set of transition frequencies, to a second set of Floquet states. The Kerr strength is then computed as the difference between the second and the first such transition frequency. The induced Kerr strength can also be computed from the time-averaged model Eq. (3.22) by diagonalizing this Hamiltonian and looking at the transition frequencies. The Kerr strength is given by the difference of the second and first oscillator-like transition frequencies in this Hamiltonian.

Both the numerical estimation of the Kerr strength from the Floquet-Markov theory and from the time-averaged model are plotted in Fig. 3.5. First, the Kerr term vanishes for high enough powers. This ability in cancelling the leading order nonlinear effects by merely tuning a pump power will be an extremely useful tool for circuit QED experiments [70]. Furthermore, the estimation from the time-averaged model (orange curve) is in qualitative agreement with the numerical results in the Floquet-Markov framework. One should note that I only performed a first-order rotating wave approximation here and a more precise approximation would require to perform higher order time averaging.

3.4 Choice of parameters for the shunted transmon circuit

The simulations of the section 3.2 have been performed with the same parameters as in the unshunted case, except for the Josephson energy that has been taken to be $E_J/\hbar = 6$ GHz and the addition of $E_L/\hbar = 14$ GHz. Noting that the sum of these two energies correspond to the Josephson energy in the unshunted case, this choice allows to keep the bare frequency of the transmon mode the same. This, however, comes at the

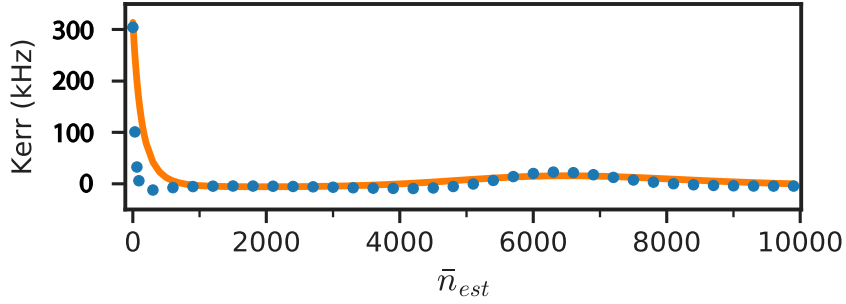


Figure 3.5: **Strength of the induced Kerr of the most linear mode $\tilde{\mathbf{a}}$.** The induced Kerr effect is defined as the difference between the transition frequencies for the second and the first excitations. The orange curve corresponds to the expected induced Kerr strength computed from the time-averaged model Eq. (3.22) while the blue dots are results from the Floquet-Markov numerical simulations. The abscissa is the same as in Fig. 3.2, using an estimation of the number of circulating photons, \bar{n}_{est} . Parameters are the same as in Fig. 3.2.

expense of diluting the nonlinearity of the transmon mode. Indeed, the anharmonicity of the shunted transmon mode is given by 37 MHz, to be compared to 143 MHz in the unshunted case. In the same way, the induced Kerr on the cavity of 306 kHz is weaker than the value of 655 kHz for the unshunted case. The shallower slope of the ac Stark shifted frequency in Fig. 3.3 (with respect to Fig. 2.5) can be explained through this difference.

Using a different set of parameters, one can achieve similar nonlinearities for both systems under consideration. For instance, by choosing $E_C/\hbar = 450$ MHz, $E_J/\hbar = 2.22$ GHz, $E_L/\hbar = 4.44$ GHz, $g/2\pi = 245$ MHz, $\omega_a = 5.5$ GHz, we achieve similar frequencies and nonlinearities to the shunted case. More precisely, in the absence of the pump, we find a cavity frequency of 5.545 GHz (5.545 GHz for the unshunted case), a qubit frequency of 4.7 GHz (4.691 GHz for the unshunted case), a qubit anharmonicity of 123 MHz (143 MHz for the unshunted case), an induced cavity Kerr of 600 kHz (655 kHz for the unshunted case) and a cross Kerr between the qubit and the cavity of 15.5 MHz (17.3 MHz for the unshunted case).

In Fig. 3.6(a), I plot and compare the shifted cavity frequencies in the shunted and unshunted case (blue dots, left axis). The slope near $\bar{n}_{est} = 0$ of the variation of frequency versus the photon number \bar{n}_{est} is now very close to that of the unshunted case. I also plot the impurity of the steady state in both cases versus the pump power (black and gray crosses, right axis). One clearly observes a much purer and smoother behavior for the shunted case with respect to the unshunted one. In Fig. 3.6(b) and (c), I plot the shifted cavity frequency and induced Kerr effect over a larger range of pump powers for the shunted case with this new set of parameters. The behavior is similar to the one shown in Fig. 3.2 and Fig. 3.3. As a result of the increased nonlinearity, the range of values taken by the Kerr strength is twice larger than in the simulations from section 3.3.

In these simulations, similar to the previous set of parameters, I have chosen a ratio between E_L and E_J of about 2. Noting that a large ratio between E_L and E_J leads to the dilution of the Josephson junction nonlinearity, one may consider the possibility of choosing a smaller ratio. This, however, comes at the expense of losing the purity of the steady state and therefore getting closer to the asymptotic behavior of the unshunted case. In order to illustrate this, I perform numerical simulations with

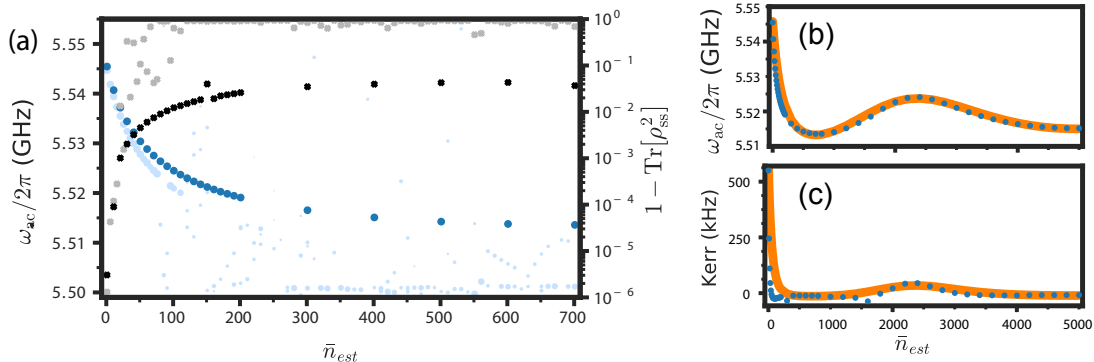


Figure 3.6: **Floquet-Markov simulations of the shunted transmon with parameters** $E_C/\hbar = 450$ MHz, $E_J/\hbar = 2.22$ GHz, $E_L/\hbar = 4.44$ GHz, $g/2\pi = 245$ MHz, $\omega_a = 5.5$ GHz. (a) Blue dots correspond to the ac Stark shifted frequencies of the oscillator as a function of the pump power. For comparison, the results for the unshunted case with the parameters of Fig. 2.5 are reproduced as pale blue dots (left axis). The impurity of the steady state is plotted as black crosses (gray crosses for the unshunted case, right axis). The abscissa is the same as in Fig. 3.2, using an estimation of the number of circulating photons, \bar{n}_{est} . (b) ac Stark shifted frequency of the shunted transmon over an extended range of pump powers. The blue dots correspond to the Floquet-Markov simulations results while the orange curve indicates the expected values from a time-averaged model from section 3.3. This is to be compared with Fig. 3.4. (c) Induced Kerr strength over the same extended range, to be compared with Fig. 3.5.

the same parameters as in Fig. 3.3, except for E_J and E_L . Indeed, I fix their sum $(E_J + E_L)/\hbar = 6.66$ GHz and let vary the ratio between them. In Fig. 3.7, I provide the impurity of the steady state as a function of the pump power for three different choices of the ratio $r = E_L/E_J$. As it can be seen, a ratio of 2, as chosen in the simulations in section 3.2, ensures globally a purer steady state and this purity is lost for smaller ratios.

There is still an open question here in the effect of the ratio $r = E_L/E_J$. From numerical investigation, it seems that adding a shunt inductance is not enough to ensure the stability of the circuit over a wide range of pump amplitudes, one has to take a large enough ratio of the inductive energy and Josephson energy. From previous numerical simulations, a ratio of about 2 seems to be a minimum to ensure the stability of the circuit and both the effect of this ratio and the threshold values to ensure stability were only studied in a numerical way here. This is the subject of ongoing research in the QUANTIC team at INRIA, mainly from M. Burgelman who is starting his PhD on this subject, trying to analytically investigate the behavior of the transmon device and the shunted transmon one, first from a classical dynamics point of view and with the tools of the classical dynamic stability analysis.

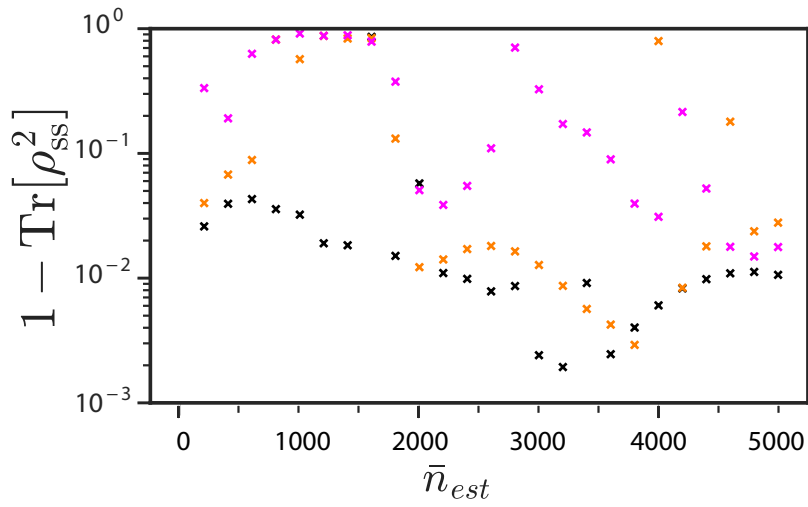


Figure 3.7: **Impurity of the steady state as a function of the pump power.** I use the same parameters as in Fig. 3.6, except for E_J and E_L . While the sum $(E_J + E_L)/\hbar = 6.66$ GHz is fixed, I consider here three different choices for their ratio $r = E_L/E_J$. The black crosses correspond to $r = 2$ ($E_L/\hbar = 4.44$ GHz and $E_J/\hbar = 2.22$ GHz), the orange ones to $r = 1.5$ ($E_L/\hbar = 4$ GHz and $E_J/\hbar = 2.66$ GHz) and the magenta ones to $r = 1$ ($E_L/\hbar = E_J/\hbar = 3.33$ GHz).

Chapter 4

Floquet-Markov simulations

Contents

4.1	Steady-state computation framework	54
4.1.1	Encoding the circuit Hamiltonian	55
4.1.2	Floquet code	60
4.1.3	Running simulations	63
4.2	Analysis code	65
4.2.1	Resonant frequencies of the system	65
4.2.2	Induced Kerr strength	66

The simulation code is organized in the form of a Python package, designed so that the simulated circuit could easily be edited and modified, in order to investigate various types of circuits using the same approach. So far, the same code has been used to simulate the transmon coupled to a cavity from Chapter 2 and the circuit with an extra shunt inductance from Chapter 3.

All the numerical simulations detailed and discussed in this manuscript were run on a (high-end) desktop workstation with an Intel Core i7-6700 CPU and 16 GB of RAM running Linux. Simulations are running in Python 3.5.2 using a modified version of QuTiP 4.2.0 [71, 72], along with Numpy 1.14.0 [73], Scipy 1.0.0 [74], Cython 0.27.3 [75]. All the figures are generated using Matplotlib 2.1.1 [76].

The simulations are performed in two steps:

- First, a Floquet simulation framework, written as a Python package, is used to run simulations for different sets of Hamiltonians and values of physical parameters of the system. This code computed the steady state of the system using a Floquet-Markov approach and outputs a dump of simulated data (populations of the Floquet modes in the steady state $\rho_{ss}(0)$).
- Then, a set of scripts were written to make further analysis of the dynamics of the system, from its computed steady state. These would compute the transition frequencies for instance, as shown in figures from Chapters 2 and 3.

As the computation of the steady state of the systems under consideration is quite long, this two steps approach lets the user do the steady state computation once and then perform as many different analysis as required on top of it. Indeed, for the unshunted case presented in Chapter 2 and in the displaced frame described in section 2.2, a truncation of about 50 transmon states and ten oscillator Fock states was required. For the shunted case and using the displaced frame described in section 3.1, a truncation of about 20 Fock states of the non-linear mode and ten Fock states of the linear one should be used. Such large truncations result in a running time of about one hour to compute the steady state $\rho_{ss}(0)$ of the system for a single pump power.

This Chapter is a walkthrough guide to the simulation code used for plotting the figures from Chapters 2-3, detailing both the numerical methods as well as the architectural choices for easing the reuse of this code as a framework for Floquet simulations of superconducting circuits systems. This code was reused by Jaya Venkatraman from QuLab at Yale University for her work on physically implementing the theoretical proposal of adding an extra shunt inductance to the transmon circuit in Chapter 2. The full code is available at <https://gitlab.inria.fr/lverney/floquet-markov-for-josephson-circuits>. QuTiP code presented in this manuscript is licensed under a New BSD license while the rest of the code is licensed under an MIT license.

4.1 Steady-state computation framework

The steady state computation starts by computing the Floquet modes from the Hamiltonian of the system and then builds the stochastic transition matrix R from Eq. (2.28), from which the steady state can be inferred. This whole procedure is described in the next subsections where I will focus on specific code extracts.

4.1.1 Encoding the circuit Hamiltonian

First, let us focus on the way I am encoding the circuit Hamiltonian. Note that in this code, the pump amplitude slightly differs from the notations from Chapters 2 and 3. Here, the pump term reads

$$\hbar\varepsilon_p \cos(\omega_p t) \mathbf{X}_a \quad (4.1)$$

with \mathbf{X}_a one of the two quadratures of the harmonic oscillator from the \mathbf{a} mode.

In Chapters 2 and 3, I was using the amplitude of the pump as primary input and deducing an approximate value of the number of circulating photons at the pump frequency, \bar{n}_{est} from this value. For practical reasons, I am here using the estimated number of circulating photons \bar{n}_{est} (denoted by the variable `n_bar` in the code) and inferring a pump amplitude from it. The pump amplitude for a given \bar{n}_{est} value can be computed using the function

```
def compute_epsilon_p(n_bar, p):
    """
    Compute the pump amplitude as a function of a rough approximation of
    ``n_bar``.
    """
    return np.sqrt(n_bar) * np.sqrt(8) * (p['omega_p'] - p['omega_a'])
```

Transmon coupled to a cavity Hamiltonian

One can then define a function to build the Hamiltonian representation for the system under consideration. The parameters in the Python code are related to the parameters from Chapters 2 and 3 by

$$\begin{aligned} \varepsilon_c &= E_C/\hbar \\ \varepsilon_j &= E_J/\hbar \\ \varepsilon_l &= E_L/\hbar \\ \varepsilon_g &= g\sqrt{2}. \end{aligned} \quad (4.2)$$

For the transmon case from Chapter 2, this is

```
def build_unshunted_hamiltonian(N_max_a, N_max_b, N_max_charge, epsilon_p, p):
    """
    :param N_max_a: Truncation on the cavity Fock space.
    :param N_max_b: Truncation on the transmon eigenstates space.
    :param N_max_charge: To compute the transmon eigenvectors, we use the
        representation in the charge states basis. This is the truncation in
        this space and should be really large (indices range from -N_max_charge
        to +N_max_charge).
    :param epsilon_p: Pump amplitude.
    :param p: Dict of parameters values.
    :returns: A tuple of H, args, H_0_cavity and c_ops.
    """
    # Preconditions
    assert N_max_b < (2 * N_max_charge + 1)

    # Operators on the cavity
    a = qutip.destroy(N_max_a)
    X_a = (a + a.dag()) / np.sqrt(2)
```

```

Id_a = qutip.qeye(N_max_a)

# Operators on the transmon, in charge state representation
N_ch = qutip.Qobj(np.diag(range(-N_max_charge, N_max_charge + 1)))
cos_phi = qutip.Qobj(
    np.diag(0.5 * np.ones(2 * N_max_charge), k=1) +
    np.diag(0.5 * np.ones(2 * N_max_charge), k=-1)
)
sin_phi = qutip.Qobj(
    np.diag(-0.5j * np.ones(2 * N_max_charge), k=1) +
    np.diag(0.5j * np.ones(2 * N_max_charge), k=-1)
)
Id_ch = qutip.qeye(2 * N_max_charge + 1)

# Transmon hamiltonian to find transmon eigenstates
H_tr = qutip.Qobj(
    4.0 * p['epsilon_c'] * (N_ch - p['N_g'] * Id_ch)**2 +
    -1.0 * p['epsilon_j'] * cos_phi
)
_, eigvec_tr = H_tr.eigenstates()
# Matrix to pass from charge states basis to transmon basis. Each column is
# a transmon eigenstate expressed in the charge states basis.
change_basis_matrix = qutip.Qobj(
    np.column_stack(x.full() for x in eigvec_tr)
)
# Then, rewrite transmon operators in this basis
N_ch_eigv_basis = change_basis(N_ch, change_basis_matrix)
cos_phi_eigv_basis = change_basis(cos_phi, change_basis_matrix)
sin_phi_eigv_basis = change_basis(sin_phi, change_basis_matrix)
# and truncate them to keep only N_max_b components.
N_ch_eigv_basis = qutip.Qobj(N_ch_eigv_basis[:N_max_b, :N_max_b])
cos_phi_eigv_basis = qutip.Qobj(cos_phi_eigv_basis[:N_max_b, :N_max_b])
sin_phi_eigv_basis = qutip.Qobj(sin_phi_eigv_basis[:N_max_b, :N_max_b])
Id_ch_eigv_basis = qutip.qeye(N_max_b)

# Cavity + transmon tensor operators in Fock tensor eigenstates of transmon
# space
N_a_tensor = qutip.tensor(a.dag() * a, Id_ch_eigv_basis)
X_a_tensor = qutip.tensor(X_a, Id_ch_eigv_basis)
N_ch_tensor = qutip.tensor(Id_a, N_ch_eigv_basis)
cos_phi_tensor = qutip.tensor(Id_a, cos_phi_eigv_basis)
sin_phi_tensor = qutip.tensor(Id_a, sin_phi_eigv_basis)
Id_tensor = qutip.tensor(Id_a, Id_ch_eigv_basis)

# Time-independent part of hamiltonian
H_0_cavity = p['omega_a'] * N_a_tensor
H_0_coupling = (
    p['epsilon_g'] * (N_ch_tensor - p['N_g'] * Id_tensor) * X_a_tensor
)
H_0_qubit = 4.0 * p['epsilon_c'] * (N_ch_tensor - p['N_g'] * Id_tensor)**2
H_0 = (
    H_0_cavity +
    H_0_coupling +
    H_0_qubit
)

# Time-dependent part
oscillating_prefactor = (
    -1.0 * p['epsilon_g'] * epsilon_p *
    p['omega_a'] / p['omega_p'] / (p['omega_p']**2 - p['omega_a']**2)
)

```

```

H_1 = -1.0 * p['epsilon_j'] * cos_phi_tensor
H_1_coef = 'cos(oscillating_prefactor * sin(omega_p * t))'
H_2 = p['epsilon_j'] * sin_phi_tensor
H_2_coef = 'sin(oscillating_prefactor * sin(omega_p * t))'
# Complete QuTiP hamiltonian object
args = {
    'oscillating_prefactor': oscillating_prefactor,
    'omega_p': p['omega_p']
}
H = [H_0, [H_1, H_1_coef], [H_2, H_2_coef]]

# Dissipation operators
c_ops = [X_a_tensor]

return H, args, H_0_cavity, c_ops

```

Inductively shunted transmon coupled to a cavity Hamiltonian

Similarly, a function is available to define the Hamiltonian of the system shunted with an extra inductance in Chapter 3:

```

def build_shunted_hamiltonian(N_max_a, N_max_b, epsilon_p, p):
    """
    :param N_max_a: Truncation on the cavity Fock space.
    :param N_max_b: Truncation on the shunted transmon eigenstates space.
    :param epsilon_p: Pump amplitude.
    :param p: Dict of parameters values.
    :returns: A tuple of H, args, H_0_cavity and c_ops.
    """
    (
        omega_bar_a, omega_bar_q,
        r, s,
        oscillating_prefactor,
        c_op_r, c_op_s
    ) = compute_shunted_parameters(epsilon_p, p)

    # Operators on the cavity
    a = qutip.destroy(N_max_a)
    X_a = (a + a.dag()) / np.sqrt(2)
    P_a = (a - a.dag()) / 1.0j / np.sqrt(2)
    Id_a = qutip.qeye(N_max_a)
    # Operators on the transmon
    b = qutip.destroy(N_max_b)
    X_b = (b + b.dag()) / np.sqrt(2)
    P_b = (b - b.dag()) / 1.0j / np.sqrt(2)
    Id_b = qutip.qeye(N_max_b)
    # Compute tensor operators
    Id_tensor = qutip.tensor(Id_a, Id_b)
    X_a_tensor = qutip.tensor(X_a, Id_b)
    P_a_tensor = qutip.tensor(P_a, Id_b)
    X_b_tensor = qutip.tensor(Id_a, X_b)
    P_b_tensor = qutip.tensor(Id_a, P_b)

    # Time independent part of hamiltonian in Fock basis
    H_0_cavity = 0.5 * omega_bar_a * (
        X_a_tensor**2 + P_a_tensor**2
    )
    H_0_qubit = 0.5 * omega_bar_q * (
        X_b_tensor**2 + P_b_tensor**2
    )

```

```

H_0 = H_0_cavity + H_0_qubit

# Time dependent part in Fock basis
phi_X_tensor = (r * X_b_tensor - s * X_a_tensor)
exp_j_phi_X_tensor = (1.0j * phi_X_tensor).expm()
H_1 = -0.5 * p['epsilon_j'] * (
    exp_j_phi_X_tensor + exp_j_phi_X_tensor.dag()
)
H_1_coef = 'cos(oscillating_prefactor * sin(omega_p * t))'
H_2 = -0.5j * p['epsilon_j'] * (
    exp_j_phi_X_tensor - exp_j_phi_X_tensor.dag()
)
H_2_coef = 'sin(oscillating_prefactor * sin(omega_p * t))'

# Rewrite everything in transmon eigenbasis
_, eigenvec = (H_0 + H_1).eigenstates()
H_0_cavity_eigv_basis = (
    H_0_cavity.transform(eigenvec) -
    0.5 * omega_bar_a * Id_tensor
)
H_0_eigv_basis = H_0.transform(eigenvec)
H_1_eigv_basis = H_1.transform(eigenvec)
H_2_eigv_basis = H_2.transform(eigenvec)

# Complete QuTiP hamiltonian object
args = {
    'oscillating_prefactor': oscillating_prefactor,
    'omega_p': p['omega_p']
}
H = [
    H_0_eigv_basis,
    [H_1_eigv_basis, H_1_coef],
    [H_2_eigv_basis, H_2_coef]
]

# Dissipation operators
c_ops = [
    (c_op_r * X_a_tensor + c_op_s * X_b_tensor).transform(eigenvec)
]

return H, args, H_0_cavity_eigv_basis, c_ops

```

where an auxiliary function, `compute_shunted_parameters`, is used to compute the renormalized parameters entering in the Hamiltonian construction. These come from the change of frame performed in section 3.1.

```

def compute_shunted_parameters(epsilon_p, p):
    theta = -0.5 * np.arctan(
        2 * p['epsilon_g'] * np.sqrt(p['epsilon_l'] * p['omega_a']) /
        (p['omega_a']**2 - 8 * p['epsilon_c'] * p['epsilon_l'])
    )

    omega_tilde_a = (
        p['omega_a'] * np.cos(theta)**2 +
        (
            8 * p['epsilon_c'] * p['epsilon_l'] / p['omega_a'] *
            np.sin(theta)**2
        ) +
        (
            -1.0 * p['epsilon_g'] *
            np.sqrt(p['epsilon_l'] / p['omega_a']) * np.sin(2 * theta)
        )
    )

```

```

    )
)
omega_tilde_q = (
    p['omega_a'] * np.sin(theta)**2 +
    (
        8 * p['epsilon_c'] * p['epsilon_l'] / p['omega_a'] *
        np.cos(theta)**2
    ) +
    (
        p['epsilon_g'] * np.sqrt(p['epsilon_l'] / p['omega_a']) *
        np.sin(2 * theta)
    )
)
omega_bar_a = np.sqrt(omega_tilde_a * p['omega_a'])
omega_bar_q = np.sqrt(omega_tilde_q * p['omega_a'])

# For dissipation
c_op_r = np.cos(theta) * np.power(p['omega_a'] / omega_tilde_a, 0.25)
c_op_s = np.sin(theta) * np.power(p['omega_a'] / omega_tilde_q, 0.25)

r = (
    np.cos(theta) * np.sqrt(p['omega_a'] / p['epsilon_l']) *
    np.power(omega_tilde_q / p['omega_a'], 0.25)
)
s = (
    np.sin(theta) * np.sqrt(p['omega_a'] / p['epsilon_l']) *
    np.power(omega_tilde_a / p['omega_a'], 0.25)
)

oscillating_prefactor = (
    0.5 * np.sqrt(p['omega_a'] / p['epsilon_l']) *
    epsilon_p * p['omega_p'] * np.sin(2 * theta) * (
        1.0 / (p['omega_p']**2 - p['omega_a'] * omega_tilde_q) -
        1.0 / (p['omega_p']**2 - p['omega_a'] * omega_tilde_a)
    )
)

return (
    omega_bar_a, omega_bar_q,
    r, s,
    oscillating_prefactor,
    c_op_r, c_op_s
)

```

Generic Hamiltonian construction

Finally, based on the parameters provided to the simulation framework, a generic `build_hamiltonian` function is calling the correct procedure to build the system Hamiltonian (with or without an extra shunt inductance for instance). This function can easily be extended to take into account other circuits, such as an array of Josephson junctions.

```

def build_hamiltonian(N_max_a, N_max_b, n_bar, p,
                    logger, out_directory, compute_kerr=False,
                    N_max_charge=100):
    """
    :param N_max_a: Truncation on the cavity Fock space.
    :param N_max_b: Truncation on the transmon eigenstates space.
    :param n_bar: Mean number of photons in the pump, at  $\omega_p$ .
    :param p: Dict of parameters values.
    """

```

```

:param logger: A logger object.
:param out_directory: Where to output images.
:param compute_kerr: Whether Kerr should be computed or not.
:param N_max_charge: To compute the transmon eigenvectors, we use the
    representation in the charge states basis. This is the truncation in
    this space and should be really large (indices range from -N_max_charge
    to +N_max_charge).
:returns: A tuple of H, args, c_ops and computed params.
"""
# Compute corresponding pump amplitude
epsilon_p = compute_epsilon_p(n_bar, p)

# Note: This is the place where we define the hamiltonian and the collapse
# operators. Currently, only shunted transmon and unshunted (regular)
# transmon are supported. You can easily extend this to match your specific
# hamiltonian.
if 'epsilon_l' in p and p['epsilon_l'] > 0:
    logger.info('Building shunted hamiltonian...')
    H, args, H_0_cavity, c_ops = build_shunted_hamiltonian(
        N_max_a, N_max_b, epsilon_p, p
    )
else:
    logger.info('Building unshunted hamiltonian...')
    H, args, H_0_cavity, c_ops = build_unshunted_hamiltonian(
        N_max_a, N_max_b, N_max_charge, epsilon_p, p
    )

# Compute kerr and plot eigvals
computed_params = []
if compute_kerr:
    computed_params = compute_eigvals_kerr_f_0(
        H[0] + H[1][0],
        H_0_cavity,
        p,
        out_directory
    )
    logger.info('Kerr value is %g MHz.', computed_params[0] * 1e3)
    logger.info('Frequency at nbar=0 is %g GHz.', computed_params[1])

return H, args, c_ops, computed_params

```

4.1.2 Floquet code

The Floquet code I used for these simulations is derived from the code from QuTiP 4.2.0 [71]. This provides functions to compute the Floquet modes (`floquet.floquet_modes`) as well as their time evolution (`floquet.floquet_modes_table`). I will detail here two functions I edited for the the computation of the steady state of the system through Floquet method.

First, the `floquet_master_equation_rates` from QuTiP can be used to compute the various rates entering the master equation written in the Floquet mode basis in Eq. (2.24). This function was already available in QuTiP 4.2.0 but was suffering some performance issues, which was particularly noticeable when working with large truncations such as in the case under consideration in this manuscript. The version presented below, improving this performance issue, was submitted for integration back into QuTiP and is currently pending review.

```

def floquet_master_equation_rates(f_modes_0, f_energies, c_op, H, T,
                                  args, J_cb, w_th, kmax=5,
                                  f_modes_table_t=None, nT=100):
    """
    Calculate the rates and matrix elements for the Floquet-Markov master
    equation.

    Parameters
    -----

    f_modes_0 : list of :class:`qutip.qobj` (kets)
        A list of initial Floquet modes.

    f_energies : array
        The Floquet energies.

    c_op : :class:`qutip.qobj`
        The collapse operators describing the dissipation.

    H : :class:`qutip.qobj`
        System Hamiltonian, time-dependent with period `T`.

    T : float
        The period of the time-dependence of the hamiltonian.

    args : dictionary
        Dictionary with variables required to evaluate H.

    J_cb : callback functions
        A callback function that computes the noise power spectrum, as
        a function of frequency, associated with the collapse operator `c_op`.

    w_th : float
        The temperature in units of frequency.

    k_max : int
        The truncation of the number of sidebands (default 5).

    f_modes_table_t : nested list of :class:`qutip.qobj` (kets)
        A lookup-table of Floquet modes at times precalculated by
        :func:`qutip.floquet.floquet_modes_table` (optional).

    nT : int
        Number of steps to take in the numerical integration.

    Returns
    -----

    output : list

        A list (Delta, X, Gamma, A) containing the matrices Delta, X, Gamma
        and A used in the construction of the Floquet-Markov master equation.

    """
    N = len(f_energies)
    M = 2 * kmax + 1

    omega = (2 * pi) / T

    Delta = np.zeros((N, N, M))

```

```

X = np.zeros((N, N, M), dtype=complex)
Gamma = np.zeros((N, N, M))
A = np.zeros((N, N))

dT = T / nT
tlist = np.arange(dT, T + dT / 2, dT)

if f_modes_table_t is None:
    f_modes_table_t = floquet_modes_table(f_modes_0, f_energies,
                                          np.linspace(0, T, nT + 1), H, T,
                                          args)

c_op = c_op.full()
for t in tlist:
    # Use numpy representation to compute overlaps, which is more
    # efficient.
    f_modes_t = [
        f.full() for f in floquet_modes_t_lookup(f_modes_table_t, t, T)
    ]
    for a in range(N):
        bra_a = np.dot(np.conj(f_modes_t[a].T), c_op)
        for b in range(N):
            scalar_product = np.asscalar(np.dot(
                bra_a,
                f_modes_t[b]
            ))
            k_idx = 0
            for k in range(-kmax, kmax + 1, 1):
                X[a, b, k_idx] += (dT / T) * exp(-1j * k * omega * t) * \
                    scalar_product
                k_idx += 1

Heaviside = lambda x: ((np.sign(x) + 1) / 2.0)
for a in range(N):
    for b in range(N):
        k_idx = 0
        for k in range(-kmax, kmax + 1, 1):
            Delta[a, b, k_idx] = f_energies[a] - f_energies[b] + k * omega
            Gamma[a, b, k_idx] = 2 * pi * Heaviside(Delta[a, b, k_idx]) * \
                J_cb(Delta[a, b, k_idx]) * abs(X[a, b, k_idx]) ** 2
            k_idx += 1

for a in range(N):
    for b in range(N):
        for k in range(-kmax, kmax + 1, 1):
            k1_idx = k + kmax
            k2_idx = -k + kmax
            A[a, b] += Gamma[a, b, k1_idx] + \
                n_thermal(abs(Delta[a, b, k1_idx]), w_th) * \
                (Gamma[a, b, k1_idx] + Gamma[b, a, k2_idx])

return Delta, X, Gamma, A

```

Then, instead of relying on the `floquet.fmmsolve` function available from QuTiP which solves the full Floquet-Markov master equation, I used the fact that, under a rotating-wave approximation, the steady state of the system is diagonal in the Floquet mode basis and the populations can be found directly from an eigenvalue problem, as detailed in Eq. (2.28). Again, this results in a huge performance improvement, making it possible to effectively compute the steady state of the system under consideration in a reasonable amount of time for a large number of different parameters.

```

def floquet_master_equation_steadystate(A, safety=True):
    """
    Returns the steadystate density matrix (in the floquet basis!) for the
    Floquet-Markov master equation.

    .. note ::

        This function uses the fact that this can be simplified to an
        eigenvalue problem.

    Parameters
    -----

    A : matrix
        A matrix used to build the master equation.
    safety : bool
        Whether to check that the nullspace is well separated from the other
        eigenspaces or not (defaults to True).
    """
    # Compute auxiliary R matrix
    R = np.zeros_like(A)
    N = A.shape[0]
    for a in range(N):
        for nu in range(N):
            if a != nu:
                R[nu, a] = A[a, nu]
            else:
                R[nu, a] = -1.0 * np.sum([
                    A[a, b] for b in range(N) if b != a
                ])

    # Look for kernel of R
    eigvals, eigvecs = Qobj(R).eigenstates()
    kernel_index = np.argmin(np.abs(eigvals))
    if safety:
        # Ensure that there is a clear separation in the spectrum, which means
        # that the nullspace is well delimited and of size 1.
        assert len(eigvals[np.isclose(eigvals, eigvals[kernel_index])]) == 1

    # Qobj().eigenstates normalizes in L2 norm, we want a L1 normalization
    ss_pops = np.real(eigvecs[kernel_index].full())
    ss_pops = ss_pops / np.sum(ss_pops)
    steadystate = Qobj(np.diag(ss_pops.flatten()))

    return steadystate, np.sort(eigvals[np.isclose(eigvals,
                                                    eigvals[kernel_index])])

```

4.1.3 Running simulations

Finally, here is a simplified version of the `run_single_simulation` function called to compute the steady state for a given set of parameters, outlining the main steps in the steady state computation.

```

def run_single_simulation(n_bar, N_max_a, N_max_b, p,
                        compute_kerr=False,
                        out_directory=None, prefix=''):
    """
    :param n_bar: Mean number of photons at  $\omega_p$  in the pump.
    :param N_max_a: Truncation of the cavity Fock space.

```

```

:param N_max_b: Truncation of the transmon eigenstates space.
:param p: Dictionary of parameters to use.
:param compute_kerr: Whether Kerr should be computed from hamiltonian or
    not.
:param out_directory: Directory where to output files.
:param prefix: A prefix to prepend to output files.
:return: Dumped data.
"""
# 1. Build the Hamiltonian
T = 2 * np.pi / p['omega_p']
N_max_charge = p.get('N_max_charge', 100)
H, args, c_ops, computed_H_params = operators.build_hamiltonian(
    N_max_a, N_max_b, n_bar, p,
    LOGGER, out_directory,
    N_max_charge=N_max_charge,
    compute_kerr=compute_kerr
)

# 2. Compute Floquet modes at t=0
# Manually compute the propagator at t=T.
# This is required to ensure convergence.
propagator_steps = np.linspace(
    0,
    T,
    p.get('propagator_steps', 10)
)
U = qutip.propagator(H, propagator_steps, [], args)[-1]
# t=0 Floquet modes
f_modes_0, f_energies = floquet.floquet_modes(H, T, args, sort=True, U=U)

# 3. Compute the decomposition of initial state on Floquet modes
psi_0 = (H[0] + H[1][0]).groundstate()[1] # Real ground state
# Find its decomposition on Floquet modes at t = 0
f_coeff = floquet.floquet_state_decomposition(f_modes_0, f_energies, psi_0)

# 4. Compute the rate matrices entering the Floquet-Markov master equation
_, X, _, Amat = floquet.floquet_master_equation_rates(
    f_modes_0, f_energies, c_ops[0], H, T, args,
    J_cb=lambda w: 0.5 * p['gamma'] / T,
    w_th=0, kmax=5, f_modes_table_t=None, nT=100)

# 5. Compute the steady state of the system
steadystate, steadystate_eigvals = (
    # Safety is false as we handle the checks manually below
    floquet.floquet_master_equation_steadystate(Amat, safety=False)
)

# 6. Dump all the results into the output directory

```

In practice, when generating the data required for the figures from Chapters 2 and 3, this `run_single_simulation` function is called 8 times in parallel, each with a different set of parameters, to speed up the computation.

4.2 Analysis code

4.2.1 Resonant frequencies of the system

From the steady state found through the Floquet-Markov simulations, one can compute the expected transition frequencies of the system, as detailed in section 2.3.1. This consists in

- First, finding the Floquet modes with a non-negligible population in the steady state, done with the loop on `f_mode_overlap` in the code below,
- Then, finding the Floquet modes which have a non-zero coupling to the previously found ones through the coupling operator, as computed in `X_overlaps` below.
- Finally, the frequency can be computed from the difference of their quasi-energies. The transition probability, as detailed in section 2.3.1 is proportional to their coupling strength.

Note that while I have considered Floquet modes only from the first Brillouin zone in this manuscript so far, I should take into account transitions between two different bands of Floquet modes here. I can however restricts the number of bands to consider to a limited range of values (from -2 to 2, with the zero index being the first Brillouin zone) as considering other bands will only result in having extra transition frequencies much larger than the pump frequency and out of the domain of interest (close to the initial oscillator frequency, in order to compute the ac Stark shifted frequency). These correspond to high order transitions requiring many pump photons.

```
def find_frequencies_from_overlaps(n_bar, data, overlaps_threshold):
    """
    :param n_bar: Mean number of photons in the pump, at  $\omega_p$ .
    :param data: Data loaded from the steady state dump.
    :param overlap_threshold: Threshold for considering Floquet modes.
    """
    frequencies = []
    # Number of computed bands
    n_k_values = int((len(data['X'][0, 0, :]) - 1) / 2)

    for i, f_mode_overlap in enumerate(data['steadystate'].diag()):
        # First, look at Floquet modes in the steadystate with enough
        # weight
        if f_mode_overlap < overlaps_threshold:
            continue

        # Then look at coupled elements through X tensor, in neighbor bands
        # We only consider the k = -2, -1, 0, 1, 2 bands
        k_range = list(range(n_k_values - 2, n_k_values + 3))
        for k in k_range:
            k_value = -n_k_values + k # This is the real value, > 0 or < 0

            X_overlaps = abs(data['X'][i, :, k])
            for j, X_overlap in enumerate(X_overlaps):
                # Look for a coupled enough Floquet mode in this band
                if X_overlap < overlaps_threshold:
                    continue

            # Compute frequency
            frequencies.append({
                "n_bar": n_bar,
```

```

        "frequency": -1.0 * (
            data['f_energies'][i] - data['f_energies'][j] +
            k_value * data['params']['omega_p']
        ) / (2.0 * np.pi),
        "area": np.pi * 7.0**2 * (
            np.sqrt(f_mode_overlap) * X_overlap
        )**2
    })
return frequencies

```

4.2.2 Induced Kerr strength

A similar analysis can be performed in order to compute the Kerr strength from section 3.2. The induced Kerr strength can be found using a cascading scheme of the method used to compute the ac Stark shifted frequencies of the system in section 4.2.1.

Indeed, starting from the computed steady state from the Floquet-Markov framework, it is possible to find the transition between Floquet modes resulting having the largest probability, using the method from section 4.2.1. Then, starting from this pair of Floquet modes and using the same method, one can find the most likely second transition. The induced Kerr strength can then be computed as the difference between the two transition frequencies found.

```

def find_kerr_from_overlaps(n_bar, data, overlaps_threshold):
    """
    :param n_bar: Mean number of photons in the pump, at  $\omega_p$ .
    :param data: Data loaded from the steady state dump.
    :param overlap_threshold: Threshold for considering Floquet modes.
    """
    kerr = []
    # Number of computed bands
    n_k_values = int((len(data['X'][0, 0, :]) - 1) / 2)

    # First, compute the most likely transition from the steady state to another Floquet mode
    max_overlap_idx1 = np.argmax(data['steadystate'].diag())
    max_overlap_idx2, max_overlap_2 = None, None
    k_value_1 = None
    for i, f_mode_overlap in enumerate(data['steadystate'].diag()):
        # First, look at Floquet modes in the steadystate with enough
        # weight
        if f_mode_overlap < overlaps_threshold: continue
        # Then look at coupled elements through X tensor, in neighbor bands
        # We only consider the k = -2, -1, 0, 1, 2 bands
        k_range = list(range(n_k_values - 2, n_k_values + 3))
        for k in k_range:
            k_value = -n_k_values + k # This is the real value, > 0 or < 0
            X_overlaps = abs(data['X'][i, :, k])
            for j, X_overlap in enumerate(X_overlaps):
                # Look for a coupled enough Floquet mode in this band
                if X_overlap < overlaps_threshold: continue
                if max_overlap_idx2 is None or X_overlap > max_overlap_2:
                    max_overlap_2 = X_overlap
                    max_overlap_idx2 = j
                    k_value_1 = k_value

    # From this Floquet mode, look for the most likely second transition
    max_k, max_k_overlap = None, None
    for k in range(len(data['X'][0, 0, :])):
        X2_overlaps = abs(data['X'][max_overlap_idx2, :, k])

```

```

max_overlap_tmp = np.max(X2_overlaps)
if max_k is None or max_overlap_tmp > max_k_overlap:
    max_k = k
    max_k_overlap = max_overlap_tmp

max_k_value = -n_k_values + max_k
X2_overlaps = abs(data['X'][max_overlap_idx2, :, max_k])

# The Kerr strength is given by the difference of the two transition frequencies
kerr.append(1e6 * (
    (-1.0 * (
        data['f_energies'][max_overlap_idx1] -
        data['f_energies'][max_overlap_idx2] +
        k_value_1 * omega_p
    ) / (2.0 * np.pi)) -
    (-1.0 * (
        data['f_energies'][max_overlap_idx2] -
        data['f_energies'][np.argmax(X2_overlaps)] +
        max_k_value * omega_p
    ) / (2.0 * np.pi))
)) # In kHz

```

Finally, the induced Kerr strength computed from the time averaged model and shown in Fig. 3.5 was computed numerically by diagonalizing the time averaged Hamiltonian and looking at the transition frequencies. The induced Kerr strength is given by the difference of the second and first oscillator-like transition frequencies in this Hamiltonian, as computed by

```

def _bessel(n_bar, data):
    epsilon_p = operators.compute_epsilon_p(n_bar, data['params'])
    H_shunted, args, _, _ = operators.build_shunted_hamiltonian(
        data['N_max_a'], data['N_max_b'], epsilon_p, data['params']
    )
    # Compute the time-averaged hamiltonian
    H = (
        H_shunted[0] +
        scipy.special.jv(0, args['oscillating_prefactor']) * H_shunted[1][0]
    )
    # Kerr can be computed through the eigenstates
    eigval, eigvec = H.eigenstates()

    # Compute Kerr from time averaged model
    return (
        -1.0 * (eigval[5] - 2 * eigval[2] + eigval[0]) / (2 * np.pi) * 1e6
    ) # In kHz

```


Chapter 5

Asymmetric Josephson Ring Modulator

Contents

5.1 Josephson Ring Modulator	70
5.1.1 Unshunted Josephson Ring Modulator	70
5.1.2 Josephson Ring Modulator with shunt inductances	72
5.2 Asymmetric Josephson Ring Modulator	75
5.2.1 Circuit Hamiltonian	75
5.2.2 Quantization of the AJRM circuit embedded in a microwave cavity	77
5.3 AJRM for the two-photon and four-photon pumping schemes	80

The previous analysis from Chapters 2-3 illustrates that one should carefully choose the building blocks to implement parametric engineering techniques. For instance, as demonstrated in Chapter 3, the presence of an extra harmonic confinement on a transmon device makes it more stable and the non-linearity is then fully exploitable.

In this Chapter, I will focus on circuits based on the Josephson Ring Modulator [24, 77, 25, 26], a circuit currently used for amplification and frequency conversion, which also features shunt inductances. In particular, I will study a slight variant of this circuit with asymmetric loops and its potential interest for implementing two-photon and four-photon pumping schemes required for the cat-states encoding scheme. This circuit should offer an interesting (physical) protection from harmful terms coming from the expansion of the non-linearity.

I will first recall the main results for the Josephson Ring Modulator, as currently used for amplification and frequency conversion. I will then present the asymmetric version of this circuit and how it helps removing potentially harmful terms. Finally, I will comment on the maximum achievable interaction strengths for two-photon and four-photon exchange processes using this device.

5.1 Josephson Ring Modulator

First, I will briefly recall previously existing results about the Josephson Ring Modulator (JRM) and its extension with shunt inductances, as presented in [24, 77, 25, 26].

5.1.1 Unshunted Josephson Ring Modulator

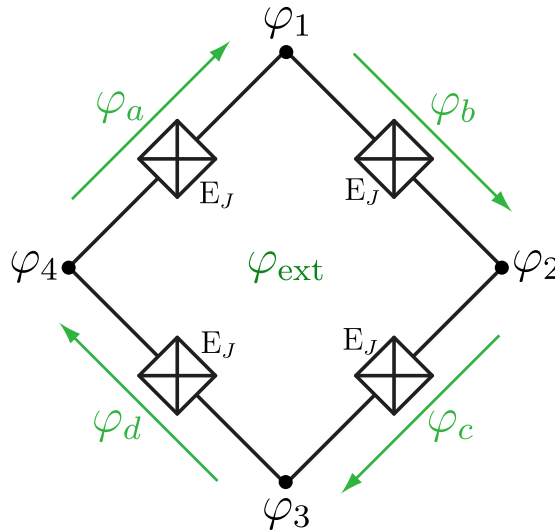


Figure 5.1: **Electric circuit for the unshunted Josephson Ring Modulator.** The JRM consists of a single loop of four Josephson junctions with the same Josephson energy E_J and capacitive energy E_C , all in series. An external reduced magnetic flux φ_{ext} is threading the loop. We denote by $\{\varphi_\mu\}_{\mu=a,b,c,d}$ the flux across each of these junctions and $\{\varphi_k\}_{k=1,2,3,4}$ the node fluxes at each vertex of the loop.

The unshunted Josephson Ring Modulator circuit is shown in Fig. 5.1. Its Hamilto-

nian reads

$$H = \frac{E_C}{2} (Q_a^2 + Q_b^2 + Q_c^2 + Q_d^2) - E_J (\cos \varphi_a + \cos \varphi_b + \cos \varphi_c + \cos \varphi_d) \quad (5.1)$$

where

$$\begin{cases} \varphi_a = \varphi_1 - \varphi_4 + \frac{\varphi_{\text{ext}}}{4} + n\frac{\pi}{2} \\ \varphi_b = \varphi_2 - \varphi_1 + \frac{\varphi_{\text{ext}}}{4} + n\frac{\pi}{2} \\ \varphi_c = \varphi_3 - \varphi_2 + \frac{\varphi_{\text{ext}}}{4} + n\frac{\pi}{2} \\ \varphi_d = \varphi_4 - \varphi_3 + \frac{\varphi_{\text{ext}}}{4} + n\frac{\pi}{2} \end{cases} \quad (5.2)$$

with φ_{ext} the external reduced magnetic flux threading the loop and n an integer and where $\{Q_\mu\}_{\mu=a,b,c,d}$ are the charge variables for each Josephson junction, defined as the conjugate variables of the $\{\varphi_\mu\}_{\mu=a,b,c,d}$.

Moreover, from the Kirchhoff's voltage law, one gets

$$\varphi_a + \varphi_b + \varphi_c + \varphi_d = \varphi_{\text{ext}} [2\pi] \quad (5.3)$$

Let us now introduce *normal modes* of the system, $\{\varphi_\nu\}_{\nu=X,Y,Z,M}$, such that the quadratic part of the Hamiltonian Eq. (5.1) reads $\varphi^T \mathcal{L} \varphi$ with \mathcal{L} a diagonal inductance matrix and $\varphi^T = (\varphi_X, \varphi_Y, \varphi_Z, \varphi_M)$. First, let us expand the Josephson part of Hamiltonian Eq. (5.1) to second order in $\{\varphi_\mu\}_{\mu=a,b,c,d}$,

$$\frac{E_J}{2} (\varphi_a^2 + \varphi_b^2 + \varphi_c^2 + \varphi_d^2) = \frac{E_J}{2} \begin{pmatrix} \varphi_1 \\ \varphi_2 \\ \varphi_3 \\ \varphi_4 \end{pmatrix}^T \underbrace{\begin{pmatrix} 2 & -1 & 0 & -1 \\ -1 & 2 & -1 & 0 \\ 0 & -1 & 2 & -1 \\ -1 & 0 & -1 & 2 \end{pmatrix}}_{\mathcal{L}} \begin{pmatrix} \varphi_1 \\ \varphi_2 \\ \varphi_3 \\ \varphi_4 \end{pmatrix} \quad (5.4)$$

By diagonalizing \mathcal{L} , one finds the normal modes of the system, defined as

$$\begin{pmatrix} \varphi_X \\ \varphi_Y \\ \varphi_Z \\ \varphi_W \end{pmatrix} = \begin{pmatrix} 0 & 1 & 0 & -1 \\ 1 & 0 & -1 & 0 \\ -1/2 & 1/2 & -1/2 & 1/2 \\ 1/2 & 1/2 & 1/2 & 1/2 \end{pmatrix} \begin{pmatrix} \varphi_1 \\ \varphi_2 \\ \varphi_3 \\ \varphi_4 \end{pmatrix}. \quad (5.5)$$

At this point, one can notice that the eigenvalue in \mathcal{L} associated with φ_W is zero. Therefore, this mode is uncoupled from the system. The normal modes are represented in Fig. 5.2

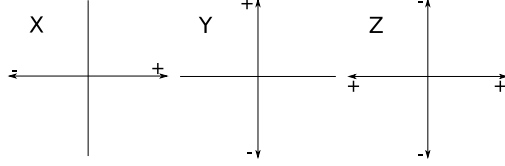


Figure 5.2: **Normal modes of the Josephson Ring Modulator.** The Josephson Ring Modulator is coupled to three orthogonal microwave modes: X and Y are differential modes in horizontal and vertical direction whereas Z is a common mode. The last normal mode, W is not represented here as the corresponding eigenvalue in the inductance matrix is zero.

In the normal modes basis, the Hamiltonian Eq. (5.1) reads

$$\begin{aligned}
 H = & \frac{E_C}{2} \left(Q_X^2 + Q_Y^2 + 4Q_Z^2 \right) \\
 & - 4E_J \left[\cos \frac{\varphi_X}{2} \cos \frac{\varphi_Y}{2} \cos \varphi_Z \cos \left(\frac{\varphi_{\text{ext}} + 2n\pi}{4} \right) \right. \\
 & \left. + \sin \frac{\varphi_X}{2} \sin \frac{\varphi_Y}{2} \sin \varphi_Z \sin \left(\frac{\varphi_{\text{ext}} + 2n\pi}{4} \right) \right]
 \end{aligned} \tag{5.6}$$

where $\{Q_\nu\}_{\nu=X,Y,Z,M}$ are the conjugate variables of $\{\varphi_\nu\}_{\nu=X,Y,Z,M}$.

Expanding the Hamiltonian from Eq. (5.6) around the point of equilibrium $\varphi_X = \varphi_Y = \varphi_Z = 0$ up to the third order in phase variables, one gets

$$\begin{aligned}
 H_{\text{linear}} = & \frac{E_C}{2} \left(Q_X^2 + Q_Y^2 + 4Q_Z^2 \right) \\
 & + \frac{E_J}{2} \cos \left(\frac{\varphi_{\text{ext}} + 2n\pi}{4} \right) \left(\varphi_X^2 + \varphi_Y^2 + 4\varphi_Z^2 \right) \\
 & - E_J \sin \left(\frac{\varphi_{\text{ext}} + 2n\pi}{4} \right) \varphi_X \varphi_Y \varphi_Z \\
 & - 4E_J \cos \left(\frac{\varphi_{\text{ext}} + 2n\pi}{4} \right).
 \end{aligned} \tag{5.7}$$

A three wave mixing term, $\varphi_X \varphi_Y \varphi_Z$ appears in Eq. (5.7), whose amplitude depends on the external flux threading the loop of the JRM, φ_{ext} . This is the term of interest for performing amplification or conversion with this device, using one mode as a *signal*, one mode as an *idler* and the third mode as a *pump* to satisfy a frequency matching condition. The maximum amplitude for the three wave mixing term is reached for an external reduced magnetic flux $\varphi_{\text{ext}} = 2\pi$. However, this configuration is unstable, as pictured on Fig. 5.3. This instability, however, is a different sort of instability than the one presented in Chapter 2.

5.1.2 Josephson Ring Modulator with shunt inductances

In order to overcome the instability of the unshunted Josephson Ring Modulator around the best point of operation for achieving three wave mixing, extra shunt inductances can be added to the Josephson ring as depicted in Fig. 5.4.

The same solution also provides a stability in the sense of Chapters 2-3. Such a system can therefore be investigated using standard time averaging techniques (rotating wave approximations).

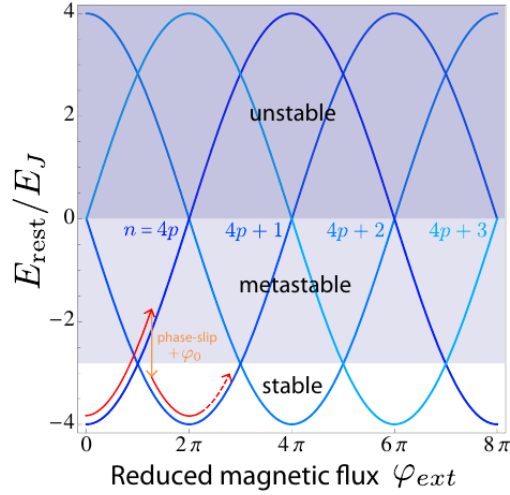


Figure 5.3: **Illustration of the instability of the unshunted Josephson Ring Modulator around the optimal point of operation.** The Kirchhoff's voltage law Eq. (5.3) gives a relation between the phases defined up to a 2π factor. Each configuration (defined by a unique set of values for $(\varphi_a, \varphi_b, \varphi_c, \varphi_d)$) is then 8π -periodic. However, the lowest energy level from the Hamiltonian Eq. (5.6), E_{rest} , depends on the value of the 2π multiple, that is, on n . Indeed, if the system starts from a branch where $n = 4p$ with p an integer and an external magnetic flux $\varphi_{\text{ext}} = 0$ and if this external magnetic flux increases to π , then the $n = 4p$ branch becomes metastable and it is the $n = 4p + 1$ branch which is the most stable. The system then undergoes a phase flip towards this configuration, preventing us from reaching the optimal point of operations $\varphi_{\text{ext}} = 2\pi$. The best compromise is then around $\varphi_{\text{ext}} = \pi$. This figure is borrowed from [26].

In this section, I will briefly recall the main results and computation of the Hamiltonian of this system, which serves as a basis for the Asymmetric Josephson Ring modulator presented in section 5.2. This subsection is following the computations and notations from [26]. I will use the central node as the reference for the potential.

The Hamiltonian of the circuit in Fig. 5.4 reads

$$\begin{aligned}
 H = & \frac{E_C}{2} (Q_a^2 + Q_b^2 + Q_c^2 + Q_d^2) \\
 & - E_J (\cos \varphi_a + \cos \varphi_b + \cos \varphi_c + \cos \varphi_d) \\
 & + \frac{E_L}{2} (\varphi_{L_1}^2 + \varphi_{L_2}^2 + \varphi_{L_3}^2 + \varphi_{L_4}^2).
 \end{aligned} \tag{5.8}$$

There are now four different relations given by Kirchhoff's voltage law, which are

$$\left\{ \begin{array}{l}
 \varphi_a - \varphi_{L_1} + \varphi_{L_4} = \frac{\varphi_{\text{ext}}}{4} + 2\pi n_a \\
 \varphi_b - \varphi_{L_2} + \varphi_{L_1} = \frac{\varphi_{\text{ext}}}{4} + 2\pi n_b \\
 \varphi_c - \varphi_{L_3} + \varphi_{L_2} = \frac{\varphi_{\text{ext}}}{4} + 2\pi n_c \\
 \varphi_d - \varphi_{L_4} + \varphi_{L_3} = \frac{\varphi_{\text{ext}}}{4} + 2\pi n_d
 \end{array} \right. \tag{5.9}$$

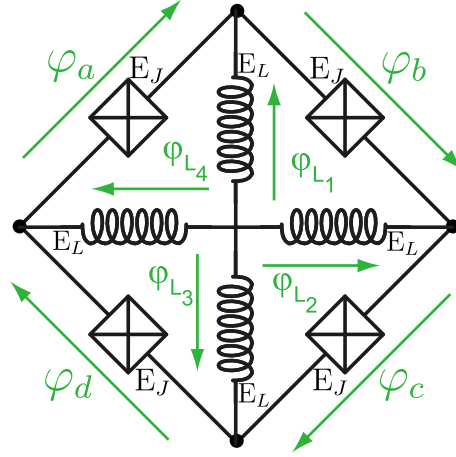


Figure 5.4: **Electric circuit for the inductively shunted Josephson Ring Modulator.** This JRM consists of a single loop of four Josephson junctions with the same Josephson energy E_J and capacitive energy E_C , all in series. Four inductances with the same inductive energy E_L are splitting the loop into four triangles of same areas. We denote by $\{\varphi_\mu\}_{\mu=a,b,c,d}$ the flux across each of these junctions and $\{\varphi_{L_k}\}_{k=1,2,3,4}$ the flux across each of the shunting inductance.

where φ_{ext} is the total external reduced magnetic flux threading the largest loop and n_a , n_b , n_c and n_d are integers.

Additionally, the charge conservation written at the central node gives

$$(\varphi_{L_1} + \varphi_{L_2} + \varphi_{L_3} + \varphi_{L_4}) = 0 \quad (5.10)$$

Using the normal modes from Eq. (5.5) as well as the relation from Eq. (5.10),

$$\left\{ \begin{array}{l} 4\varphi_{L_1} = 2(\varphi_Y - \varphi_Z) \\ 4\varphi_{L_2} = 2(\varphi_X + \varphi_Z) \\ 4\varphi_{L_3} = -2(\varphi_Y + \varphi_Z) \\ 4\varphi_{L_4} = -2(\varphi_X - \varphi_Z) \end{array} \right. \quad (5.11)$$

Contrary to the base case from section 5.1.1, all of the fluxes $\{\varphi_\mu\}_{\mu=a,b,c,d}$ are now 2π -periodic. Using the same set of modes as in Eq. (5.5) (and shown on Fig. 5.2),

replacing the φ_k by φ_{L_k} , the Hamiltonian of the system reads

$$\begin{aligned}
H = & \frac{E_C}{2} (Q_X^2 + Q_Y^2 + 4Q_Z^2) \\
& + \frac{E_L}{2} \left(\frac{\varphi_X^2}{2} + \frac{\varphi_Y^2}{2} + \varphi_Z^2 \right) \\
& - 4E_J \left[\cos \frac{\varphi_X}{2} \cos \frac{\varphi_Y}{2} \cos \varphi_Z \cos \left(\frac{\varphi_{\text{ext}} + 2n\pi}{4} \right) \right. \\
& \quad \left. + \sin \frac{\varphi_X}{2} \sin \frac{\varphi_Y}{2} \sin \varphi_Z \sin \left(\frac{\varphi_{\text{ext}} + 2n\pi}{4} \right) \right]
\end{aligned} \tag{5.12}$$

This Hamiltonian can also provide a three wave mixing term, similarly to the one from Eq. (5.6). However, contrary to this previous case, all flux configurations are now stable, allowing to reach the optimal point of operation to maximize this three wave mixing term.

When expanding Hamiltonian (5.12) to higher order, extra Kerr-type terms coming from the terms φ_X^4 , φ_Y^4 and φ_Z^4 should be taken into account. These terms are resonant in rotating wave approximations [19] and detrimental to the operation of the system.

5.2 Asymmetric Josephson Ring Modulator

The inner inductive loops of the Josephson Ring Modulator circuit provided extra stability to the system, while maintaining the main features in the Hamiltonian useful for parametric amplification or conversion. Building on this circuit which provides a pure three-wave mixing term, let us introduce an asymmetric version (the Asymmetric Josephson Ring Modulator), as pictured in Fig. 5.5. This asymmetric version provides a pure higher-order mixing terms, in which two modes appear with odd powers only and the third mode appear with both odd and even powers. Such a pure higher-order mixing term can be used to efficiently implement two-photon and four-photon exchange Hamiltonians.

Indeed, in order to implement the cat-state pumping scheme presented in section 1.5, the circuit should implement a term of the form $\mathbf{bc}^d + \text{h.c.}$ with $d = 2$ (for two-photon scheme) or $d = 4$ (for four-photon scheme), with \mathbf{b} and \mathbf{c} the annihilation operators of two different modes. Josephson junction circuits provide cosine and sine potential. Therefore, a term of the form $\sin(\mathbf{a} + \mathbf{a}^\dagger) \sin(\mathbf{b} + \mathbf{b}^\dagger) \cos(\mathbf{c} + \mathbf{c}^\dagger)$ where \mathbf{a} is the annihilation operator of a third mode coupled to a pump, would implement the required Hamiltonian interaction with a carefully chosen frequency matching condition.

5.2.1 Circuit Hamiltonian

Let us focus on the circuit pictured in Fig. 5.5, presenting a shunted Josephson Ring Modulator with areas in a ratio λ . The base Hamiltonian in the basis of the phases across each junction still reads

$$\begin{aligned}
H = & \frac{E_C}{2} (Q_a^2 + Q_b^2 + Q_c^2 + Q_d^2) \\
& - E_J (\cos \varphi_a + \cos \varphi_b + \cos \varphi_c + \cos \varphi_d) \\
& + \frac{E_L}{2} (\varphi_{L_1}^2 + \varphi_{L_2}^2 + \varphi_{L_3}^2 + \varphi_{L_4}^2).
\end{aligned} \tag{5.13}$$

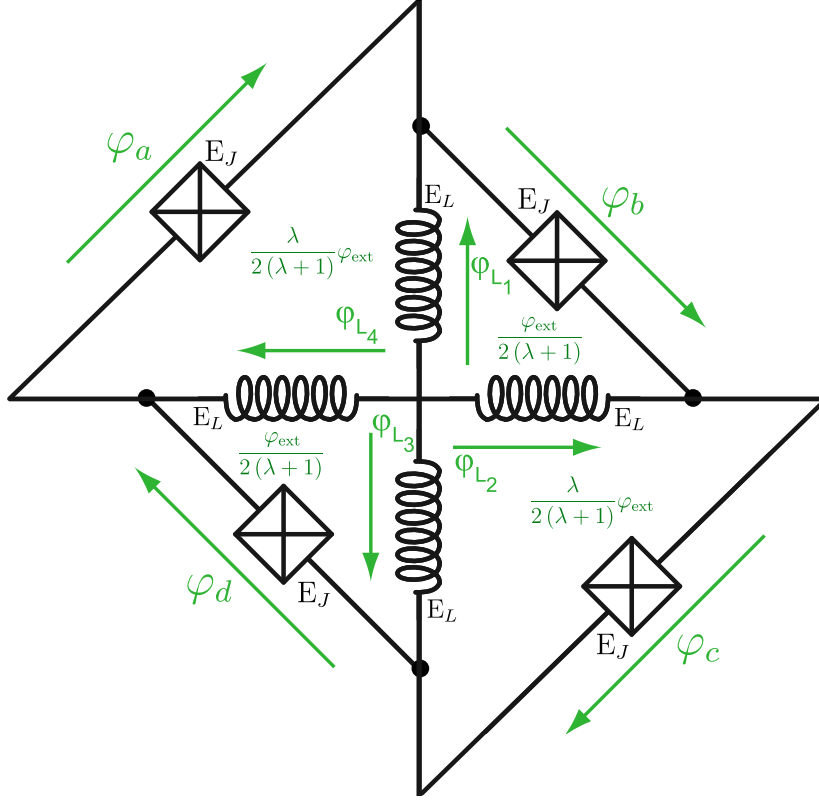


Figure 5.5: **Electric circuit for the Asymmetric Josephson Ring Modulator.** This circuit is the same as the Josephson Ring Modulator with shunt inductances circuit from Fig. 5.4 except that the inner loops now have different areas, in a ratio λ .

The four different relations given by Kirchhoff's voltage law are

$$\left\{ \begin{array}{l} \varphi_a - \varphi_{L_1} + \varphi_{L_4} = \frac{\lambda}{2(\lambda+1)}\varphi_{\text{ext}} + 2\pi n_a \\ \varphi_b - \varphi_{L_2} + \varphi_{L_1} = \frac{1}{2(\lambda+1)}\varphi_{\text{ext}} + 2\pi n_b \\ \varphi_c - \varphi_{L_3} + \varphi_{L_2} = \frac{\lambda}{2(\lambda+1)}\varphi_{\text{ext}} + 2\pi n_c \\ \varphi_d - \varphi_{L_4} + \varphi_{L_3} = \frac{1}{2(\lambda+1)}\varphi_{\text{ext}} + 2\pi n_d \end{array} \right. \quad (5.14)$$

where φ_{ext} is the total external reduced magnetic flux threading the outermost loop, λ is the ratio of areas of the inner loops and n_a , n_b , n_c and n_d are integers.

Additionally, the charge conservation written at the central node gives

$$(\varphi_{L_1} + \varphi_{L_2} + \varphi_{L_3} + \varphi_{L_4}) = 0 \quad (5.15)$$

From Eq. (5.14) and Eq. (5.11),

$$\left\{ \begin{array}{l} \varphi_a = \frac{\lambda}{2(\lambda+1)}\varphi_{\text{ext}} + 2\pi n_a + \frac{\varphi_X + \varphi_Y - 2\varphi_Z}{2} \\ \varphi_b = \frac{1}{2(\lambda+1)}\varphi_{\text{ext}} + 2\pi n_b + \frac{\varphi_X - \varphi_Y + 2\varphi_Z}{2} \\ \varphi_c = \frac{\lambda}{2(\lambda+1)}\varphi_{\text{ext}} + 2\pi n_c - \frac{\varphi_X + \varphi_Y + 2\varphi_Z}{2} \\ \varphi_d = \frac{1}{2(\lambda+1)}\varphi_{\text{ext}} + 2\pi n_d - \frac{\varphi_X - \varphi_Y - 2\varphi_Z}{2} \end{array} \right. \quad (5.16)$$

Finally, when imposing $\varphi_{\text{ext}} = 2\pi$ and rewriting this Hamiltonian in the normal modes basis Eq. (5.5) written built from the φ_{L_k} instead of the φ_k , it is now given by

$$\begin{aligned} H = & \frac{E_C}{2} (Q_X^2 + Q_Y^2 + 4Q_Z^2) \\ & + \frac{E_L}{2} \left(\frac{\varphi_X^2}{2} + \frac{\varphi_Y^2}{2} + \varphi_Z^2 \right) \\ & - 4E_J \sin\left(\frac{\varphi_X}{2}\right) \sin\left(\frac{\varphi_Y}{2}\right) \left[\sin\left(\frac{(\lambda-1)\pi}{2(\lambda+1)}\right) \cos(\varphi_Z) \right. \\ & \quad \left. - \cos\left(\frac{(\lambda-1)\pi}{2(\lambda+1)}\right) \sin(\varphi_Z) \right] \end{aligned} \quad (5.17)$$

The Hamiltonian Eq. (5.17) now only contains terms with odd powers in φ_X and φ_Y coming from the Josephson potential and a mix of odd and even powers of φ_Z depending on the ratio λ . The fact that no even powers of φ_X and φ_Y enter this expression implies that in rotating wave approximations [19], resonant parasitic terms involving these modes will not exist. The asymmetry here helps preserving terms such as $\varphi_X \varphi_Y \varphi_Z^2$ which will be useful for implementing the two photons or four photons pumping scheme (see section 5.2.2) while avoiding Kerr-type terms on both X , Y and Z modes. This cancellation of extra parasitic terms however comes at the expense of operating at a fixed external flux value, $\varphi_{\text{ext}} = 2\pi$, whereas the external flux was another control parameter available to engineer the strength of the interactions in the Josephson Ring Modulator circuit. One can also note that by changing the layout of the large and small inner loops, one can rotate which modes appear in a sine term only and which mode has both a cosine and a sine term.

5.2.2 Quantization of the AJRM circuit embedded in a microwave cavity

In this section, I will focus on using an Asymmetric Josephson Ring Modulator circuit embedded into half-wavelength resonators to couple it with microwave modes in a cavity. This circuit is represented in Fig. 5.6. I will assume a specific ratio between the areas of the larger and smaller loops, $\lambda = 3$.

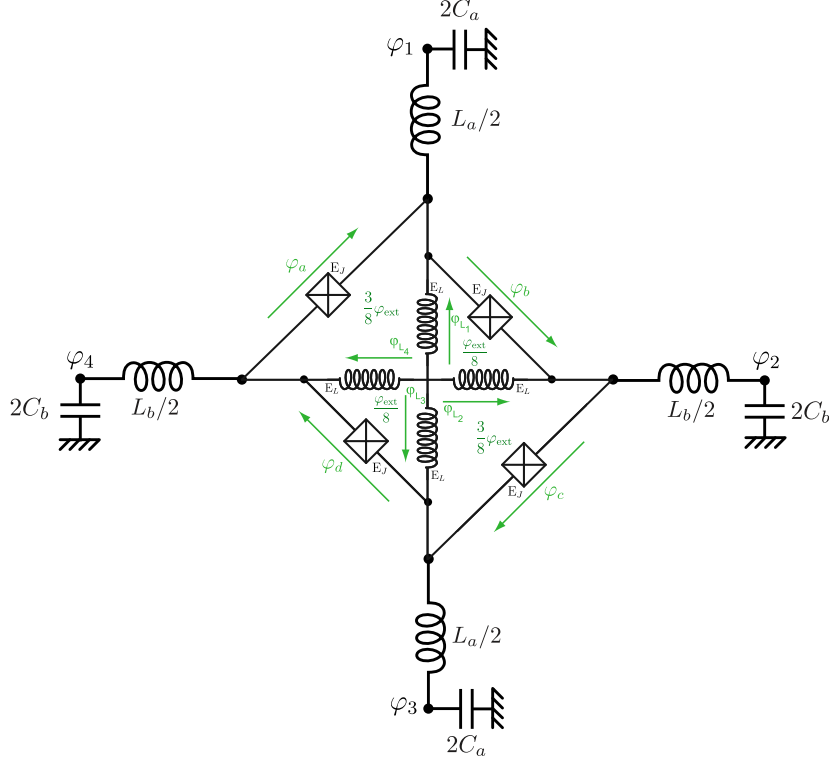


Figure 5.6: **Electric circuit for the Asymmetric Josephson Ring Modulator embedded into $\lambda/2$ resonators.** The AJRM circuit from section 5.2 is embedded here into $\lambda/2$ resonators to couple it with microwave modes of a 3D cavity. I am here considering a particular $\lambda = 3$ ratio between the areas of the inner loops, resulting in a perceived magnetic flux $3\varphi_{\text{ext}}/8$ in the larger loops and $\varphi_{\text{ext}}/8$ in the smaller loops.

Let us define new modes for the inner ring, similarly to the ones from Eq. (5.5),

$$\left\{ \begin{array}{l} \varphi_X = \varphi_{L_2} - \varphi_{L_4} \\ \varphi_Y = \varphi_{L_1} - \varphi_{L_3} \\ \varphi_Z = \frac{1}{2} (\varphi_{L_2} + \varphi_{L_4} - \varphi_{L_1} - \varphi_{L_3}) \end{array} \right. \quad (5.18)$$

and the same kind of modes based on the $\{\varphi_k\}_{k=1,2,3,4}$ node fluxes in each antenna,

$$\left\{ \begin{array}{l} \varphi_{\tilde{X}} = \varphi_2 - \varphi_4 \\ \varphi_{\tilde{Y}} = \varphi_1 - \varphi_3 \\ \varphi_{\tilde{Z}} = \frac{1}{2} (\varphi_2 + \varphi_4 - \varphi_1 - \varphi_3) \end{array} \right. \quad (5.19)$$

These two sets of modes can easily be related by defining the *participation factors*

as the ratios between the external node fluxes and the AJRM vertex fluxes, as

$$\begin{aligned}\xi_X &= \varphi_X / \varphi_{\tilde{X}} = L_X^{\text{AJRM}} / L_X^{\text{tot}}, \\ \xi_Y &= \varphi_Y / \varphi_{\tilde{Y}} = L_Y^{\text{AJRM}} / L_Y^{\text{tot}}, \\ \xi_Z &= \varphi_Z / \varphi_{\tilde{Z}} = L_Z^{\text{AJRM}} / L_Z^{\text{tot}}.\end{aligned}\tag{5.20}$$

where we introduced the inductance and capacitance of each mode, sum of the AJRM contribution and the antenna contributions, defined as

$$\begin{aligned}L_X^{\text{AJRM}} &= 2 \frac{\varphi_0^2}{E_L}, & L_X^{\text{tot}} &= L_a + L_X^{\text{AJRM}}, & C_X^{\text{tot}} &= C_a \\ L_Y^{\text{AJRM}} &= 2 \frac{\varphi_0^2}{E_L}, & L_Y^{\text{tot}} &= L_b + L_Y^{\text{AJRM}}, & C_Y^{\text{tot}} &= C_b \\ L_Z^{\text{AJRM}} &= \frac{\varphi_0^2}{E_L}, & L_Z^{\text{tot}} &= \frac{L_a + L_b}{4} + L_Z^{\text{AJRM}}, & C_Z^{\text{tot}} &= \frac{4C_a C_b}{C_a + C_b}\end{aligned}\tag{5.21}$$

with $\varphi_0 = (\hbar/2e)$ the magnetic flux quantum. Note that in order to write Eq. (5.21), I neglected the contributions of the Josephson junctions capacitive energy compared to the capacitances of the antennas. These participation ratios represent the fraction of the mode energy contained in the AJRM.

Imposing $\varphi_{\text{ext}} = 2\pi$ as in section 5.2, the full Hamiltonian of the circuit shown in Fig. 5.6 is then given by

$$\begin{aligned}H &= \frac{\varphi_0^2}{2L_X^{\text{tot}}} \varphi_{\tilde{X}}^2 + \frac{1}{2C_X^{\text{tot}}} Q_{\tilde{X}}^2 \\ &+ \frac{\varphi_0^2}{2L_Y^{\text{tot}}} \varphi_{\tilde{Y}}^2 + \frac{1}{2C_Y^{\text{tot}}} Q_{\tilde{Y}}^2 \\ &+ \frac{\varphi_0^2}{2L_Z^{\text{tot}}} \varphi_{\tilde{Z}}^2 + \frac{1}{2C_Z^{\text{tot}}} Q_{\tilde{Z}}^2 \\ &- 2\sqrt{2}E_J \sin\left(\frac{\varphi_X}{2}\right) \sin\left(\frac{\varphi_Y}{2}\right) [\cos(\varphi_Z) - \sin(\varphi_Z)].\end{aligned}\tag{5.22}$$

Following the approach from [14, 17], photon annihilation and creation operators can be introduced for each mode in order to quantize them, leading to

$$\begin{cases} \varphi_{\tilde{X}} = \varphi_{\tilde{X}}^0 (\mathbf{a} + \mathbf{a}^\dagger) \\ \varphi_{\tilde{Y}} = \varphi_{\tilde{Y}}^0 (\mathbf{b} + \mathbf{b}^\dagger) \\ \varphi_{\tilde{Z}} = \varphi_{\tilde{Z}}^0 (\mathbf{c} + \mathbf{c}^\dagger) \end{cases}\tag{5.23}$$

where

$$\varphi_{\tilde{X}, \tilde{Y}, \tilde{Z}}^0 = \frac{1}{\varphi_0} \sqrt{\frac{\hbar Z_{X,Y,Z}}{2}} \quad \text{with} \quad Z_{X,Y,Z} = \sqrt{\frac{L_{X,Y,Z}^{\text{tot}}}{C_{X,Y,Z}^{\text{tot}}}}.\tag{5.24}$$

From these $\varphi_{\tilde{X}}$, $\varphi_{\tilde{Y}}$, $\varphi_{\tilde{Z}}$ the other required operators can easily be written as

$$\left\{ \begin{array}{l} \mathbf{Q}_{\tilde{X}} = -i\sqrt{\frac{\hbar}{2Z_X}} (\mathbf{a} + \mathbf{a}^\dagger) \\ \mathbf{Q}_{\tilde{Y}} = -i\sqrt{\frac{\hbar}{2Z_Y}} (\mathbf{b} + \mathbf{b}^\dagger) \\ \mathbf{Q}_{\tilde{Z}} = -i\sqrt{\frac{\hbar}{2Z_Z}} (\mathbf{c} + \mathbf{c}^\dagger) \end{array} \right. \quad \text{and} \quad \left\{ \begin{array}{l} \varphi_X = \xi_X \varphi_{\tilde{X}} \\ \varphi_Y = \xi_Y \varphi_{\tilde{Y}} \\ \varphi_Z = \xi_Z \varphi_{\tilde{Z}} \end{array} \right. \quad (5.25)$$

At this point, one might note that, *a priori*, the inductances $L_{X,Y,Z}^{\text{tot}}$ depends on the magnetic flux threading the outermost loop, φ_{ext} . Therefore, the resonance frequencies should also depends on this external flux, as

$$\omega_{X,Y,Z} = \frac{1}{\sqrt{L_{X,Y,Z}^{\text{tot}}(\varphi_{\text{ext}}) C_{X,Y,Z}^{\text{tot}}}}.$$

Although this is true for a general operation of this circuit, I am interested here in the behavior and properties of this circuit when imposing $\varphi_{\text{ext}} = 2\pi$.

5.3 AJRM for the two-photon and four-photon pumping schemes

I will now show how the circuit from Fig. 5.6 with the Hamiltonian from Eq. 5.22 can be used to achieve parametrically a four photons pumping Hamiltonian. Let us consider an extra pump term applied on the X mode. The full Hamiltonian reads

$$\begin{aligned} H = & \hbar\omega_X \mathbf{a}^\dagger \mathbf{a} + \hbar\omega_Y \mathbf{b}^\dagger \mathbf{b} + \hbar\omega_Z \mathbf{c}^\dagger \mathbf{c} \\ & - 2\sqrt{2}E_J \sin\left(\frac{\varphi_{\tilde{X}}^0}{2} (\mathbf{a}^\dagger + \mathbf{a})\right) \sin\left(\frac{\varphi_{\tilde{Y}}^0}{2} (\mathbf{b}^\dagger + \mathbf{b})\right) \cos\left(\varphi_{\tilde{Z}}^0 (\mathbf{c}^\dagger + \mathbf{c})\right) \\ & + 2\sqrt{2}E_J \sin\left(\frac{\varphi_{\tilde{X}}^0}{2} (\mathbf{a}^\dagger + \mathbf{a})\right) \sin\left(\frac{\varphi_{\tilde{Y}}^0}{2} (\mathbf{b}^\dagger + \mathbf{b})\right) \sin\left(\varphi_{\tilde{Z}}^0 (\mathbf{c}^\dagger + \mathbf{c})\right) \\ & + i\mathcal{A}_p(t) (\mathbf{a}^\dagger - \mathbf{a}) \end{aligned} \quad (5.26)$$

where $\mathcal{A}_p(t) = A_p \cos(\omega_p t)$ is the time-dependent amplitude of the pump. In the stiff pump regime, this results in the \mathbf{a} mode being populated by a coherent state $\alpha e^{-i\omega_p t}$ with $\alpha = A_p/2(\omega_p - \omega_a)$. Let us note that, in absence of a pump, the \mathbf{a} and \mathbf{b} modes are not normal modes of the system. Indeed, the lowest order term in the expansion of the first part of the Hamiltonian hybridizes these two modes, therefore changing their frequencies. In a spectroscopy measurement, the frequency of the normal modes will be shifted from ω_X and ω_Y due to this hybridization.

Furthermore, let us assume a frequency matching condition

$$\omega_p + \omega_Y = d\omega_Z \quad (5.27)$$

with $d = 2$ for the two-photon pumping scheme and $d = 4$ for the four-photon pumping scheme. Assuming no other resonance conditions exist between the frequencies ω_p and $\omega_{X,Y,Z}$, one can apply a rotating wave approximation similar to section 1.3. This

rotating-wave approximation is allowed as the inductive shunts ensure the stability of the system in presence of driving pump. Only terms of the form

$$|\alpha|^{2k} (\mathbf{b}^\dagger)^l \mathbf{b}^l (\mathbf{c}^\dagger)^m \mathbf{c}^m \left[\alpha \mathbf{b} (\mathbf{c}^\dagger)^d + \alpha^* \mathbf{b}^\dagger \mathbf{c}^d \right] \quad (5.28)$$

where $k, l, m \in \mathbb{Z}$ should be taken into account in the expansion of the product of cosine and sine term. Indeed, similarly to the Kerr term in Chapter 2, the multi-photon interaction term in this system can be studied under a rotating-wave approximation.

Let us first start by considering the pump mode, represented by its complex amplitude α . Following the approach from section 1.3 (displacement of the pump mode and interaction picture) and the results from chapter 2 (time averaging), the pump contribution to the Hamiltonian can be captured with a time-averaging technique,

$$\overline{\sin\left(\frac{\varphi_{\tilde{X}}^0}{2}(\alpha^* e^{i\omega_p t} + \alpha e^{-i\omega_p t})\right)} / |\alpha| \times (\alpha e^{-i\omega_p t} + \text{h.c.}) = \left[\frac{\varphi_{\tilde{X}}^0}{2} \times e^{-\left(\frac{\varphi_{\tilde{X}}^0}{2}\right)^2/8} \times \frac{J_1\left(\frac{\varphi_{\tilde{X}}^0}{2}|\alpha|\right)}{\left(\frac{\varphi_{\tilde{X}}^0}{2}|\alpha|\right)/2} \right] (\alpha + \text{h.c.}). \quad (5.29)$$

For the two remaining modes, \mathbf{b} and \mathbf{c} , we want to consider terms of the form $(\mathbf{b}^\dagger)^k \mathbf{b}^k \mathbf{b}$ (respectively $(\mathbf{c}^\dagger)^k \mathbf{c}^k \mathbf{c}^d$) or their hermitian conjugate in the expansion of the sine and cosine term from Eq. (5.22).

From the relation

$$(A + B)^n = \sum_{\substack{k=0 \\ n \equiv k \pmod{2}}}^n \left(-\frac{[A, B]}{2} \right)^{\frac{n-k}{2}} \frac{n!}{k!(\frac{n-k}{2})!} \left(\sum_{r=0}^k \binom{k}{r} A^r B^{k-r} \right) \quad (5.30)$$

which gives the Newton binomial expansion of non-commutative terms under the condition that $[A, [A, B]] = [B, [A, B]] = 0$ and can be demonstrated using the Baker-Campbell-Hausdorff lemma, one finds for the \mathbf{b} mode

$$\begin{aligned} \sin\left(\frac{\varphi_{\tilde{Y}}^0}{2} \frac{\mathbf{b} e^{-i\omega_Y t} + \mathbf{b}^\dagger e^{i\omega_Y t}}{2}\right) &= \frac{\varphi_{\tilde{Y}}^0}{2} \sum_{i \geq 0} (-1)^i \left(\frac{\varphi_{\tilde{Y}}^0}{2}\right)^{2i} \frac{(\mathbf{b} e^{-i\omega_Y t} + \mathbf{b}^\dagger e^{i\omega_Y t})^{2i+1}}{(2i+1)!} \\ &= \frac{\varphi_{\tilde{Y}}^0}{2} \sum_{i \geq 0} \left(-\frac{\varphi_{\tilde{Y}}^0}{4}\right)^i \sum_{\substack{k=0 \\ k=1[2]}}^{2i+1} \frac{\left(\frac{[\mathbf{b}, \mathbf{b}^\dagger]}{2}\right)^{\frac{2i+1-k}{2}}}{k! \left(\frac{2i+1-k}{2}\right)!} \sum_{r=0}^k \binom{k}{r} e^{i(2r-k)\omega_Y t} (\mathbf{b}^\dagger)^r \mathbf{b}^{k-r} \end{aligned} \quad (5.31)$$

which yields the following contribution to the total Hamiltonian

$$\left[-\frac{\varphi_{\tilde{Y}}^0}{2} \times e^{-\left(\frac{\varphi_{\tilde{Y}}^0}{2}\right)^2/8} \times \frac{L_{\mathbf{b}^\dagger \mathbf{b} + 1}^{(-1)}\left(\left(\frac{\varphi_{\tilde{Y}}^0}{2}\right)^2/4\right)}{\left(\frac{\varphi_{\tilde{Y}}^0}{2}\right)^2/4} \right] (\mathbf{b} e^{-i\omega_Y t} + \text{h.c.}). \quad (5.32)$$

Conversely, the \mathbf{c} mode yields the contribution

$$\left[-\frac{\left(\frac{\varphi_{\tilde{Z}}^0}{2}\right)^2}{8} \times e^{-\left(\frac{\varphi_{\tilde{Z}}^0}{2}\right)^2/8} \times \frac{L_{\mathbf{c}^\dagger \mathbf{c} + 2}^{(-2)}\left(\left(\frac{\varphi_{\tilde{Z}}^0}{2}\right)^2/4\right)}{\left(\frac{\varphi_{\tilde{Z}}^0}{2}\right)^2/4} \right] (\mathbf{c}^2 e^{-2i\omega_Z t} + \text{h.c.}) \quad (5.33)$$

for the two-photon pumping interaction and

$$\left[e^{-\left(\varphi_{\tilde{Z}}^0\right)^2/2} \times \frac{L_{\mathbf{c}^\dagger \mathbf{c}}^{(-4)}\left(\left(\varphi_{\tilde{Z}}^0\right)^2\right)}{\left(\varphi_{\tilde{Z}}^0\right)^4} \right] \left(\mathbf{c}^4 e^{-4i\omega_Z t} + \text{h.c.} \right) \quad (5.34)$$

for the four-photon pumping interaction.

Finally, by doing a full expansion of the Hamiltonian Eq. (5.22) and taking into account all of the possible resonant terms from each mode in the rotating-wave approximation, while still considering the pump mode semi-classically, I get for the two-photon pumping scheme ($d = 2$)

$$\begin{aligned} \mathbf{H}_{2\text{ph}}^{\text{full}} = & -2\sqrt{2}E_J \left[\frac{\varphi_{\tilde{X}}^0}{2} \times e^{-\left(\varphi_{\tilde{X}}^0\right)^2/8} \times \frac{J_1\left(\varphi_{\tilde{X}}^0\alpha\right)}{\left(\varphi_{\tilde{X}}^0\alpha\right)/2} \right] \times \\ & \left[-\frac{\varphi_{\tilde{Y}}^0}{2} \times e^{-\left(\varphi_{\tilde{Y}}^0\right)^2/8} \times \frac{L_{\mathbf{b}^\dagger \mathbf{b}+1}^{(-1)}\left(\left(\varphi_{\tilde{Y}}^0\right)^2/4\right)}{\left(\varphi_{\tilde{Y}}^0\right)^2/4} \right] \times \\ & \left[-\frac{\left(\varphi_{\tilde{Z}}^0\right)^2}{8} \times e^{-\left(\varphi_{\tilde{Z}}^0\right)^2/8} \times \frac{L_{\mathbf{c}^\dagger \mathbf{c}+2}^{(-2)}\left(\left(\varphi_{\tilde{Z}}^0\right)^2/4\right)}{\left(\varphi_{\tilde{Z}}^0\right)^2/4} \right] \times \\ & \left[\alpha \mathbf{b} \left(\mathbf{c}^\dagger \right)^2 + \alpha^* \mathbf{b}^\dagger \mathbf{c}^2 \right] \end{aligned} \quad (5.35)$$

where $J_1(\cdot)$ is the first kind Bessel function of order one, $L_{\mathbf{n}}^{(\nu)}(\cdot)$ is the generalized Laguerre polynomials of degree \mathbf{n} and index ν and α is the coherent amplitude of the semi-classical pump.

Conversely, for the four-photon pumping scheme ($d = 4$), I get

$$\begin{aligned} \mathbf{H}_{4\text{ph}}^{\text{full}} = & -2\sqrt{2}E_J \left[\frac{\varphi_{\tilde{X}}^0}{2} \times e^{-\left(\varphi_{\tilde{X}}^0\right)^2/8} \times \frac{J_1\left(\varphi_{\tilde{X}}^0\alpha\right)}{\left(\varphi_{\tilde{X}}^0\alpha\right)/2} \right] \times \\ & \left[-\frac{\varphi_{\tilde{Y}}^0}{2} \times e^{-\left(\varphi_{\tilde{Y}}^0\right)^2/8} \times \frac{L_{\mathbf{b}^\dagger \mathbf{b}+1}^{(-1)}\left(\left(\varphi_{\tilde{Y}}^0\right)^2/4\right)}{\left(\varphi_{\tilde{Y}}^0\right)^2/4} \right] \times \\ & \left[e^{-\left(\varphi_{\tilde{Z}}^0\right)^2/2} \times \frac{L_{\mathbf{c}^\dagger \mathbf{c}}^{(-4)}\left(\left(\varphi_{\tilde{Z}}^0\right)^2\right)}{\left(\varphi_{\tilde{Z}}^0\right)^4} \right] \times \\ & \left[\alpha \mathbf{b} \left(\mathbf{c}^\dagger \right)^4 + \alpha^* \mathbf{b}^\dagger \mathbf{c}^4 \right]. \end{aligned} \quad (5.36)$$

In these Hamiltonians, the \mathbf{a} mode (coupled to the X normal mode) is then a *pump* mode, the \mathbf{b} mode (coupled to the Y normal mode) is a *readout* mode and the \mathbf{c} mode (coupled to the Z normal mode) is the *storage* mode. This circuit can implement a two-photon and four-photon interaction Hamiltonian using parametric engineering, whose strength as a function of the number of circulating photons from the pump, $|\alpha|^2$, is shown in Fig. 5.7. However, the coupling strength is strongly reduced by the factorial

prefactors and the (small) zero-point fluctuations appearing with a high power, resulting in an achievable two-photon interaction of the order of 1 MHz and a four-photon interaction of the order of 1 kHz. Further increasing this interaction strength would be experimentally challenging. As an alternative, a two-stage process such as the one proposed in [29] seems more promising and experimentally achievable to implement a four-photon exchange Hamiltonian with a larger interaction strength. The Asymmetric Josephson Ring Modulator circuit could still be a useful tool to implement two-photon exchange Hamiltonian terms, with a large coupling amplitude and reduced nefarious terms.

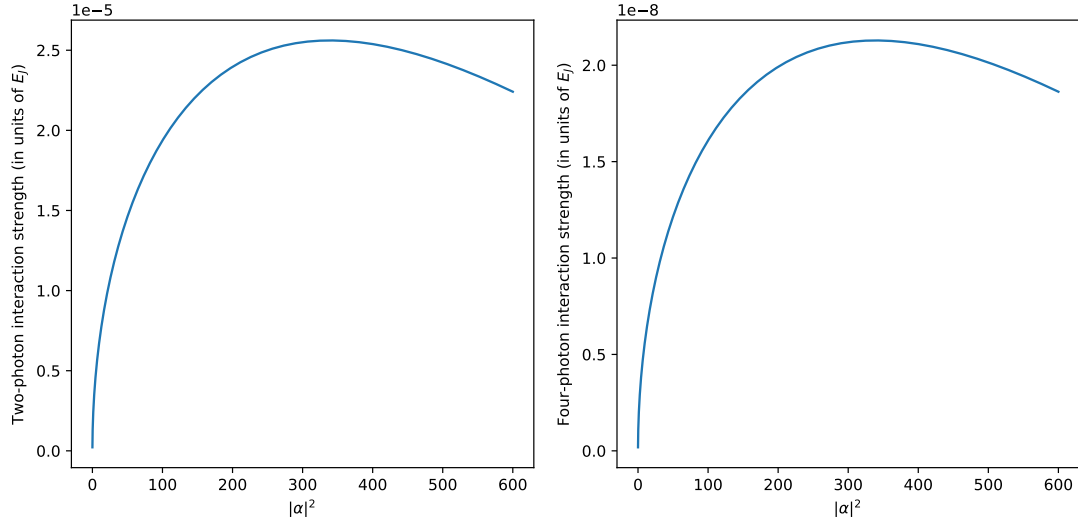


Figure 5.7: **Multi-photon interaction strength.** Strength of the two-photon and four-photon interaction as a function of the number of photons in the pump, $|\alpha|^2$, in units of E_J . Here, the size of the cat state is taken to $|\gamma|^2 = 6$. Using $\varphi_{\tilde{X}} \approx \varphi_{\tilde{Y}} \approx 0.1$ and $\varphi_{\tilde{Z}} \approx 0.05$, the resulting achievable two-photon strength is of the order of $E_J \times 10^{-5} \approx 10$ MHz and the achievable four-photon strength is of the order of $E_J \times 10^{-8} \approx 10$ kHz. These zero-point fluctuations are larger than the typical ones in symmetric JRM. The possibility of their implementation remains to be studied in a future work.

Chapter 6

Conclusions and perspectives

In this thesis, I investigated the behavior of parametrically pumped quantum Josephson circuits in the strong pumping regime. This analysis has been based on the transmon device which is widely used as a source of non-linearity. I considered the cat-states encoding scheme for quantum error correction as an example for parametric engineering of Hamiltonian. This chapter gives a brief summary of the manuscript, along with several comments that intend to put this work into perspective.

In a first part, I focused on the study of the instability of the driven transmon circuit under strong external microwave drives. Indeed, the transmon circuit is one of the most common circuits providing a non-linearity and is therefore of major interest for parametric pumping, that is the engineering of Hamiltonian interactions and tailoring of dissipative terms. The instability of the driven transmon in this regime had been previously observed and used experimentally (for high-fidelity qubit readout). It had already been theoretically investigated assuming two-level, multi-level or Duffing approximations. Contrary to these previous works, the numerical methods presented in this manuscript are non-perturbative and take into account the transmon device as well as its precise coupling with the environment. I also avoid resorting to rotating-wave approximations or cosine potential expansion (contrary to model based on the Duffing approximation). Such approximations are not valid in the strong pumping regime under consideration, as confirmed *a posteriori* by our numerical simulations. These numerical methods let me take into account as much states in the Hilbert space as required. Indeed, thanks to the change of frame described in Chapter 2 (Bogoliubov transformation and mode hybridization), the (displaced) cavity mode is not much populated and can therefore be truncated to a low number of excitations. This lets me use a much higher truncation for the (displaced) transmon mode Hilbert space and take into account enough excited states to capture the states on which the system has support for high pump powers, after the AC Stark shifted frequency jump, while keeping the numerical simulations tractable.

I demonstrated that the transmon circuit is structurally unstable for large enough drives. Indeed, due to the boundedness of the cosine potential of the Josephson junction, the transmon state gets excited to high number of excitations, well above the confinement provided by the cosine potential of the Josephson junction. This translates into limitations of the achievable ac Stark shift strength and of the exploitable range of pump powers. Indeed, above a threshold pump power, the transmon states escapes from the cosine confinement and the system behaves as if there was no nonlinearity, similar to the ionization of an (artificial) atom. This theoretical investigation was conducted in parallel with experimental study of the transmon device at the Laboratoire Pierre-

Aigrain. In this collaboration, we managed to develop a cavity spectroscopy to probe the transmon decay after applying a strong-off resonant pump, resolving the states of the transmon device up to the cosine barrier and confirming our theoretical analysis that the transmon device state is no longer within the cosine confinement potential under the action of such pumps.

These results impose strong limitations when considering the transmon circuit as a tool for parametric engineering, such as in the context of amplification or conversion as well as active qubits. Indeed, active qubits, such as the cat-states encoding scheme presented throughout this manuscript, aim at tailoring interactions and dissipation terms using pump drives and non-linearities (and allowing for broader kind of interactions with more tunability than could be realized with physical implementations), in order to build logical encodings of quantum information protected against (some) decoherence processes. For instance, enforcing the dominant dissipation term to be a multi-photon dissipation, the cat states encoding provides a logical encoding with heavily biased noise: the phase-flip type errors are heavily suppressed and only bit-flip type errors remain. The strength of the engineered interaction usually scales with the pump power and one wishes to reach very high pump strengths. The dynamical instability of the transmon device imposes a hard bound on the maximum achievable pump power, and therefore on the maximum interaction strength.

Then, I proposed an alternative circuit to fix this dynamical instability of the transmon device. This circuit consists in adding an extra inductive shunt in parallel with the Josephson junction, therefore providing an extra harmonic confinement for all pump powers. The same numerical methods used for the analysis of the transmon can be used with this system. Contrary to the unshunted case, the presence of the extra confinement now makes the system stable as illustrated by the smooth ac Stark shifted frequency behavior, slowly decaying towards the renormalized frequency of the modes. The dynamical behavior of this system is also found to be well captured by a rotating-wave approximation of the circuit Hamiltonian, providing a useful tool for analytical investigation and fast numerical simulations of this circuit.

This inductively shunted transmon circuit is currently being experimentally investigated at Yale University by J. Venkatraman under the supervision of M. Devoret. This collaboration has led to a US patent which is pending review. There remains some open theoretical questions on the behavior of these systems, in particular the role of the E_L/E_J ratio in stabilizing the circuit (and the threshold value) as well as on the threshold pump amplitude at which the unshunted transmon circuit becomes highly excited and no longer contributes any nonlinearity. Such questions are still a main and active topic of interest in the QUANTIC team at INRIA and the dynamical stability of these circuits will be studied in the classical approximation, using classical dynamic stability analysis tools, by M. Burgelman who is starting his PhD.

The numerical methods for running the simulations presented in this manuscript are based on the Floquet-Markov theory, which enabled me to take into account large Hilbert space truncations while avoiding both approximating the cosine nonlinearity and resorting to rotating-wave approximations. The whole framework was written in a modular way, in order to make it easily reusable for other physical implementations or circuits. For instance, it has already been used by the M. Devoret group at Yale University to perform numerical simulations of our shunted transmon proposal when considering an array of Josephson junctions instead of an inductive shunt.

Building on the analysis of the transmon and inductively shunted transmon circuits, I finally studied a circuit based on the Josephson Ring Modulator, a circuit already

widely used to achieve amplification and frequency conversion. Using an asymmetric version of this circuit, we can cancel out some of the nefarious terms, simply with symmetry properties. This circuit, in presence of appropriate parametric pumps, should be a powerful tool for implementing two-photon and four-photon interactions. Due to the presence of shunt inductances and building on the previous analysis of the transmon device, one could hope that such a circuit will behave in a stable manner on a wide range of pump parameters, therefore enabling us to reach multi-photon exchange terms with a large enough strength. However, due to the high order of the cosine expansion required to implement a four-photon exchange Hamiltonian term, the coupling strength is strongly reduced by the factorial prefactors and the (small) zero-point fluctuations appearing with a high power. As an alternative, a two-stage process such as the one proposed in [29] seems more promising and experimentally achievable to implement a four-photon exchange Hamiltonian. The Asymmetric Josephson Ring Modulator circuit could still be a useful tool to implement two-photon exchange Hamiltonian terms, with a large coupling amplitude and reduced nefarious terms. The team of Z. Leghtas at ENS is currently investigating similar circuits to implement a cleaner two-photon exchange term in a parametric way while reducing the influence of nefarious terms compared to a single Josephson junction, building on the results and insights we got while studying the Asymmetric Josephson Ring Modulator.

Bibliography

- [1] Charles H. Bennett and Gilles Brassard. Quantum cryptography: Public key distribution and coin tossing. *Theoretical Computer Science*, 560:7–11, dec 2014.
- [2] L. Davidovich. Towards the ultimate precision limits: An introduction to quantum metrology. <http://journals.openedition.org/annuaire-cdf/13568>, 2016. Accessed: 2019-04-25.
- [3] T. Symul, S. M. Assad, and P. K. Lam. Real time demonstration of high bitrate quantum random number generation with coherent laser light. *Applied Physics Letters*, 98(23):231103, jun 2011.
- [4] P. W. Shor. Polynomial-time algorithms for prime factorization and discrete logarithms on a quantum computer. *SIAM Journal on Computing*, 26(5):1484–1509, oct 1997.
- [5] Y. Nakamura, C. D. Chen, and J. S. Tsai. Spectroscopy of energy-level splitting between two macroscopic quantum states of charge coherently superposed by josephson coupling. *Physical Review Letters*, 79(12):2328–2331, September 1997.
- [6] D. Vion, A. Aassime, A. Cottet, P. Joyez, H. Pothier, C. Urbina, D. Esteve, and M. H. Devoret. Manipulating the quantum state of an electrical circuit. *Science*, 296(5569):886–889, 2002.
- [7] H. Paik, D. I. Schuster, L. S. Bishop, G. Kirchmair, G. Catelani, A. P. Sears, B. R. Johnson, M. J. Reagor, L. Frunzio, L. I. Glazman, S. M. Girvin, M. H. Devoret, and R. J. Schoelkopf. Observation of high coherence in josephson junction qubits measured in a three-dimensional circuit QED architecture. *Physical Review Letters*, 107(24), dec 2011.
- [8] C. Rigetti, J. M. Gambetta, S. Poletto, B. L. T. Plourde, J. M. Chow, A. D. Córcoles, J. A. Smolin, S. T. Merkel, J. R. Rozen, G. A. Keefe, M. B. Rothwell, M. B. Ketchen, and M. Steffen. Superconducting qubit in a waveguide cavity with a coherence time approaching 0.1 ms. *Physical Review B*, 86(10), September 2012.
- [9] A. P. Sears. *Extending Coherence in Superconducting Qubits: From microseconds to milliseconds*. PhD thesis, Yale University, 2013.
- [10] K. L. Geerlings. *Improving Coherence of Superconducting Qubits and Resonators*. PhD thesis, Yale University, 2013.
- [11] M. H. Devoret and R. J. Schoelkopf. Superconducting circuits for quantum information: An outlook. *Science*, 339(6124):1169–1174, mar 2013.

- [12] A. Blais, R.-S. Huang, A. Wallraff, S. M. Girvin, and R. J. Schoelkopf. Cavity quantum electrodynamics for superconducting electrical circuits: An architecture for quantum computation. *Physical Review A*, 69(6), jun 2004.
- [13] Y. Makhlin, G. Schön, and A. Shnirman. Quantum-state engineering with josephson-junction devices. *Reviews of Modern Physics*, 73(2):357–400, may 2001.
- [14] S. M. Girvin. Circuit QED: superconducting qubits coupled to microwave photons. In *Quantum Machines: Measurement and Control of Engineered Quantum Systems*, pages 113–256. Oxford University Press, jun 2014.
- [15] S.O. Mundhada, S. Shankar, A. Narla, E. Zolys-Geller, S.M. Girvin, and M.H. Devoret. Dependence of transmon qubit relaxation rate on readout drive power. *APS March Meeting 2016*, 61(2), mar 2016.
- [16] M. Mirrahimi, Z. Leghtas, V. V Albert, S. Touzard, R. J Schoelkopf, L. Jiang, and M. H Devoret. Dynamically protected cat-qubits: a new paradigm for universal quantum computation. *New Journal of Physics*, 16(4):045014, apr 2014.
- [17] M. H. Devoret. Quantum Fluctuations in Electrical Circuits. In S. Reynaud, E. Giacobino, and J. Zinn-Justin, editors, *Fluctuations Quantiques/Quantum Fluctuations*, page 351, 1997.
- [18] W. H. Louisell, A. Yariv, and A. E. Siegman. Quantum fluctuations and noise in parametric processes. i. *Physical Review*, 124(6):1646–1654, December 1961.
- [19] M. Mirrahimi and P. Rouchon. Dynamics and control of open quantum systems. <https://who.rocq.inria.fr/Mazyar.Mirrahimi/QuantSys2015.pdf>. Accessed: 2018-03-06.
- [20] A. Roy and M. Devoret. Introduction to parametric amplification of quantum signals with josephson circuits. *Comptes Rendus Physique*, 17(7):740–755, August 2016.
- [21] B. Yurke, L. R. Corruccini, P. G. Kaminsky, L. W. Rupp, A. D. Smith, A. H. Silver, R. W. Simon, and E. A. Whittaker. Observation of parametric amplification and deamplification in a josephson parametric amplifier. *Physical Review A*, 39(5):2519–2533, March 1989.
- [22] M. A. Castellanos-Beltran and K. W. Lehnert. Widely tunable parametric amplifier based on a superconducting quantum interference device array resonator. *Applied Physics Letters*, 91(8):083509, August 2007.
- [23] T. Yamamoto, K. Inomata, M. Watanabe, K. Matsuba, T. Miyazaki, W. D. Oliver, Y. Nakamura, and J. S. Tsai. Flux-driven josephson parametric amplifier. *Applied Physics Letters*, 93(4):042510, July 2008.
- [24] N. Bergeal, F. Schackert, M. Metcalfe, R. Vijay, V. E. Manucharyan, L. Frunzio, D. E. Prober, R. J. Schoelkopf, S. M. Girvin, and M. H. Devoret. Phase-preserving amplification near the quantum limit with a josephson ring modulator. *Nature*, 465(7294):64–68, may 2010.
- [25] F. D. O. Schackert. *A Practical Quantum-Limited Parametric Amplifier Based on the Josephson Ring Modulator*. PhD thesis, Yale University, 2013.

- [26] Emmanuel Flurin. *The Josephson Mixer, a Swiss army knife for microwave quantum optics*. Theses, Ecole Normale Supérieure, Paris, December 2014.
- [27] E. Flurin, N. Roch, J. D. Pillet, F. Mallet, and B. Huard. Superconducting quantum node for entanglement and storage of microwave radiation. *Physical Review Letters*, 114(9), March 2015.
- [28] Z. Leghtas, S. Touzard, I. M. Pop, A. Kou, B. Vlastakis, A. Petrenko, K. M. Sliwa, A. Narla, S. Shankar, M. J. Hatridge, M. Reagor, L. Frunzio, R. J. Schoelkopf, M. Mirrahimi, and M. H. Devoret. Confining the state of light to a quantum manifold by engineered two-photon loss. *Science*, 347(6224):853–857, feb 2015.
- [29] S O Mundhada, A Grimm, S Touzard, U Vool, S Shankar, M H Devoret, and M Mirrahimi. Generating higher-order quantum dissipation from lower-order parametric processes. *Quantum Science and Technology*, 2(2):024005, may 2017.
- [30] C. Macklin, K. O'Brien, D. Hover, M. E. Schwartz, V. Bolkhovskiy, X. Zhang, W. D. Oliver, and I. Siddiqi. A near-quantum-limited josephson traveling-wave parametric amplifier. *Science*, 350(6258):307–310, September 2015.
- [31] J. Venkatraman, X. Xiao, C. Smith, Z. Leghtas, L. Verney, M. Mirrahimi, S. Shankar, I.-M. Pop, and M. H. Devoret. Suppressing the instabilities of the rf driven transmon by a kinetic inductive shunt - part 1: Motivation and modelization. APS March Meeting, Session E26: Driven and Dissipative Superconducting Circuits, 2019.
- [32] R. Lescanne, L. Verney, Q. Ficheux, M. H. Devoret, B. Huard, M. Mirrahimi, and Z. Leghtas. Escape of a driven quantum josephson circuit into unconfined states. *Physical Review Applied*, 11(1), jan 2019.
- [33] C. Wang, Y. Y. Gao, I. M. Pop, U. Vool, C. Axline, T. Brecht, R. W. Heeres, L. Frunzio, M. H. Devoret, G. Catelani, L. I. Glazman, and R. J. Schoelkopf. Measurement and control of quasiparticle dynamics in a superconducting qubit. *Nature Communications*, 5(1), December 2014.
- [34] Y. Y. Gao, B. J. Lester, Y. Zhang, C. Wang, S. Rosenblum, L. Frunzio, L. Jiang, S. M. Girvin, and R. J. Schoelkopf. Programmable interference between two microwave quantum memories. *ArXiv e-prints*, February 2018.
- [35] Maxime Boissonneault, J. M. Gambetta, and Alexandre Blais. Improved superconducting qubit readout by qubit-induced nonlinearities. *Phys. Rev. Lett.*, 105:100504, Sep 2010.
- [36] M. D. Reed, L. DiCarlo, B. R. Johnson, L. Sun, D. I. Schuster, L. Frunzio, and R. J. Schoelkopf. High-fidelity readout in circuit quantum electrodynamics using the jaynes-cummings nonlinearity. *Phys. Rev. Lett.*, 105:173601, Oct 2010.
- [37] Lev S. Bishop, Eran Ginossar, and S. M. Girvin. Response of the strongly driven jaynes-cummings oscillator. *Phys. Rev. Lett.*, 105:100505, Sep 2010.
- [38] Matthew Elliott and Eran Ginossar. Applications of the fokker-planck equation in circuit quantum electrodynamics. *Phys. Rev. A*, 94:043840, Oct 2016.

- [39] Th. K. Mavrogordatos, G. Tancredi, M. Elliott, M. J. Peterer, A. Patterson, J. Rahamim, P. J. Leek, E. Ginossar, and M. H. Szymańska. Simultaneous bistability of a qubit and resonator in circuit quantum electrodynamics. *Phys. Rev. Lett.*, 118:040402, Jan 2017.
- [40] D. Sank, Z. Chen, M. K., J. Kelly, R. Barends, B. Campbell, Y. Chen, B. Chiaro, A. Dunsworth, A. Fowler, E. Jeffrey, E. Lucero, A. Megrant, J. Mutus, M. Neeley, C. Neill, P. J. J. O’Malley, C. Quintana, P. Roushan, A. Vainsencher, T. White, J. Wenner, Alexander N. Korotkov, and John M. Martinis. Measurement-induced state transitions in a superconducting qubit: Beyond the rotating wave approximation. *Physical Review Letters*, 117(19), nov 2016.
- [41] Rémi Azouit. *Élimination adiabatique pour systèmes quantiques ouverts*. PhD thesis, Ecole des Mines de Paris, 2017. Thèse de doctorat dirigée par Rouchon, Pierre Mathématiques et automatique Paris Sciences et Lettres 2017.
- [42] Paolo Forni. Third- and fourth-order adiabatic elimination for two-photon-pumping example. Private Communication.
- [43] A. Steane. Multiple-particle interference and quantum error correction. *Proceedings of the Royal Society of London. Series A: Mathematical, Physical and Engineering Sciences*, 452(1954):2551–2577, November 1996.
- [44] Z. Leghtas, G. Kirchmair, B. Vlastakis, R. J. Schoelkopf, M. H. Devoret, and M. Mirrahimi. Hardware-efficient autonomous quantum memory protection. *Physical Review Letters*, 111(12), sep 2013.
- [45] Joachim Cohen. *Autonomous quantum error correction with superconducting qubits*. PhD thesis, Ecole Normale Supérieure, Paris, 2017. Thèse de doctorat dirigée par Mirrahimi, Mazyar Physique quantique Paris Sciences et Lettres 2017.
- [46] A. Wallraff, D. I. Schuster, A. Blais, L. Frunzio, R.-S. Huang, J. Majer, S. Kumar, S. M. Girvin, and R. J. Schoelkopf. Strong coupling of a single photon to a superconducting qubit using circuit quantum electrodynamics. *Nature*, 431(7005):162–167, sep 2004.
- [47] D. I. Schuster, A. A. Houck, J. A. Schreier, A. Wallraff, J. M. Gambetta, A. Blais, L. Frunzio, J. Majer, B. Johnson, M. H. Devoret, S. M. Girvin, and R. J. Schoelkopf. Resolving photon number states in a superconducting circuit. *Nature*, 445(7127):515–518, feb 2007.
- [48] G. Kirchmair, B. Vlastakis, Z. Leghtas, S. E. Nigg, H. Paik, E. Ginossar, M. Mirrahimi, L. Frunzio, S. M. Girvin, and R. J. Schoelkopf. Observation of quantum state collapse and revival due to the single-photon kerr effect. *Nature*, 495(7440):205–209, mar 2013.
- [49] B. Abdo, K. Sliwa, F. Schackert, N. Bergeal, M. Hatridge, L. Frunzio, A. D. Stone, and M. Devoret. Full coherent frequency conversion between two propagating microwave modes. *Physical Review Letters*, 110(17), apr 2013.
- [50] M. A. Castellanos-Beltran, K. D. Irwin, G. C. Hilton, L. R. Vale, and K. W. Lehnert. Amplification and squeezing of quantum noise with a tunable josephson metamaterial. *Nature Physics*, 4(12):929–931, oct 2008.

- [51] E. Flurin, N. Roch, F. Mallet, M. H. Devoret, and B. Huard. Generating entangled microwave radiation over two transmission lines. *Physical Review Letters*, 109(18), oct 2012.
- [52] U. Vool, S. Shankar, S.O. Mundhada, N. Ofek, A. Narla, K. Sliwa, E. Zalusky-Geller, Y. Liu, L. Frunzio, R.J. Schoelkopf, S.M. Girvin, and M.H. Devoret. Continuous quantum nondemolition measurement of the transverse component of a qubit. *Physical Review Letters*, 117:133601, 2016.
- [53] D. I. Schuster, A. Wallraff, A. Blais, L. Frunzio, R.-S. Huang, J. Majer, S. M. Girvin, and R. J. Schoelkopf. ac stark shift and dephasing of a superconducting qubit strongly coupled to a cavity field. *Phys. Rev. Lett.*, 94:123602, Mar 2005.
- [54] F. R. Ong, M. Boissonneault, F. Mallet, A. Palacios-Laloy, A. Dewes, A. C. Doherty, A. Blais, P. Bertet, D. Vion, and D. Esteve. Circuit qed with a nonlinear resonator: ac-stark shift and dephasing. *Phys. Rev. Lett.*, 106:167002, Apr 2011.
- [55] Jay Gambetta, Alexandre Blais, D. I. Schuster, A. Wallraff, L. Frunzio, J. Majer, M. H. Devoret, S. M. Girvin, and R. J. Schoelkopf. Qubit-photon interactions in a cavity: Measurement-induced dephasing and number splitting. *Phys. Rev. A*, 74:042318, Oct 2006.
- [56] Jens Koch, Terri M. Yu, Jay Gambetta, A. A. Houck, D. I. Schuster, J. Majer, Alexandre Blais, M. H. Devoret, S. M. Girvin, and R. J. Schoelkopf. Charge-insensitive qubit design derived from the cooper pair box. *Phys. Rev. A*, 76:042319, Oct 2007.
- [57] I. Pietikäinen, S. Danilin, K. S. Kumar, A. Vepsäläinen, D. S. Golubev, J. Tuorila, and G. S. Paraoanu. Observation of the bloch-siegert shift in a driven quantum-to-classical transition. *Phys. Rev. B*, 96:020501, 2017.
- [58] C. Gardiner and P. Zoller. *Quantum Noise: A Handbook of Markovian and Non-Markovian Quantum Stochastic Methods with Applications to Quantum Optics (Springer Series in Synergetics)*. Springer, 2004.
- [59] E. Faou. *Geometric Numerical Integration and Schrödinger Equations*. European Mathematical Society Publishing House, jan 2012.
- [60] I. Pietikäinen, S. Danilin, K. S. Kumar, J. Tuorila, and G. S. Paraoanu. Multilevel effects in a driven generalized rabi model. *Journal of Low Temperature Physics*, 191(5-6):354–364, January 2018.
- [61] S. E. Nigg, H. Paik, B. Vlastakis, G. Kirchmair, S. Shankar, L. Frunzio, M. H. Devoret, R. J. Schoelkopf, and S. M. Girvin. Black-box superconducting circuit quantization. *Physical Review Letters*, 108(24), jun 2012.
- [62] M. Grifoni and P. Hänggi. Driven quantum tunneling. *Physics Reports*, 304(5):229 – 354, 1998.
- [63] M. Silveri, J. Tuorila, M. Kemppainen, and E. Thuneberg. Probe spectroscopy of quasienergy states. *Physical Review B*, 87(13), apr 2013.

- [64] Brian Vlastakis, Gerhard Kirchmair, Zaki Leghtas, Simon E. Nigg, Luigi Frunzio, S. M. Girvin, Mazyar Mirrahimi, M. H. Devoret, and R. J. Schoelkopf. Deterministically encoding quantum information using 100-photon schrödinger cat states. *Science*, 342(6158):607–610, 2013.
- [65] J. Koch, V.E. Manucharyan, M.H. Devoret, and L. Glazman. Charging effects in the inductively shunted Josephson junction. *Phys. Rev. Lett.*, 103:217004, 2009.
- [66] J. Braumüller, M. Sandberg, M.R. Vissers, A. Schneider, S. Schlör, L. Grünhaupt, H. Rotzinger, M. Marthaler, A. Lukashenko, A. Dieter, A.V. Ustinov, M. Weides, and D.P. Pappas. Concentric transmon qubit featuring fast tunability and an anisotropic magnetic dipole moment. *Appl. Phys. Lett.*, 108:032601, 2016.
- [67] S. Richer, N. Maleeva, S.T. Skacel, I.M. Pop, and D. DiVincenzo. Inductively shunted transmon qubit with tunable transverse and longitudinal coupling. *Phys. Rev. B*, 96:174520, 2017.
- [68] J. E. Mooij, T. P. Orlando, L. Levitov, Lin Tian, Caspar H. van der Wal, and Seth Lloyd. Josephson persistent-current qubit. *Science*, 285(5430):1036–1039, 1999.
- [69] Vladimir E. Manucharyan, Jens Koch, Leonid I. Glazman, and Michel H. Devoret. Fluxonium: Single cooper-pair circuit free of charge offsets. *Science*, 326(5949):113–116, 2009.
- [70] N. E. Frattini, U. Vool, S. Shankar, A. Narla, K. M. Sliwa, and M. H. Devoret. 3-wave mixing josephson dipole element. *Applied Physics Letters*, 110(22):222603, may 2017.
- [71] J.R. Johansson, P.D. Nation, and F. Nori. QuTiP: An open-source python framework for the dynamics of open quantum systems. *Computer Physics Communications*, 183(8):1760–1772, aug 2012.
- [72] J.R. Johansson, P.D. Nation, and F. Nori. QuTiP 2: A python framework for the dynamics of open quantum systems. *Computer Physics Communications*, 184(4):1234–1240, apr 2013.
- [73] T. Oliphant. NumPy: A guide to NumPy. USA: Trelgol Publishing, 2006–. [Online; accessed <today>].
- [74] E. Jones, T. Oliphant, P. Peterson, et al. SciPy: Open source scientific tools for Python, 2001–. [Online; accessed <today>].
- [75] S. Behnel, R. Bradshaw, C. Citro, L. Dalcin, D.S. Seljebotn, and K. Smith. Cython: The best of both worlds. *Computing in Science Engineering*, 13(2):31–39, mar-apr 2011.
- [76] J. D. Hunter. Matplotlib: A 2d graphics environment. *Computing In Science & Engineering*, 9(3):90–95, 2007.
- [77] N. Roch, E. Flurin, F. Nguyen, P. Morfin, P. Campagne-Ibarcq, M. H. Devoret, and B. Huard. Widely tunable, nondegenerate three-wave mixing microwave device operating near the quantum limit. *Physical Review Letters*, 108(14), apr 2012.

RÉSUMÉ

Dans cette thèse, nous étudions le comportement de circuits Josephson sous l'action de champs micro-ondes forts. Les circuits Josephson dans le régime quantique sont une brique pour émuler une variété d'hamiltoniens, utiles pour traiter l'information quantique. Nous étudions ici le transmon, constitué d'une jonction Josephson et d'un condensateur en parallèle. À travers des simulations numériques et en comparant aux résultats expérimentaux, nous montrons que ces champs conduisent à une instabilité qui envoie le circuit sur des états qui ne sont plus confinés par le potentiel Josephson en cosinus. Quand le transmon occupe de tels états, le circuit se comporte comme si la jonction avait été remplacée par un interrupteur ouvert et toute non-linéarité est perdue, ce qui se traduit par des limitations sur les amplitudes maximales des hamiltoniens émulés.

Dans une deuxième partie, nous proposons et étudions un circuit alternatif basé sur un transmon avec une inductance en parallèle, qui fournit un confinement harmonique. La dynamique de ce circuit est stable et bien capturée par un modèle moyennisé qui fournit alors un outil pratique pour l'analyse analytique ou les simulations rapides.

Nous avons développé un nouvel outil de simulations modulaire et basé sur la théorie de Floquet-Markov pour permettre de simuler facilement d'autres circuits Josephson en évitant les limitations des analyses perturbatives.

Enfin, nous étudions les propriétés d'une version asymétrique du *Josephson Ring Modulator*, un circuit actuellement utilisé pour l'amplification et la conversion, comme source de non-linéarité pour émuler les hamiltoniens d'interaction à deux et quatre photons requis pour l'encodage de l'information quantique sur des états de chats de Schrödinger.

MOTS CLÉS

Information quantique, circuits supraconducteurs, pompage paramétrique, hamiltoniens paramétriques, ingénierie de réservoir, code quantique.

ABSTRACT

In this thesis, we investigate the behavior of Josephson circuits under the action of strong microwave drives. Josephson circuits in the quantum regime are a building block to emulate a variety of Hamiltonians, useful to process quantum information. We are here considering a transmon device, made of a Josephson junction and a capacitor in parallel. Through numerical simulations and comparison with experimental results, we show that these drives lead to an instability which results in the escape of the circuit state into states which are no longer confined by the Josephson cosine potential. When the transmon occupies such states, the circuit behaves as if the junction had been removed and all non-linearities are lost, which translates into limitations on the emulated Hamiltonian strengths.

In a second part, we propose and study an alternative circuit consisting of a transmon device with an extra inductive shunt, providing a harmonic confinement. This circuit is found to be stable for all pump powers. The dynamics of this circuit is also well captured by a time-averaged model, providing a useful tool for analytical investigation and fast numerical simulations. We developed a novel numerical approach that avoids the built-in limitations of perturbative analysis to investigate the dynamical behavior of both of these circuits. This approach, based on the Floquet-Markov theory, resulted in a modular simulation framework which can be used to study other Josephson-based circuits.

Last, we study the properties of an asymmetric version of the Josephson Ring Modulator, a circuit currently used for amplification and conversion, as a more robust source of non-linearity to engineer two-photon and four-photon interaction Hamiltonians required for the cat-state encoding of quantum information.

KEYWORDS

Quantum information, superconducting circuits, parametric pumping, hamiltonian engineering, reservoir engineering, quantum error correction.